Numerical Modeling of Frequency Combs: Functionality, Stability and Control

Chang Sun

A dissertation
submitted in partial fulfillment of the
requirements for the degree of

Doctor of Philosophy

University of Washington

2021

Reading Committee:

J. Nathan Kutz, Chair

Marcel den Nijs

Subhadeep Gupta

Program Authorized to Offer Degree:
Physics

University of Washington

Abstract

Numerical Modeling of Frequency Combs:
Functionality, Stability and Control

Chang Sun

Chair of the Supervisory Committee:
Professor J. Nathan Kutz
Applied Mathematics

Frequency comb generation has been at the scientific forefront for several decades because of its potential applications in fundamental and applied physics, including chemical sensing, optical atomic clocks and low-phase-noise microwave radiation. Still, the generation of stable frequency combs is often hand-tuned in experiments and the dynamics are sensitive to perturbations of the system. Therefore we wish to find a theoretical characterization of how the perturbations deform the frequency combs. We derive a micro-comb perturbation theory that allows one to consider the effects of higher-order terms in the microresonator for frequency comb generation, including Raman scattering, spontaneous emission noises and enforcing pump noises. To generate frequency combs at a preferable parameter regime in a semiconductor diode laser, we introduce the waveguide arrays for its temporal shaping effects to provide intensity discrimination and controllable loss by mode-coupling. The stable and efficient numerical scheme of this model is demonstrated, followed by a von-Neumann analysis. In addition, we develop a fast, reliable self-tuning controller with deep reinforcement learning to obtain the high-energy, single-pulse state in a passive mode-locked fiber laser. The self-tuning strategy allows the optical system to recognize bi-stable structures and navigate to optimally performing solutions via trajectory planning.

TABLE OF CONTENTS

LIST OF FIGURES

LIST OF TABLES

ACKNOWLEDGMENTS

I wish to express my sincere appreciation to my advisor, J. Nathan Kutz, not only for his guidance to make this research possible, but his encouragement that shapes and inspires me over the years. I would like to thank Eurika Kaiser, Steven L. Brunton, Niall M. Mangan, Mark Dong, Steven T. Cundiff, Herbert G. Winful and Travis Askham, for their advice and patience to make the difficult work enjoyable. I am also indebted to all my committee members, J. Nathan Kutz, Marcel den Nijs, Subhadeep Gupta, Jiun-Haw Chu, Steven L. Brunton and Antonino Ferrante, for their generous help and support. I also want to thank my family and friends, who have been so important supporting me throughout my school life, especially those early days as a graduate student.

DEDICATION

to my dear parents and husband

Chapter 1

INTRODUCTION

The invention of the laser in 1960 is a pivotal moment in scientific innovation and fundamental physics [99]. The laser has become ubiquitous in academic, medical and industrial research and applications in the past few decades because of its reliability, capacity and compaction. For instance, the laser is a key instrument for research in spectroscopy, fluorescence microscopy and laser interferometry. It's also used in revolutionary medical devices such as dentistry and microsurgery. Some applications, for instance, multi-heterodyne spectroscopy, optical atomic clocks, and high-speed fiber-optic communication systems, require sequence of ultrashort pulses that are nearly uniform in amplitudes. Over the decades, the generation of such soliton pulses has been attractive to academic arenas due to its great impact on ultrafast and nonlinear optics [85], and a variety of physically realizable laser cavity configurations have been presented both theoretically and experimentally. In this thesis, we focus on the formation of frequency combs and therefore the generation of a single-peaked cavity soliton. A frequency comb is a sequence of equidistant frequency lines in a spectrum that forms as a short-pulse laser in time. Frequency combs can be formed by different mechanisms, here we focus on frequency combs generated in passive microresonators due to the Kerr nonlinearity, as well as the mode-locking of fiber lasers. The latter mechanism has been the most attractive in the past decades, and has led to one half of the Nobel Prize in Physics in 2005. Generally, intensity discrimination and a bandwidth limited gain are essential for the generation of mode-locking. The intensity discrimination preferentially selects high intensity and attenuates weaker intensity portions of individual pulses, whereas this attenuation is compensated by the bandwidth limited gain to preserve the total energy inside cavity. The pulse shaping occurs consequently as the high intensity portion experiences a net gain while

the low intensity tails have a net loss.

In a dispersive medium, the propagation of an optical field is given by Maxwell's equations

$$\nabla \times \mathbf{E} = -\frac{\partial \mathbf{B}}{\partial t}, \tag{1.1a}$$

$$\nabla \times \mathbf{H} = \mathbf{J}_f + \frac{\partial \mathbf{D}}{\partial t}, \tag{1.1b}$$

$$\nabla \cdot \mathbf{D} = \rho_f, \tag{1.1c}$$

$$\nabla \cdot \mathbf{B} = 0, \tag{1.1d}$$

where the electric field, the magnetic field, the corresponding electric displacement field and the magnetic flux density are denoted by $\mathbf{E}(x, y, z, t)$, $\mathbf{H}(x, y, z, t)$, $\mathbf{D}(x, y, z, t)$ and $\mathbf{B}(x, y, z, t)$ respectively. $\mathbf{J}_f$ is the free current density and ρ_f denotes the free electric charge density. In a given medium, the flux densities $\mathbf{D}$ and $\mathbf{B}$ are related to the electric and magnetic fields as:

$$\mathbf{D} = \epsilon_0 \mathbf{E} + \mathbf{P}, \tag{1.2a}$$

$$\mathbf{B} = \mu_0 \mathbf{H} + \mathbf{M}, \tag{1.2b}$$

where ϵ_0 and μ_0 are the permittivity and permeability of free space respectively. The magnetization field $\mathbf{M}$ is absent at optical frequencies. $\mathbf{P}$ is the induced polarization field, it characterizes the nonlinear response of the medium to the electric field. Rearranging equations (1.1)-(1.2) gives the electric field evolution equation

$$\nabla^2 \mathbf{E} - \nabla(\nabla \cdot \mathbf{E}) - \frac{1}{c^2}\frac{\partial^2 \mathbf{E}}{\partial t^2} = \mu_0 \frac{\partial^2 \mathbf{P}(\mathbf{E})}{\partial t^2}, \tag{1.3}$$

which reduces in the one-dimensional case to

$$\frac{\partial^2 E}{\partial x^2} - \frac{1}{c^2}\frac{\partial^2 E}{\partial t^2} = \mu_0 \frac{\partial^2 P(E)}{\partial t^2}. \tag{1.4}$$

For a nonlinear media, the electric polarization field P takes the form

$$\mathbf{P} = \epsilon_0 \chi^{(1)} \mathbf{E} + \epsilon_0 \chi^{(2)} \mathbf{E} \cdot \mathbf{E} + \epsilon_0 \chi^{(3)} (\mathbf{E} \cdot \mathbf{E}) \mathbf{E} + ..., \tag{1.5}$$

where $\chi^{(1)}$ is the linear response of the polarization to the electric field. As we assume the propagation in a centrosymmetric medium, $\chi^{(2)} = 0$ due to the inversion symmetry. $\chi^{(3)}$ is the nonlinear (cubic) susceptibility, it is significant in materials exhibiting a non-negligible Kerr effect. We consider a governing equation with linear propagation and an instantaneous Kerr effect:

$$\frac{\partial^2 E}{\partial x^2} - \frac{1}{c^2}\frac{\partial^2 E}{\partial t^2} = \frac{1}{c^2}\frac{\partial^2}{\partial t^2}(\int_{-\infty}^{t} \chi^{(1)}(t-\tau)E(\tau,x)d\tau + \chi^{(3)}E^3), \tag{1.6}$$

where $c = \sqrt{1/(\epsilon_0\mu_0)}$ is the speed of light. Note that Eq. (1.6) yields waves propagating in both directions in the medium, but we are interested in propagation along a single direction in the waveguide. Following the center-frequency asymptotic [91], we assume

$$E(x,t) = u(x,t)e^{i(kx-\omega t)} + c.c. \tag{1.7}$$

where k is the wavenumber, ω is the optical frequency and $c.c.$ denotes complex conjugate. Note that we assume $k,\ \omega \gg 1$, and a slowly-varying envelop compared to the carrier dynamics $exp(ikx - i\omega t)$. Eq. (1.7) reduces to a plane wave solution when u is constant. Inserting Eq. (1.7) into Eq. (1.6) and letting $\sigma = t - \tau$, we obtain

$$\begin{aligned} &e^{i(kx-\omega t)}(u_{xx} + 2iku_x - k^2u) - \frac{1}{c^2}e^{i(kx-\omega t)}(u_{tt} - 2i\omega u_t - \omega^2 u) \\ &= \frac{1}{c^2}\frac{\partial^2}{\partial t^2}e^{i(kx-\omega t)}(\int_0^{\infty} \chi^{(1)}(\sigma)u(t-\sigma,x)e^{i\omega\sigma}d\sigma + \chi^{(3)}|u|^2u). \end{aligned} \tag{1.8}$$

Taking Taylor expansion for $u(t-\sigma,x)$

$$u(t-\sigma,x) = u(t,x) - \sigma u_t(x,t) + \frac{1}{2}\sigma^2 u_{tt}(x,t) + ... \tag{1.9}$$

and inserting into Eq. (1.8) we obtain

$$c^2(u_{xx}+2iku_x-k^2u)+\omega^2(1+\hat{\chi})u+i[(\omega^2\hat{\chi})_\omega+2\omega]u_t-1/2[(\omega^2\hat{\chi})_{\omega\omega}+2]u_{tt}+\omega^2\chi^{(3)}|u|^2u+... = 0, \tag{1.10}$$

where $\hat{\chi} = \int_0^{\infty} \chi^{(1)}(\sigma)e^{i\omega\sigma}d\sigma$ is the Fourier transform of the linear susceptibility. Assume $\chi^{(1)}$ is real. A complex linear susceptibility is considered in the following sections, with its

imaginary part leading to an attenuation inside the laser cavity. Assume k, $\omega \gg 1$, the leading order of Eq. (1.10) balances so that

$$k^2 = \frac{\omega^2}{c^2}(1 + \hat{\chi}). \tag{1.11}$$

Taking derivatives of Eq. (1.11) we obtain

$$2c^2 k k' = (\omega^2 \hat{\chi})_\omega + 2\omega, \tag{1.12a}$$

$$2c^2(kk'' + (k')^2) = (\omega^2 \hat{\chi})_{\omega\omega} + 2, \tag{1.12b}$$

where $k' = dk/d\omega$ is the inverse of the group velocity v_g. Inserting Eq. (1.12) into Eq. (1.10) and transforming into the moving reference frame by defining

$$t = t - k'x, \tag{1.13a}$$

$$x = x, \tag{1.13b}$$

we obtain the governing equation, i.e., the nonlinear Schrödinger equation (NLSE)

$$iu_x - \frac{k''}{2}u_{tt} + \sum_{n=3}^{\infty} \beta_n \partial_t^{(n)} u + \alpha|u|^2 u = 0, \tag{1.14}$$

where $\alpha = \omega^2 \chi^{(3)}/2kc^2$, β_n $(n > 2)$ are the coefficients of the higher-order dispersion. In the standard NLSE, higher order terms of chromatic dispersion are neglected and we obtain with appropriate normalization:

$$iu_x - \frac{k''}{2}u_{tt} + |u|^2 u = 0. \tag{1.15}$$

In Eq. (1.15), the chromatic dispersion and Kerr nonlinearity are dominant and need to be balanced for the generation and stabilization of frequency combs. Once the intra-cavity pulse is shaped, Kerr nonlinearity leads to the nonlinear self-phase modulation, which balances the chromatic dispersion and nonlinearly locks the phase of different axial modes inside the cavity, and forms the stable trains of solitons.

In this thesis, three different models for the generation of frequency combs are presented, newly developed and discussed in details. The thesis outline is as follows: three different

models are briefly summarized in Chapter 1, followed by a more thorough discussion in Chapter 2-5 for each model respectively. Chapter 2 focuses on the model built with the Lugiato-Lefever equation (LLE), the governing equation characterizing the frequency comb generation in microresonators. We extend the soliton perturbation theory and derive a new micro-comb perturbation theory, with which a new class of periodic solutions to LLE is formed to interpret the microresonator dynamics and effects of perturbations on the comb line stability. A theoretical model describing the lasing dynamics of a semiconductor diode laser based on quantum wells is presented in Chapter 3. A waveguide array is highlighted for providing the essential intensity discrimination and controllable loss for mode-locking. The stable and efficient numerical scheme used for this traveling wave model is demonstrated in Chapter 4, followed by a von-Neumann analysis showing that the combination of a predictor-corrector scheme with an operator-splitting strategy efficiently provides a stable scheme to characterize the nonlinear dispersive cavity dynamics with counter propagating waves and complex semiconductor gain dynamics. In Chapter 5, we focus on the control and self-tuning of mode-locked lasers, and demonstrate an effective strategy for the control with deep reinforcement learning. A well-established computational model is used to characterize the intra-cavity dynamics, which treats the cavity in a component by component manner by separately applying the nonlinear optical propagation to the laser dynamics with discrete waveplates and polarizer in each round trip. The propagation of intra-cavity fields is modeled by the modified coupled nonlinear Schrödinger equations (CNLS), whereas the effect of the waveplates and polarizer is modeled by the discrete application of Jones matrices. By interacting with the environment, a deep reinforcement learning controller can automatically achieve and stabilize around the desired mode-locking state through its access to the waveplates and polarizer. Furthermore, we show that deep reinforcement learning enables the laser system to recognize bi-stable structures and achieve the global optimal states. With transfer learning, the deep reinforcement learning controller can rapidly generalize its control authority to new environments and can provide an effective control to the laser system.

Models of frequency comb generation

A high-level summary of the three different models discussed in this thesis to achieve frequency combs is presented in this section.

Lugiato-Lefever Equation

The Lugiato-Lefever equation (LLE) was originally formulated by Luigi Lugiato and Renè Lefever in 1987 in the context of detuned cavity resonators [98]. It has been demonstrated to describe the interaction of a coherent field with a Kerr medium, as well as the evolution of the electric fields in microresonators [23]. As a modification of the nonlinear Schrödinger equation (NLSE), the dimensionless LLE, a partial differential equation (PDE),

$$\frac{\partial u}{\partial t} = -(1 + i\alpha)u + i|u|^2 u - i\frac{\beta}{2}\frac{\partial^2 u}{\partial x^2} + F, \tag{1.16}$$

includes the damping, detuning, dispersion and a pumping term. $u(x,t)$ represents the complex envelope of the total intra-cavity electric field, t is the time normalized by half-linewidth, x is transformed to remove the group velocity motion and we have $x \in [-\pi, \pi)$ since the microresonator enforces periodic boundary conditions [23]. α is the cavity detuning parameter, and β determines the microring dispersion, where a positive value stands for normal group-velocity dispersion and $\beta < 0$ represents anomalous group-velocity dispersion. The pumping term F characterizes the external cavity excitation.

We follow the standard convention of the Lugiato-Lefever equation in Eq. (1.16) where the group velocity motion is removed by the transformation

$$x = x - v_g t, \tag{1.17a}$$

$$t = t. \tag{1.17b}$$

This convention is followed in Chapter 2 in the development of the micro-comb perturbation theory of LLE, whereas the models in Chapter 3-5 of this thesis follow the convention in the form of the standard NLSE Eq. (1.15).

Waveguide Array Mode-Locking

The waveguide array (WGA) architecture is a pulse shaping strategy that promotes stable waveforms with intensity discrimination. More specifically, it contributes to the pulse formation and stabilization in a laser system by providing the linear, evanescent mode coupling as saturable absorption.

Numerical studies and stability analyses [5] show that to form the waveguide array, three or more waveguides should be included to produce robust pulse shaping and intensity discrimination. Moreover, early WGA experiments [112] show that a three waveguide structure has almost identical properties to the 41 waveguides. Therefore, we consider a WGA architecture with three waveguides here. The leading-order equation describing the intra-cavity dynamics with linear, evanescent mode coupling to the neighboring waveguides is given as

$$i\frac{du_n}{dx} + C(u_{n-1} + u_{n+1}) + \beta|u_n|^2 u_n = 0, \tag{1.18}$$

where u_n represents the electric field envelope in the n-th waveguide in the waveguide array, x represents the normalized distance in the waveguide array, C is the linear coupling coefficient, and β represents the nonlinear self-phase modulation parameter [5, 26, 112]. The electric field propagating in the first waveguide is shaped by coupling out low-intensity portion to the neighboring waveguides. The mode coupling provides a controllable loss mechanism to filter out the high order longitudinal modes, and contributes to the necessary intensity discrimination to achieve stable mode-locked pulses in a laser cavity [22, 114, 89].

Coupled Nonlinear Schrödinger Equation with Jones Matrices

The schematic of the mode-locked laser with passive nonlinear polarization rotation is shown in Fig. 1.1, where the intra-cavity dynamic is modeled in a component by component manner by separating the nonlinear optical propagation from the discrete waveplates and polarizer applied in each round trip through the cavity [40, 39, 82]. The propagation of the intra-cavity

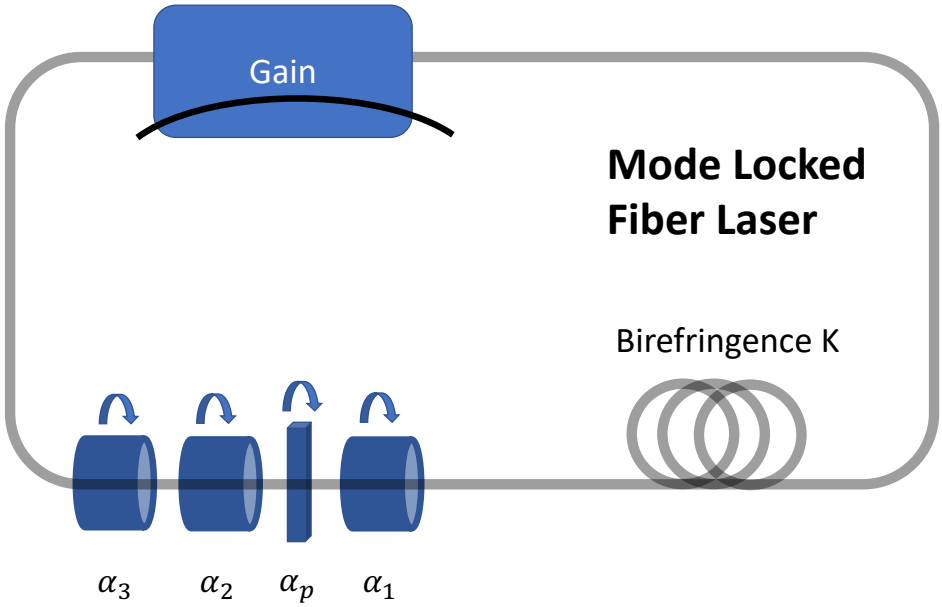

Figure 1.1: Schematic of the mode-locked laser with passive nonlinear polarization rotation (NPR). α_1 and α_2 are the quarter-waveplates, α_3 is the half-waveplate, and α_p is the polarizer. K is the fiber birefringence that is sensitive to thermal fluctuations.

fields is modeled by the coupled nonlinear Schrödinger equations (CNLS) as

$$i\frac{\partial u}{\partial x} + \frac{D}{2}\frac{\partial^2 u}{\partial t^2} - Ku + (|u|^2 + A|v|^2)u + Bv^2u^* = iRu, \tag{1.19}$$

$$i\frac{\partial v}{\partial x} + \frac{D}{2}\frac{\partial^2 v}{\partial t^2} + Kv + (A|u|^2 + |v|^2)v + Bu^2v^* = iRv, \tag{1.20}$$

where $u(x,t)$ and $v(x,t)$ are the two orthogonally polarized intra-cavity electric field envelopes that are often referred as the fast and slow components respectively. x is the propagation distance normalized by the cavity length, and the dimensionless time t is normalized by the full width at half maximum of the pulse. D is the average group velocity dispersion, and K is the fiber birefringence that is sensitive to thermal fluctuations. A and B are the nonlinear coupling parameters characterizing the cross-phase modulation and the four-wave mixing. In a silica fiber we have $A = 2/3$ and $B = 1/3$. R is the dissipative term characterizing the bandwidth-limited gain and attenuation arising from the Yb-doped amplification, and is defined as

$$R = \frac{2g_0(1 + \tau\partial_t^2)}{1 + (1/e_0)\int_{-\infty}^{\infty}(|u|^2 + |v|^2)dt} - \Gamma, \tag{1.21}$$

where g_0 and e_0 are the dimensionless pumping strength and saturating energy of the gain medium, respectively. The pump bandwidth is τ and Γ characterizes losses caused by output coupling and fiber attenuation.

The waveplates and polarizer are applied in each round trip of the propagation through the cavity for generation of mode-locking, and their effect is modeled by the discrete application of Jones matrices:

$$W_{\lambda/4} = \begin{bmatrix} e^{-i\pi/4} & 0 \\ 0 & e^{i\pi/4} \end{bmatrix}, W_{\lambda/2} = \begin{bmatrix} -i & 0 \\ 0 & i \end{bmatrix}, W_p = \begin{bmatrix} 1 & 0 \\ 0 & 0 \end{bmatrix}. \tag{1.22}$$

In our model, we have two quarter-waveplates (α_1 and α_2) characterized by $W_{\lambda/4}$, one half-waveplate (α_3) characterized by $W_{\lambda/2}$, and one polarizer (α_p) characterized by W_p. A rotation matrix $R(\alpha)$ is necessary for characterizing the offset between the direction of the intra-cavity field and the principal axes of the waveplates and polarizer, and the effect of the

waveplates and polarizer during each round trip is eventually modeled as

$$J_j = R(\alpha_j) W_j R(-\alpha_j), \tag{1.23}$$

where

$$R(\alpha_j) = \begin{bmatrix} cos(\alpha_j) & -sin(\alpha_j) \\ sin(\alpha_j) & cos(\alpha_j) \end{bmatrix} \quad (j = 1, 2, 3, p). \tag{1.24}$$

Note that the waveplate and polarizer angles α_j $(j = 1, 2, 3, p)$ can be easily manipulated via electronic control [126], therefore are considered as the control variables to establish robust self-tuning and control of the mode-locking laser system here. This component-by-component model illustrates a variety of rich, intra-cavity laser dynamics [130, 88, 86].

Chapter 2

ELLIPTIC FUNCTION SOLUTIONS OF LUGIATO-LEFEVER EQUATION

In this chapter[1], the model built with the Lugiato-Lefever equation (LLE) is discussed, and a new class of periodic solutions to the LLE is demonstrated to characterize the propagation of intra-cavity fields in a microresonator cavity. Specifically, a new micro-comb perturbation theory is derived by extending the soliton perturbation theory, with Jacobi elliptic functions as the leading order solutions to the LLE. Stability analysis shows that the Jacobi elliptic *dn* is the only stable solution stabilized by the pumping of the microresonator. It's also demonstrated that the new micro-comb perturbation theory is able to characterize the effects of physically realizable perturbations on the combline stability, including effects of Raman scattering and stimulated emission. The new micro-comb perturbation theory, verified through full numerical simulations of the LLE, serves as an analytic platform for discovering new methods of achieving mode-locking and engineering new resonator designs.

2.1 Introduction

As a critical technology applied in metrology, high-resolution spectroscopy and microwave photonics [31, 80, 36, 110, 45, 113, 95, 133], frequency comb generation in microresonators is often achieved by the generation of a single soliton in a high-Q microresonator cavity [59, 151]. However in analogy with the multi-pulsing instability (MPI) in mode-locked laser cavities [3, 149, 93], the performance of the frequency comb generation in such microresonators is limited as the microresonators tend to generate multiple pulses in the cavity [60, 55]. Though solitons have been broadly observed in experiments, it only becomes possible recently to manipulate

[1]Content of this chapter is published in journal article [134].

states with multiple solitons deterministically in microresonators with the goal of prediction and control [60]. Consequently we are interested in providing a theoretical complement to the recent experimental observations for characterizing the dynamics and stability of frequency comb generation in the microresonators, especially the transitions between N to $N+1$ (or vice versa) pulses in a microresonator.

Enlightened by the soliton perturbation theory, a theory well-known for its success in characterizing the underlying physics in optical communication systems [72, 81, 77, 43] and mode-locked lasers [75, 70, 71, 4], we derive a micro-comb perturbation theory and analytically explore the solutions to the Lugiato-Lefever equation (LLE) [98], the governing equation of the microresonator dynamics [23], for a better interpretation of the intra-cavity dynamics in this chapter. Note that the theory relies on an analytic solution, the Galilean invariant one-soliton solution, of the nonlinear Schrödinger equation. Given the LLE as the governing equation, we analytically characterize the intra-cavity dynamics with Jacobi elliptic function as the leading order solution, which is a generalization of soliton solutions of the LLE and has the form of either a single localized pulse or a periodic pulse train.

Furthermore, we demonstrate the effects of including cavity perturbations, for instance, the Raman effect or spontaneous emission noise, to the combline stability and robustness with the perturbation theory. Much like solitons, the Jacobi elliptic solutions are determined by a number of parameters of which the slow evolution characterizes the stability of the solutions. Such parameters, however, are constrained by the cavity perturbations. We demonstrate in this chapter a linear stability analysis of the Jacobi elliptic solutions to characterize the key combline properties under perturbation. Notice that similar to MPI in mode-locked lasers [3, 149, 93], the cavity tends to jump to the most energetically favorable configuration when initially started. Our analysis characterizes the stability of N pulses per round trip in the laser cavity, and demonstrate, in consistency with the experimental findings, that one can change the microresonator detuning to manipulate the number of pulses per round trip as desired.

In Section 2.2, we first briefly give an overview of the perturbation theory and the soliton

perturbation theory. The LLE is then introduced with the specific scalings as used here to model the microresonator. Section 2.3 presents the Jacobi elliptic function solutions that satisfy the LLE as the leading order solutions in our scalings and Section 2.4 shows in detail the linear stability analysis of the Jacobi elliptic function solutions. Raman effect, spontaneous emission noises and enforcing pump noises are considered in section 2.5 as three canonical perturbations to the intra-cavity dynamics in our scalings. Section 2.6 briefly summarizes the theoretical method demonstrated and its potential applications in engineering new resonator designs.

2.2 Background: perturbation theory and Lugiato-Lefever equation (LLE)

2.2.1 Perturbation Theory

We start with an introduction to perturbation theory, which solves the problems with no analytic solutions by breaking them into solvable and perturbation parts. For instance, in the most general form, we consider the one dimensional PDE as

$$\frac{\partial u}{\partial t} = N(u, u_x, u_{xx}, \cdots, \mu) + \epsilon G(u, x, t) \ , \tag{2.1}$$

where $N(\cdot)$ represents some analytically solvable nonlinear dynamics, and μ is a (bifurcation) parameter. $\epsilon G(u, x, t)$ is a small term treated as a perturbation to the solvable dynamics. Perturbation theory leads to a solution in the form of a multi-scale perturbation expansion [8, 78]. Specifically, the solution is given as

$$u(x,t) = u_0(x,t,\tau) + \epsilon u_1(x,t) + \epsilon^2 u_2(x,t) + \cdots \ , \tag{2.2}$$

where $\tau = \epsilon t$ corresponds to a slow variable dependence [81, 148]. Note that the deviation from the exactly solvable problem is characterized in the higher order terms of ϵ.

We break the unsolvable problem by collecting terms at each order of ϵ. The leading order terms form the analytically solvable problem with nonlinear dynamics, whereas forced,

linear dynamics is given by all other orders, i.e.

$$\begin{aligned}
\frac{\partial u_0}{\partial t} &= N(u_0, u_{0x}, u_{0xx}, \cdots, \mu) \ , && \text{(2.3a)} \\
\frac{\partial u_1}{\partial t} &= L_1(u_0)u_1 + F_1(u_0) \ , && \text{(2.3b)} \\
\frac{\partial u_2}{\partial t} &= L_2(u_0)u_2 + F_2(u_0, u_1) \ , && \text{(2.3c)} \\
&\vdots
\end{aligned}$$

where the first equation is the $O(1)$ balance, the second equation is the $O(\epsilon)$ balance and the third equations is the $O(\epsilon^2)$ balance. As in the approach of Weinstein [148], we consider a solution of the leading order problem with slow-time modulation. Let $u_0(x,t)$ be given by

$$u_0(x,t) = \Phi(x, t, A_1, A_2, \cdots) \ , \tag{2.4}$$

where the parameters A_i are functions of the slow time scale τ as $A_i = A_i(\tau)$. Following the Fredholm alternative, the forcing term F_1 in the forced, linear PDE of u_1 is required to be orthogonal to the generalized null space of the adjoint operator $L_1^\dagger$, i.e. if $(L_1^\dagger)^m v = 0$ for some $m > 0$, then

$$\langle v, F_1 \rangle = 0 \ , \tag{2.5}$$

where $\langle u, v \rangle = \int_D uv^* \, dx$ is the inner product over the domain D. This applies constraints to the evolution of the parameters A_i on the slow time scale τ in the form as

$$\frac{\partial A_i}{\partial \tau} = f_i(A_1, A_2, \cdots) \ . \tag{2.6}$$

Importantly, Weinstein's analysis of the NLSE [148] demonstrates that these constraints are all that needs to be satisfied for ϵu_1 to be small when ϵ is small. In the following sections, we demonstrate similar results in the configuration of our LLE perturbation theory. Specifically, we show that the additional terms in LLE can be treated as a perturbation to the NLSE, and stabilize the parameters of the Jacobi elliptic *dn* solutions. We further demonstrate that these orthogonal constraints lead to evolution of the parameters A_i when Raman effect, spontaneous emission noises and enforcing pump noises are included.

Soliton Perturbation Theory

We demonstrate here, as comparison to our LLE perturbation theory, a brief introduction to soliton perturbation theory first. As an example, consider the perturbed nonlinear Schrödinger equation (NLSE)

$$i\frac{\partial u}{\partial t}+\frac{1}{2}\frac{\partial^2 u}{\partial x^2}+|u|^2u=\epsilon G(u,x,t), \tag{2.7}$$

where $\epsilon G(u,x,t)$ is a small term representing the perturbation to NLSE. The leading-order, Galilean invariant one-soliton solution is given by

$$u_0(x,t)=\eta sech[\eta(x-x_0)]e^{i[\xi(x-x_0)+\phi-\phi_0]}=U_0\exp^{i\psi} \tag{2.8}$$

where $dx_0/dt=\xi$ and $d\phi/dt=(\xi^2+\eta^2)/2$. Note that this one-soliton solution is parameterized by η, x_0, ξ and ϕ_0 as functions of the slow time-scale τ.

We collect the terms at order $O(\epsilon)$ for the forced, linear dynamics as defined in Eq. (3.3b). Computing the linearized operator $L(u_0)$ allows us to compute the solvability conditions associated with the perturbed problem at $O(\epsilon)$. This enforces the following constraints on the slow evolution of the parameters:

$$\frac{d\eta}{d\tau}=\frac{1}{2}\langle sech\zeta, \Im\left(\exp(-i\psi)G(u_0)\right)\rangle \tag{2.9a}$$
$$\frac{dx_0}{d\tau}=\frac{1}{\eta^2}\langle \zeta sech\zeta, \Im\left(\exp(-i\psi)G(u_0)\right)\rangle \tag{2.9b}$$
$$\frac{d\xi}{d\tau}=\eta\langle \tanh\zeta sech\zeta, \Re\left(\exp(-i\psi)G(u_0)\right)\rangle \tag{2.9c}$$
$$\frac{d\phi_0}{d\tau}+\xi\frac{dx_0}{d\tau}=\langle \zeta tanh\zeta sech\zeta, \Re\left(\exp(-i\psi)G(u_0)\right)\rangle \tag{2.9d}$$

where $\zeta=\eta(x-x_0)$. The four inner products represented are the enforced orthogonality conditions with respect to the null space of the linearized operator

$$L=\frac{1}{2}\eta^2\begin{bmatrix}0 & L_-\\ -L_+ & 0\end{bmatrix} \tag{2.10}$$

where

$$L_- = \frac{d^2}{dx^2} + 2sech^2\zeta - 1, \tag{2.11a}$$

$$L_+ = \frac{d^2}{dx^2} + 6sech^2\zeta - 1. \tag{2.11b}$$

2.2.2 Lugiato-Lefever equation

The Lugiato-Lefever equation (LLE), a modification of the nonlinear Schrödinger equation (NLSE), was originally derived in detuned cavity resonators [98] to describe the evolution of the electromagnetic field in microresonators [23]. As introduced in Chapter 1, the LLE includes damping, detuning and a driving/pumping term, and is given in the dimensionless form as

$$\frac{\partial u}{\partial t} = -(\epsilon + i\alpha)u + i|u|^2u - i\frac{\beta}{2}\frac{\partial^2 u}{\partial x^2} + \epsilon F + \epsilon G(u, x, t), \tag{2.12}$$

where $u(x, t)$ represents the complex envelope of the total intra-cavity electric field, t is the time normalized by half mode bandwidth. α characterizes the cavity detuning, and β determines the microring dispersion, where a positive value quantifies the normal group-velocity dispersion and $\beta < 0$ is anomalous group-velocity dispersion. The pumping term F characterizes the external cavity excitation, x is transformed to remove the group velocity motion and we have $x \in [-\pi, \pi)$ since the microresonator enforces periodic boundary conditions [23].

Note that in our specific scaling, we rearrange the LLE as a perturbed version of the detuned NLSE:

$$i\frac{\partial u}{\partial t} - \frac{\beta}{2}\frac{\partial^2 u}{\partial x^2} + |u|^2u - \alpha u = i\epsilon(F - u + G(u, x, t)), \tag{2.13}$$

where we treat dispersion, Kerr self-phase modulation, and detuning as the dominant dynamics inside the microresonator. The effects of pumping, linear cavity attenuation and small perturbations $G(u, x, t)$ are modeled by the parameter $\epsilon \ll 1$. Taking the limit of $\epsilon = 1$ recovers the original LLE derived in [98].

This scaling allows us to develop a systematic perturbation analysis of previously unconsidered, periodic Jacobi elliptic solutions of the LLE. This complements the detailed stability

analysis of Godey et al. [51] which details the onset of a myriad of spatio-temporal patterns in the LLE model. Specifically, they show that the steady-state solutions of the LLE (with all temporal and spatial derivatives set to zero) lead to a host of pattern-forming instabilities [30] that are ultimately responsible for the generation of strongly nonlinear periodic waveforms. In our analysis, we consider the stability of Jacobi elliptic solutions which are strongly nonlinear solutions whose dominant balance includes temporal and spatial derivative terms [21, 13, 14, 12].

2.3 Jacobi Elliptic Functions for the LLE

The Jacobi elliptic functions are periodic wavefunctions that satisfy the NLSE with detuning [21, 13, 14, 12]. Specifically, $sn(x|k)$, $cn(x|k)$, and $dn(x|k)$ are three basic types of the Jacobi elliptic functions, and they are the solutions to the following three differential equations respectively:

$sn(x|k)$:

$$\frac{d^2y}{\partial x^2} + (1+k^2)y - 2k^2y^3 = 0, \tag{2.14}$$

$cn(x|k)$:

$$\frac{d^2y}{\partial x^2} + (1-2k^2)y + 2k^2y^3 = 0, \tag{2.15}$$

$dn(x|k)$:

$$\frac{d^2y}{\partial x^2} - (2-k^2)y + 2y^3 = 0. \tag{2.16}$$

These solutions are parameterized by the elliptic modulus k, which is constrained in $[0, 1)$, as shown in Fig. 2.1. In software for evaluating the Jacobi elliptic functions, the parameter $m = k^2$ is more commonly used. Note that the period of $sn(x|k)$ and $cn(x|k)$ is $4K$, but $dn(x|k)$ is $2K$ periodic, where K is the complete elliptic integral of the first kind depending on k.

As described by Eq. (2.13), we write the LLE in the form as a perturbed NLSE with detuning, and the Jacobi elliptic functions are solutions to its leading order dynamics. Specifically, expand the full LLE solution u into $u = u_0(x,t,\tau) + \epsilon u_1(x,t,\tau)$, where $\tau = \epsilon * t$ denotes

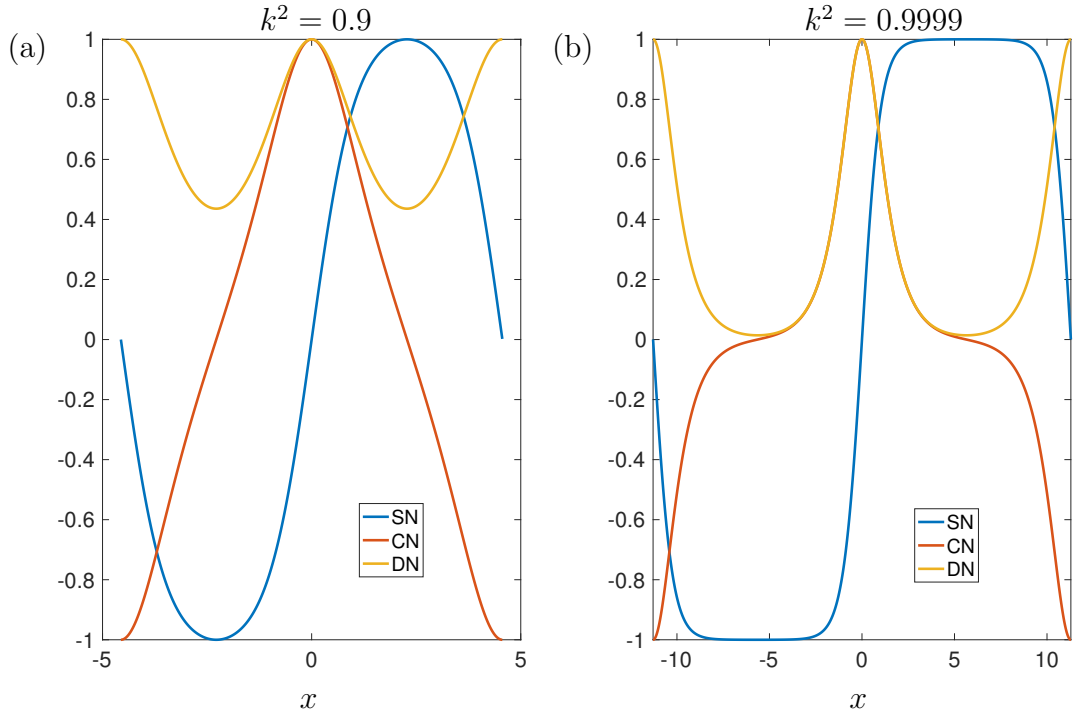

Figure 2.1: Three basic types of the Jacobi elliptic functions $sn(x|k)$, $cn(x|k)$, and $dn(x|k)$ that are parameterized by the elliptic modulus k.

the slow time dependency, and collect the terms at order $O(1)$ and $O(\epsilon)$ separately, we obtain the leading order equation:

$$iu_{0t} - \alpha u_0 + |u_0|^2 u_0 - \frac{\beta}{2} u_{0xx} = 0, \tag{2.17}$$

and find the Jacobi elliptic functions $sn(x|k)$, $cn(x|k)$ and $dn(x|k)$ as solutions to Eq. (2.17).

The stability of these solutions to NLSE is well-studied. The Jacobi elliptic sn is the solution to the defocusing NLSE with $\beta > 0$ as denoted in Eq. (2.13), and is known to be modulationally stable [11]. The Jacobi elliptic cn and dn, on the other hand, are known as solutions to the focusing NLSE with $\beta < 0$, and are shown modulationally unstable [34]. Recent research [56] further demonstrates that the dn solution is spectrally stable only under perturbations with a period equal to the fundamental period, but not a multiple of the fundamental period. The Jacobi elliptic cn, as shown similarly by spectral stability analysis, is only stable when $k \in (0, k_c)$ ($k_c \approx 0.908$) under perturbations with a period equal to the fundamental period [56]. In-depth discussion of the stability properties of Jacobi elliptic function solutions of the NLSE can be found in [11, 34, 56].

Furthermore, we demonstrate that the damping and pumping terms of the microresonator in LLE destabilize the cn and sn solutions in their respective regimes. Figure 2.2 shows a numerical simulation of the LLE with damping and pumping terms that starts with a four-pulse wave in the form of cn and sn. The sn wave form quickly decays to the constant solution, and the cn wave form evolves into a form of the dn type that has two pulses instead of four. It appears that the wave forms with pulses separated by a node, i.e., with a π phase change between neighboring pulses, are not supported by the LLE albeit their spectral stability as a solution to the NLSE. The dn type solutions, however, are in fact stable solutions to LLE with the damping and pumping terms, even with multiple pulses in the cavity. In Bose-Einstein condensates, the addition of a Hamiltonian term, i.e. a periodic potential generated by the interference of lasers, can stabilize the elliptic function solutions [13, 14, 12]. In the LLE, the perturbations considered to Eq. (2.13) are dissipative in nature, modeling the damping and forcing on the microresonator. As we demonstrate in the following

section, the dissipative terms can stabilize the $dn(x|k)$ solutions in the anomalous regime, and we focus on the dn type solutions in the remainder of this chapter.

Solutions of dn type: anomalous dispersion

As mentioned previously, the dn solution is the only stable solution to the LLE with damping and external forcing/pumping terms in the anomalous dispersion regime ($\beta < 0$). More discussion about the dn solution are provided in details as it is of the most practical importance. We assume the general form for this solution as

$$u_0(x,t) = \hat{u}_0 e^{i\psi} = A dn(B(x-x_0)|k) e^{i[\xi(x-x_0)+\sigma-\sigma_0]}, \tag{2.18}$$

of which the constraints on parameters A, B, ξ, σ, x_0 and σ_0 are required to satisfy Eq. (2.17). Since the second derivative of u_0 is given

$$u_{0xx} = AB^2 dn'' e^{i\psi} + 2iAB\psi_x dn' e^{i\psi} - A\psi_x^2 dn e^{i\psi} + iA\psi_{xx} dn e^{i\psi}, \tag{2.19}$$

and

$$iu_{0t} = iA[Bdn'(-\frac{dx_0}{dt})e^{i\psi} + dne^{i\psi} i(-\xi\frac{dx_0}{dt} + \frac{d\sigma_0}{dt})], \tag{2.20}$$

collecting terms of dn, dn^3 and dn' separately, we obtain

dn :

$$-A(-\xi\frac{dx_0}{dt} + \frac{d\sigma}{dt})dn - \alpha A dn\frac{\beta}{2}AB^2(2-k^2)dn + \frac{\beta}{2}A\xi^2 dn = 0, \tag{2.21}$$

dn^3 :

$$\beta AB^2 dn^3 + A^3 dn^3 = 0, \tag{2.22}$$

dn' :

$$-iAB(\frac{dx_0}{dt})dn' - i\beta AB\xi dn' = 0. \tag{2.23}$$

To have Eq. (2.17) satisfied for any x, we obtain $A^2 = -\beta B^2$, and

$$\frac{dx_0}{dt} = -\beta\xi, \tag{2.24a}$$

$$\frac{d\sigma}{dt} = -\alpha - \frac{\beta}{2}B^2(2-k^2) - \frac{\beta}{2}\xi^2. \tag{2.24b}$$

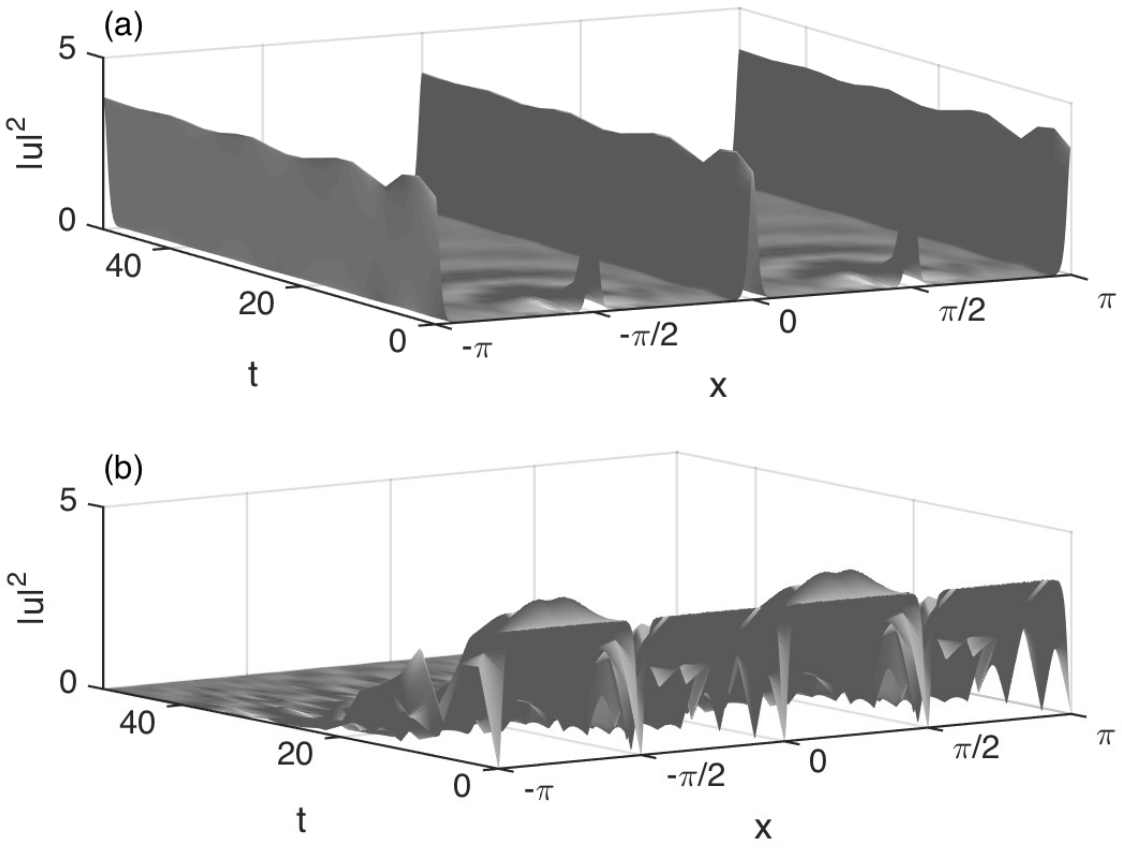

Figure 2.2: Numerical simulation of the (a) *cn* and (b) *sn* solutions of Eq. (2.13) with $|\beta| = 0.01$, $\epsilon = 0.1$, $G = 0$, and the detuning α set to (a) $\alpha = 1.8732$ and (b) $\alpha = 3.7464$ (these values of the detuning are chosen so that $k^2 = 1 - 10^{-12} \approx 1$ in the analog of Eq. (2.26) for these solutions). The solutions were seeded with a white noise perturbation to induce instability in the evolution. Both solutions are unstable, even in the limit $k \to 1$ where the linear stability analysis shows the eigenvalues to shrink to the real axis. Note that the *cn* solution collapses from an $N = 4$ solution to a stable $N = 2$ *dn* solution.

Since we are characterizing the intra-cavity dynamics of a microresonator with enforced periodic boundary conditions, the leading order solution $u_0(x,t)$ should be $2\pi/N$ periodic, where N is a positive integer representing the number of localized pulses per round trip in the microresonator. Considering that the period of the Jacobi elliptic dn is modulated by k, the value of B determines the value of k and vice-versa. Specifically, the period of the Jacobi elliptic function $y = dn(x|k)$ is $2K(k)$, where $K(k)$, as a function of k, is the elliptic integral of the first kind. For $\hat{u}_0 = dn(Bx|k)$ given in Eq. (2.13), we have its period as $T = 2K/B$. To satisfy the periodic boundary condition, we have $2K/B = 2\pi/N$, thus $B = KN/\pi$.

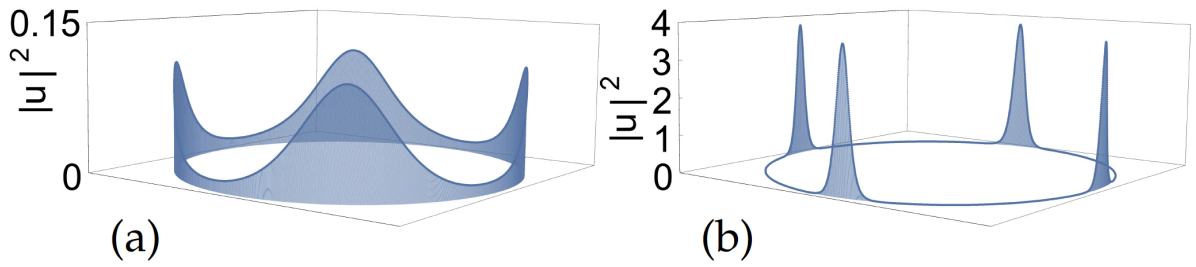

Figure 2.3: The dn-type solutions for (a) $k^2 = 0.9$ and (b) $k^2 = 1 - 10^{-12} \approx 1$ with $N = 4$. The two panels demonstrate that the elliptic modulus $k \in [0, 1)$ can produce solutions which resemble a modulated CW beam or highly localized, hyperbolic secant pulses. Note that the dn solution has no nodal points where the solution is zero.

The dn-type solutions for two values of the parameter k are shown in Fig. 2.3, where $k \in [0, 1)$. In the limit $k \to 0$, the function $dn(x|k) \to 1$, i.e., a continuous wave solution of the LLE. When $k \to 1$, the function $dn(x|k) \to sech(x)$, which is the standard hyperbolic secant soliton solution generated by the dominant NLSE terms. Fig. 2.3 shows the $k^2 = 0.9$ and $k^2 = 1 - 10^{-12} \approx 1$ solutions of the LLE. Note that these figures are illustrated with four localized pulses per round trip in the microresonator ($N = 4$). Figure 2.4 shows the dn solutions with the number of localized pulses N increased from one to four. As N increases, the pulses are narrowed down in width but increased in height.

Here we consider leading order solutions about the center frequency with a fixed phase

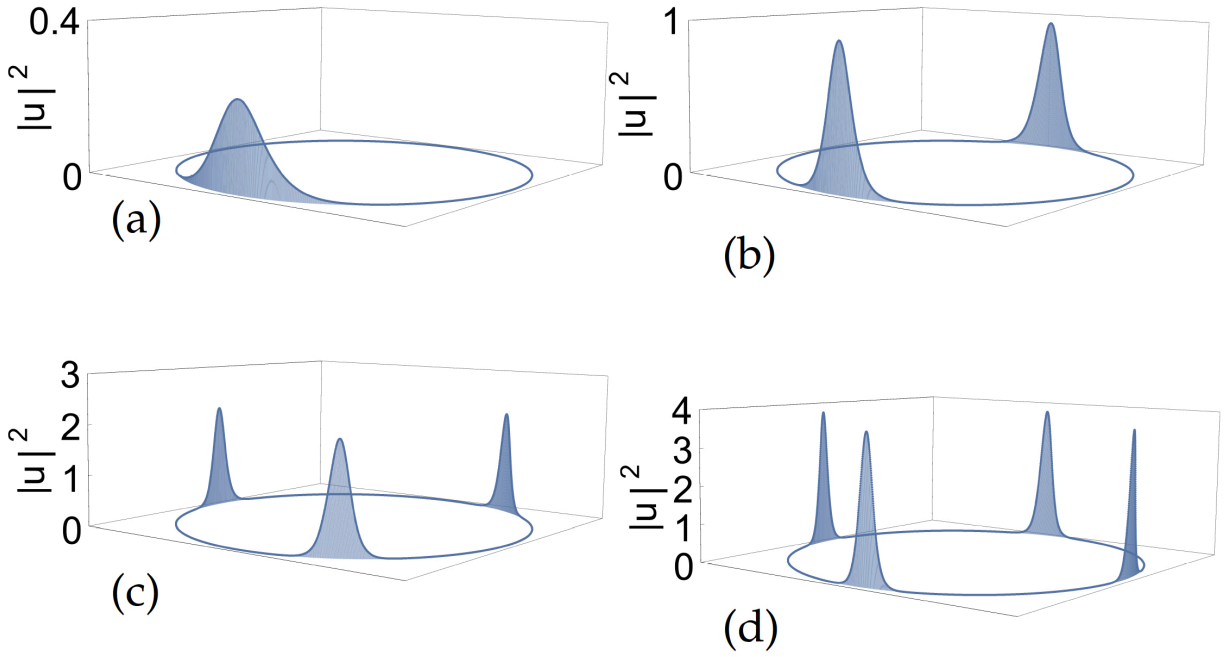

Figure 2.4: The dn solution for $N = 1, 2, 3$ and 4. Here we plot dn solutions with the same modulus, $k^2 = 1 - 10^{-12} \approx 1$, as functions on a circle (to emphasize their periodicity). As the number of pulses N increases, the width of the each pulse narrows and the height increases. These four solution branches co-exist for a fixed value of the detuning α. The stability of each solution branch depends upon the detuning parameter as shown in Fig. 2.5.

term, given the observed solutions of LLE in numerical simulations. Thus the parameters of the leading order solution Eq. (2.18) are constrained by setting

$$\xi = 0, \tag{2.25}$$

$$\alpha = -\beta B^2(2 - k^2)/2. \tag{2.26}$$

These constrains require the detuning α to increase in order to accommodate more pulses per round trip, which is consistent with experimental findings.

Furthermore, we can characterize the dependence of the cavity energy e_c on the detuning frequency α. Given

$$e_c = \int_{-\pi}^{\pi} |u_0|^2 dx = -\beta B^2 \int_{-\pi}^{\pi} dn^2(By|k) dy, \tag{2.27}$$

we demonstrate the energy of each solution branch with different values of N in Fig. 2.5. The stability of each branch will be discussed in what follows, but the energy versus detuning shows the important trends to be considered. For $k \to 1$, the function $dn(x|k) \to sech(x)$ so that the energy integral can be approximated explicitly

$$e_c \approx -\beta B \int_{-B\pi}^{B\pi} sech^2 z dz = -2\beta B \ . \tag{2.28}$$

Given that $\alpha \approx -\beta B^2/2$, we can then simplify the relationship between the detuning and cavity energy, i.e. $|e_c/\beta| \approx 2\sqrt{2}\sqrt{|\alpha/\beta|}$. This value is for only a single pulse. If there are N pulses, we obtain

$$|e_c/\beta| = 2\sqrt{2}N\sqrt{|\alpha/\beta|}. \tag{2.29}$$

This gives a simple quantization of the energy as a function of the number of pulses in the limit $k \to 1$. We will show in what follows that the $k \to 1$ limit is where solutions to the LLE are stable, thus the energy quantization formula is a good approximation for the LLE microresonator dynamics.

Note that in Fig. 2.5, since $|\alpha/\beta| = B^2/2$, we have $|\alpha/\beta| \to \infty$ when $k \to 1$ and $|\alpha/\beta| \to 0$ when $k \to 0$.

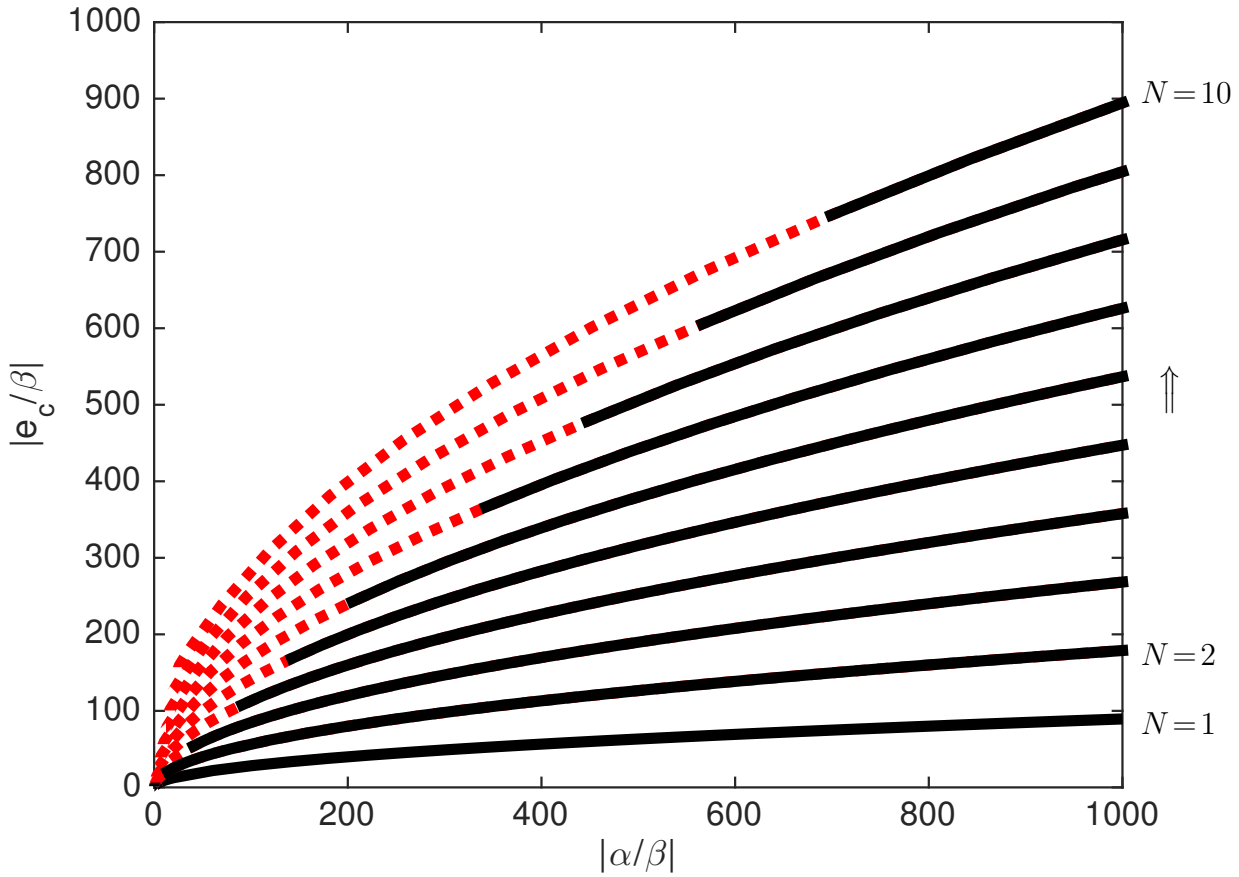

Figure 2.5: The solution branches of the *dn* solution as a function of energy ($|e_c/\beta|$) versus detuning ($|\alpha/\beta|$). Plotted are the solution branches from $N = 1$ to $N = 10$. The instability of each branch can be computed from the linearized operator Eq. 2.33. Specifically, if the real part of any eigenvalue crosses the threshold of 5×10^{-4}, then the branch is considered unstable (dashed red lines) for that value of detuning. For candidate branches that are potentially stable (black lines), further analysis is required to confirm the stability of the *dn* solution branches. This figure matches recent experimental findings of [55] and confirms that the specific number of pulses in the microresonator can be controlled by manipulation of the detuning.

2.4 Stability Analysis of the LLE

The stability of the Jacobi elliptic function solutions to the LLE can be characterized using a linear stability analysis. Note that parameters A, B, x_0, ξ and σ_0 all vary slowly on $\tau = \epsilon t$, the contribution of iu_0 to the equation of $O(\epsilon)$ is

$$i[A_\tau dn + A(B_\tau(x - x_0))dn' + iAdn(\xi(x - x_0) - \xi x_{0\tau} - \sigma_{o\tau})]e^{i\psi}. \tag{2.30}$$

Let $u_1 = e^{i\psi}w_1$, following the perturbation expansion of Eq. (2.2), we find the linearized evolution in the order $O(\epsilon)$:

$$i\frac{\partial w_1}{\partial t} - \alpha w_1 + 2|u_0|^2 w_1 - \frac{\beta}{2}\frac{\partial^2 w_1}{\partial x^2} + |u_0|^2 w_1^* = \hat{F}, \tag{2.31}$$

where $\hat{F} = i(e^{-i\psi}F + e^{-i\psi}G(u_0, x, t) - \hat{u}_0 - e^{-i\psi}u_{0\tau})$.

We can decompose the linearized evolution into real and imaginary components by letting $w_1 = R + iI$, $(w_1^* = R - iI)$ so that in matrix notation it takes the form

$$\begin{bmatrix} R_t \\ I_t \end{bmatrix} = \begin{bmatrix} 0 & \frac{\beta}{2}\partial_x^2 - \hat{u}_0^2 + \alpha \\ -\frac{\beta}{2}\partial_x^2 + 3\hat{u}_0^2 - \alpha & 0 \end{bmatrix} \begin{bmatrix} R \\ I \end{bmatrix} + \begin{bmatrix} \Im\hat{F} \\ \Re\hat{F} \end{bmatrix}, \tag{2.32}$$

where ∂_x^2 denotes the second order derivative. The eigenvalue spectrum of the matrix in Eq. (2.32) yields the spectral stability of dn solutions, generally. Note that for $\hat{u}_0$ given by the dn solution, $\alpha = -\beta B^2(2 - k^2)/2$.

Figure 2.6 shows the computed spectrum of the linearized operator in Eq. (2.32) for the dn solution with $N = 4$. The operator was numerically evaluated using a spectrally accurate method with 1024 grid points (a fast Fourier transform was used to evaluate the second derivatives) and a standard matrix eigenvalue solver. The eigenvalues corresponding to both $k^2 = 0.9$ and $k^2 = 1 - 10^{-12} \approx 1$ are evaluated. Note for the case $N = 4$, the fundamental period $T = \pi/2$, thus $[-\pi, \pi)$ is a multiple of the fundamental period, so we expect instability [56]. For $k^2 = 0.9$, the dn solution clearly has unstable eigenvalues, i.e. eigenvalues with large positive real part. As $k \to 1$, the real part of the eigenvalues of dn shrink to the imaginary axis, suggesting that the $k \to 1$ solutions will be better behaved, even if they are

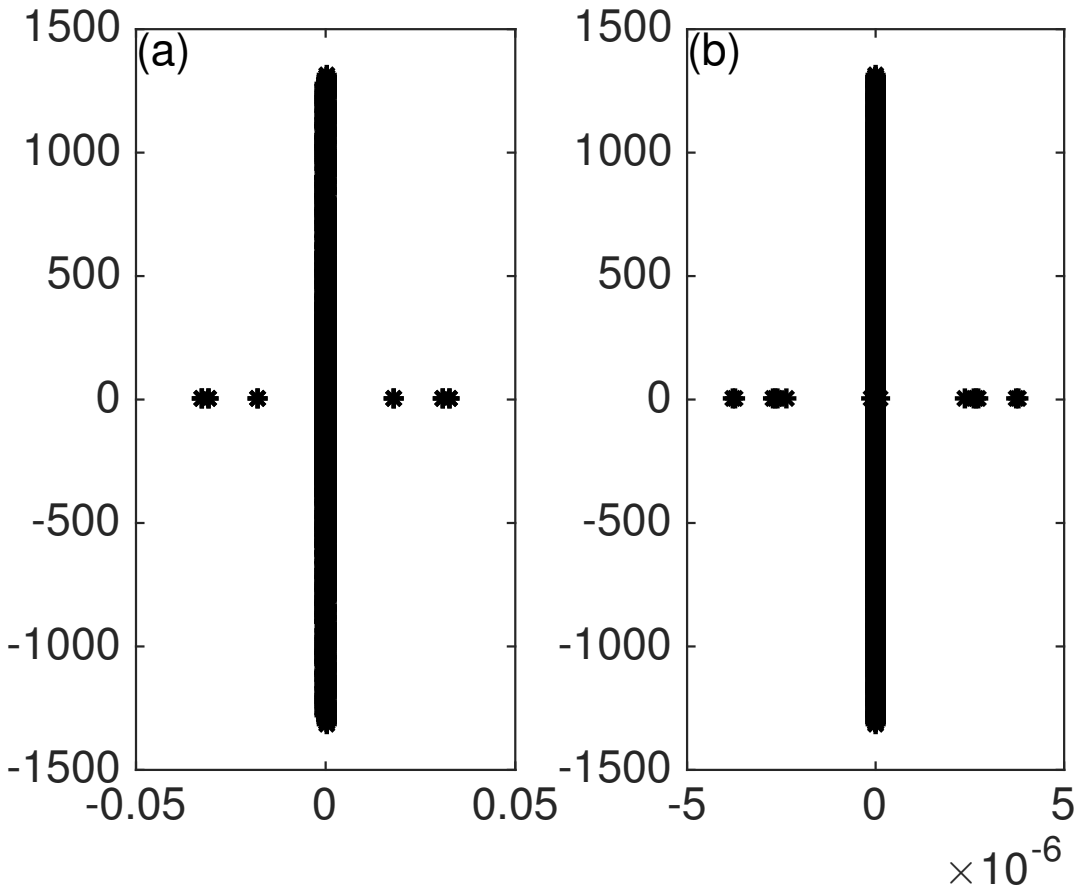

Figure 2.6: Eigenvalue spectrum of the matrix $\mathbf{L}$ defined in Eq. (2.32) for the dn solution with (a) $k^2 = 0.9$ and (b) $k^2 = 1 - 10^{-12} \approx 1$. Although the eigenvalues shrink to the imaginary axis as $k \to 1$, the solutions are known to be unstable under generic perturbations.

technically unstable [56]. Thus a critical part of the analysis is to determine if the addition of the LLE term F stabilizes such microresonator solutions subject to slow-time modulation of the parameters.

2.4.1 Discrete Spectrum of dn Solutions

As with soliton perturbation theory, the generalized null space of the adjoint of the linearized operator is critical for determining stability. Specifically, the Fredholm-alternative theorem stated in Eq. (2.5) requires that perturbations be orthogonal to the null space of the adjoint linear operator (this removes so-called "secular" modes which have polynomial growth in time [148]). For the *dn* solution, the linear operator reduces to

$$\mathbf{L} = -\frac{\beta}{2}B^2 \begin{bmatrix} 0 & L_- \\ -L_+ & 0 \end{bmatrix}, \tag{2.33}$$

with the self-adjoint operators

$$L_- = -\frac{d^2}{dz^2} - 2dn^2 z - k^2 + 2 \,, \tag{2.34a}$$

$$L_+ = -\frac{d^2}{dz^2} - 6dn^2 z - k^2 + 2 \,, \tag{2.34b}$$

where a change of variables to $z = B(x - x_0)$ has been made and the dependence of dn on k has been dropped for notational convenience.

In the following, we will denote the generalized nullspace of a linear operator L by $\ker_g(L)$, i.e.

$$\ker_g(L) = \bigcup_{m=1}^{\infty} \ker(L^m) \,. \tag{2.35}$$

We also require the space $H^m_{\text{per}}[a,b)$, which denotes a periodic Sobolev space on $[a,b)$. This space may be characterized by the Fourier coefficients of a given function. Let f be a function defined on $[a,b) = [-\pi,\pi)$ and let c_j defined by

$$c_j = \frac{1}{2\pi}\int_{-\pi}^{\pi} f(x)e^{-ijx}\,dx \,. \tag{2.36}$$

Then the $H^m_{\rm per}[-\pi,\pi)$ norm is defined by

$$\|f\|^2_{H^m_{\rm per}} = \sum_j |c_j|^2(1+|j|^2+\cdots|j|^{2m}) \; . \tag{2.37}$$

Note that if $\|f\|_{H^m_{\rm per}} < \infty$, then the Fourier coefficients of the $(m-1)st$ derivative of f are absolutely summable so that $f^{(m-1)}$ is continuous as a periodic function on $[-\pi,\pi)$. The space $H^m_{\rm per}$ can be defined for other intervals by appropriate scaling.

Let $w_1 = R + iI$ as above. As in [148], we define the space

$$\mathcal{M} = H^1_{\rm per} \times H^1_{\rm per} \bigcap \left(\ker_g(\mathbf{L}^\dagger)\right)^\perp \; , \tag{2.38}$$

which is where we will constrain the evolution of $(R,I)^T$. Note that the domain for z is $[-NK(k), NK(k))$. We also define the periodic functions $\phi(z)$ and $\varphi(z)$ to be

$$\phi(z) = (K(k)E(z,k) - E(k)z)dnz - k^2K(k)snzcnz, \tag{2.39a}$$

$$\begin{aligned}\varphi(z) = {} & k^2 cnzsnz(K(k)E(z,k) - E(k)z) \\ & +(E(k)-K(k))dnz + k^2K(k)cn^2zdnz \; ,\end{aligned} \tag{2.39b}$$

where $E(z,k) = \int_0^z dn^2y dy$ is the incomplete elliptic integral of the second kind, $E(k) = E(K(k),k)$ is the complete elliptic integral of the second kind, and $K(k)$ is as above. For the sake of compactness, we will often drop the dependence of $E(k)$ and $K(k)$ on the modulus k in the following. Note that $E(z,k)$ is odd, $\phi(z)$ is odd, and $\varphi(z)$ is even — the parity of functions simplifies much of the following analysis. A set of eigenfunctions that span $\ker_g(\mathbf{L}^\dagger)$ can then be computed from the following observations

$$L_-[dnz] = 0, \tag{2.40a}$$

$$L_+[snzcnz] = 0, \tag{2.40b}$$

$$L_+L_-\left[\phi(z)\right] = L_+[-2k^2Esnzcnz] = 0, \tag{2.40c}$$

$$L_-L_+\left[\varphi(z)\right] = L_-[2((k^2-2)E - 2(k^2-1)K)dnz] = 0. \tag{2.40d}$$

These results are used to derive some important properties of the operators $\mathbf{L}^\dagger$, L_+, and L_-, which are summarized in propositions 1 and 2.

Proposition 1 *Assume $N \in \mathbb{N}$ and $0 < k < 1$. The operator L_- is non-negative and self-adjoint, with $\ker(L_-) = span\{dnz\}$. The operator L_+ is self-adjoint, with $\ker(L_+) = span\{snzcnz\}$.*

Proof

One can directly verify that $L_-[dnz] = 0$. Because dnz has no zeros, $\lambda = 0$ is the first eigenvalue (listed in increasing order).

Again, one can verify that $L_+[snzcnz] = 0$. There is at most one function (up to a constant multiple) in $\ker(L_+)$ which is linearly independent of $w(z) = snzcnz$. Note that the natural domain for L_+ is $H^2_{\text{per}}[0, 2NK)$ and recall that functions in H^2_{per} are determined by their values on $[0, 2NK)$ and periodicity. For integer j, we have that $w(jK) = 0$ and $w'(jK) = (-1)^j$. Suppose that v is another solution of $L_+[v] = 0$. We have that $w(z)v'(z) - w'(z)v(z)$ is constant, so that $(v/w)' = d/w^2$ for some constant d on any interval where $w \neq 0$. Consider an interval of the form $(jK, (j+1)K)$ and let $x_j = (j + 1/2)K$. For $jK < z < (j+1)K$, we have

$$v(z) = c_j w(z) + d_j w(z) \int_{x_j}^{z} \frac{dy}{w^2(y)} \ . \tag{2.41}$$

Let

$$\tilde{w}_j(z) = w(z) \int_{x_j}^{z} \frac{dy}{w^2(y)} \tag{2.42}$$

be defined on each interval $(jK, (j+1)K)$. It can be verified that the limit of $\tilde{w}_j(z)$ exists as you approach either endpoint. In particular, we have

$$\lim_{z \to 2jK^+} \tilde{w}_{2j}(z) = \lim_{z \to 2jK^-} \tilde{w}_{2j-1}(z) = -1 \ ,$$

$$\lim_{z \to (2j+1)K^-} \tilde{w}_{2j}(z) = \lim_{z \to (2j+1)K^+} \tilde{w}_{2j+1}(z) = \frac{1}{\sqrt{1-k^2}} \ .$$

Because w is zero at all of these endpoints, we see that for v to be continuous, the d_j should all be equal. Without loss of generality, we set $d_j = 1$ for all j.

While the derivatives are still defined at the endpoints, they are not so well behaved. We have that

$$\begin{aligned} j_1 &:= \lim_{z \to 2jK^+} \tilde{w}'_{2j}(z) - \lim_{z \to 2jK^-} \tilde{w}'_{2j-1}(z) \\ &= \frac{2}{1-k^2}\left((1-k)^{3/2} - 1 + (2-k^2)E(K/2,k) - (1-k^2)K\right) , \\ j_2 &:= \lim_{z \to (2j+1)K^+} \tilde{w}'_{2j+1}(z) - \lim_{z \to (2j+1)K^-} \tilde{w}'_{2j}(z) \\ &= \sqrt{1-k^2}\left(j_1 - \frac{2(2-k^2)E - 4(1-k^2)K}{1-k^2}\right) . \end{aligned}$$

Note that, for $0 < k < 1$, $j_1 \neq j_2$. To enforce that v has continuous derivatives, we then obtain the following system of equations

$$\begin{aligned} c_1 - c_0 &= -j_1 \\ c_2 - c_1 &= j_2 \\ c_3 - c_2 &= -j_1 \\ &\vdots \\ c_{2N-1} - c_{2N-2} &= -j_1 \\ c_0 - c_{2N-1} &= j_2 . \end{aligned}$$

By summing all of the equations, we obtain that $0 = N(j_2 - j_1) \neq 0$, so that the equations are inconsistent. Therefore, there is no such v with a continuous derivative, i.e. there is no such v in $H^2_{\text{per}}[0, 2NK)$. Note that for the case $k = 0$, we see that $j_1 = j_2$ so that such a v does exist, as expected.

Proposition 2 *Assume $N \in \mathbb{N}$ and $0 < k < 1$ and let $(f, g)^T \in H^1_{\text{per}} \times H^1_{\text{per}}$. If the following*

orthogonality relations hold

$$\langle f, dnz\rangle \;\; = 0 \; , \tag{2.43a}$$

$$\langle f, \phi(z)\rangle \;\; = 0 \; , \tag{2.43b}$$

$$\langle g, snzcnz\rangle \;\; = 0 \; , \tag{2.43c}$$

$$\langle g, \varphi(z)\rangle \;\; = 0 \; , \tag{2.43d}$$

then $(f, g)^T \in \mathcal{M}$.

Proof

From Proposition 1, we have that

$$\ker(\mathbf{L}^\dagger) = span\{(dnz, 0)^T, (0, snzcnz)^T\} \; . \tag{2.44}$$

Recall the definitions of ϕ and φ:

$$\phi(z) = (KE(z,k) - Ez)\, dnz - k^2 snzcnz, \tag{2.45a}$$

$$\begin{aligned}\varphi(z) = {} & k^2 cnzsnz(KE(z,k) - Ez) + (E-K)dnz \\ & + k^2 Kcn^2 z dnz.\end{aligned} \tag{2.45b}$$

It can be verified that

$$L_+ L_-[\phi(z)] = L_+\left[-2k^2 Esnzcnz\right] = 0, \tag{2.46a}$$

$$L_- L_+[\varphi(z)] = L_-[2((k^2-2)E - 2(k^2-1)K)dnz] = 0. \tag{2.46b}$$

Therefore,

$$\ker((\mathbf{L}^\dagger)^2) = span\{(dnz, 0)^T, (0, snzcnz)^T, (\phi(z), 0)^T, (0, \varphi(z))^T\} \; . \tag{2.47}$$

Suppose that $(f, g)^T \in \ker((\mathbf{L}^\dagger)^3)$. Then, formally,

$$f = c_1 L_-^{-1}\varphi(z) + c_2\phi(z) + c_3 dnz \; , \tag{2.48}$$

$$g = c_4 L_+^{-1}\phi(z) + c_5\varphi(z) + c_6 snzcnz \; , \tag{2.49}$$

where the inverses above denote a particular solution of the corresponding inhomogeneous ODE. Consider $L_-^{-1}\varphi(z)$. Note that the Fredholm alternative implies that

$$0 = \langle k^2 cnzsnz(KE(z,k) - Ez) + (E-K)dnz, dnz\rangle + \langle k^2 Kcn^2 zdnz, dnz\rangle \tag{2.50}$$

$$= N(E^2 + (k^2-1)K^2)\ . \tag{2.51}$$

For $0 < k < 1$, the expression $E^2 + (k^2-1)K^2 > 0$, a contradiction. Therefore, there is no such particular solution. Similarly, consider $L_+^{-1}\phi(z)$. The Fredholm alternative implies that

$$0 = \langle (KE(z,k) - Ez)\, dnz - k^2 Ksnzcnz, snzcnz\rangle \tag{2.52}$$

$$= -\frac{N}{k^2}\left(E^2 + (k^2-1)K^2\right)\ , \tag{2.53}$$

again, a contradiction. Therefore,

$$\ker_g(\mathbf{L}^\dagger) = \ker((\mathbf{L}^\dagger)^2)\ . \tag{2.54}$$

2.4.2 Bounding the evolution of w_1 ($N = 1$)

Following the analysis of Weinstein [148], the evolution of the term $w_1 = R + iI$ is bounded by considering the function

$$Q(f,g) = -\frac{\beta}{2}B^2[\langle L_+ f, f\rangle + \langle L_- g, g\rangle]\ , \tag{2.55}$$

which is a conserved quantity along the solution trajectory for w_1, i.e. $dQ(R,I)/dt = 0$. For $(R,I)^T \in \mathcal{M}$, we have the following bound.

Proposition 3 *Assume $N = 1$. Let $w = R + iI \in \mathcal{M}$. Then there exist constants C_1 and C_2 such that*

$$C_1\left(\|R\|^2_{H^1_{\text{per}}} + \|I\|^2_{H^1_{\text{per}}}\right) \leq Q(R,I)\ , \tag{2.56}$$

$$C_2\left(\|R\|^2_{H^1_{\text{per}}} + \|I\|^2_{H^1_{\text{per}}}\right) \geq Q(R,I)\ . \tag{2.57}$$

This proposition is the primary result needed in our analysis: if the slow evolution of the parameters B, ξ, x_0, and σ is such that $(R(t), I(t))^T \in \mathcal{M}$, then for any T_0 we have $\sup_{0\leq t\leq T_0/\epsilon}$

$\|\epsilon w_1(t)\|_{H^1_{\rm per}} \to 0$ as $\epsilon \to 0$. See [148] for details. A proof of Proposition 3 based on a variational formulation can be found in [56]. A more classical proof modeled after [148] is provided as follows.

Proof

The existence of C_2 is simple to establish. To establish the existence of C_1, we require the following two lemmas. Note that for the remainder of these statements, we assume that $N = 1$.

Lemma 1 *Suppose that* $\langle f, dnz\rangle = 0$ *and* $\langle f, \phi(z)\rangle$. *Then there exists a positive constant* C_1^+ *such that*

$$\langle L_+ f, f\rangle \geq C_1^+ \|f\|_{L^2}^2 \ . \tag{2.58}$$

Lemma 2 *Suppose that* $\langle g, snzcnz\rangle = 0$ *and* $\langle g, \varphi(z)\rangle = 0$. *Then there exists a positive constant* C_1^- *such that*

$$\langle L_- g, g\rangle \geq C_1^- \|g\|_{L^2}^2 \ . \tag{2.59}$$

Suppose that $\langle f, dnz\rangle = 0$, $\langle f, \phi(z)\rangle$, $\langle g, snzcnz\rangle = 0$, and $\langle g, \varphi(z)\rangle = 0$. Let C_1^+ and C_1^- be as in Lemmas 1 and 2, respectively. Then

$$\langle L_+ f, f\rangle + 6\|f\|_{L^2} + \langle L_- g, g\rangle + 2\|g\|_{L^2} \tag{2.60}$$

$$= \|\frac{d}{dz} f\|_{L^2} + 6\langle (1 - dn^2 z) f, f\rangle + (2 - k^2)\|f\|_{L^2} \tag{2.61}$$

$$+ \|\frac{d}{dz} g\|_{L^2} + 2\langle (1 - dn^2 z) g, g\rangle + (2 - k^2)\|g\|_{L^2} \ , \tag{2.62}$$

$$\geq \|f\|_{H^1_{\rm per}} + \|g\|_{H^1_{\rm per}} \ . \tag{2.63}$$

Therefore, the proposition holds with

$$C_1 = \min\left(\frac{1}{1 + \frac{6}{C_1^+}}, \frac{1}{1 + \frac{2}{C_1^-}}\right) \ . \tag{2.64}$$

Proof of Lemma 1

In the following, we repeat the argument of [148], making appropriate changes to handle the periodic case. First, we note that by Theorem 3.1 of Chapter 8 in [28], L_+ has one negative eigenvalue (when $N = 1$) with a corresponding eigenfunction f_0, which we take to be nonnegative without loss of generality. Define

$$\gamma_1 = \min_f \langle L_+ f, f\rangle \ , \ \text{where } \|f\|_2 = 1, \ \langle f, dnz\rangle = 0 \ . \tag{2.65}$$

Then, by Lemma E.1 of [148], we have that $\gamma_1 \geq 0$ if

$$\langle L_+^{-1} dnz, dnz\rangle \leq 0 \ , \tag{2.66}$$

which is straightforward to verify using arguments similar to those in the proof of Proposition 2. Therefore, $\gamma_1 \geq 0$. The lemma is then proved if we can show that $\gamma_2 = \inf_f \langle L_+ f, f\rangle$ with f restricted such that $\|f\|_{L^2} = 1$, $\langle f, dnz\rangle = 0$, and $\langle f, \phi(z)\rangle = 0$ is non-zero, as $\gamma_2 \geq \gamma_1 \geq 0$.

Suppose that $\gamma_2 = 0$. Let f_m be a minimizing sequence of $\langle L_+ f, f\rangle$ satisfying $\|f_m\|_{L^2} = 1$, $\langle f_m, dnz\rangle = 0$, and $\langle f_m, \phi(z)\rangle = 0$. Given $\delta > 0$, there exists a $M(\delta)$ such that

$$0 < \int_{-K(k)}^{K(k)} \left(\frac{d}{dz} f_m\right)^2 dz + (2 - k^2) \int_{-K(k)}^{K(k)} f_m^2 \, dz \tag{2.67}$$

$$\leq 6 \int_{-K(k)}^{K(k)} dn^2 z f_m^2 \, dz + \delta \ , \tag{2.68}$$

for all $m \geq M(\delta)$. In particular, the sequence f_m is uniformly bounded in the H^1_{per} norm. Therefore, there is a subsequence of f_m which converges weakly to an H^1_{per} function f_*. This function satisfies the constraints $\langle f_*, dnz\rangle = 0$ and $\langle f_*, \phi(z)\rangle = 0$ by weak convergence. Because H^1_{per} is compactly embedded in L^2, there exists a further subsequence, which we denote by f_{m_j}, that converges in the L^2 norm (to f_*). Therefore, $\|f_*\|_{L^2} = 1$.

Let h be such that $\|h\|_2 = 1$. Note that $\langle h, f_*'\rangle = \lim \langle h, f_{m_j}'\rangle \leq \liminf \|f_{m_j}'\|_{L^2}$ by weak convergence in H^1_{per}. Taking the maximum over all such h implies that $\|f_*'\|_{L^2} \leq \liminf \|f_{m_j}'\|_{L^2}$. Combining this with the L^2 convergence of f_{m_j} gives that $\langle L_+ f_*, f_*\rangle \leq \liminf \langle L_+ f_{m_j}, f_{m_j}\rangle = 0$, so that $\langle L_+ f_*, f_*\rangle = 0$.

Because f_* attains the minimum and is admissible, there exists a critical point of the problem

$$(L_+ - \lambda_1)f = \lambda_2 dnz + \lambda_3 \phi(z) \ , \tag{2.69}$$

$$\|f\|_2 = 1 \ , \tag{2.70}$$

$$\langle f, dnz \rangle = 0 \ , \tag{2.71}$$

$$\langle f, \phi(z) \rangle = 0 \ , \tag{2.72}$$

of the form $(f_*, \lambda_1, \lambda_2, \lambda_3)$. Taking the inner product of f_* with Eq. (2.69), we obtain that $\lambda_1 = \langle L_+ f_*, f_* \rangle = 0$. This implies that

$$L_+ f_* = \lambda_2 dnz + \lambda_3 \phi(z) \ . \tag{2.73}$$

Taking the inner product of $snzcnz$ with Eq. (2.73), we obtain that $\lambda_3 = 0$. Following the arguments in the proof of Proposition 2, this implies that

$$f_* = \frac{\lambda_2}{2((k^2-2)E - 2(k^2-1)K)} \varphi(z) + \lambda_4 snzcnz \ , \tag{2.74}$$

for some λ_4. The constraint $\langle f_*, \phi(z) \rangle = 0$ implies that $\lambda_4 = 0$ and the constraint $\langle f_*, dnz \rangle = 0$ implies that $\lambda_2 = 0$. We have that $f_* \equiv 0$, a contradiction. Therefore, $\gamma_2 > 0$, proving the lemma.

Proof of Lemma 2

This lemma can be proved using arguments similar to the above.

2.4.3 Modulation equations for the dn solution ($N = 1$)

For the *dn* solution,

$$\begin{aligned} \partial_\tau (\hat{u}_0) = \sqrt{-\beta} B_\tau dnz + A \frac{dk}{dB} B_\tau dn_k z \\ + A[B_\tau (x - x_0) - B x_{0\tau}] dn_z z \ . \end{aligned} \tag{2.75}$$

We consider solutions with $k \to 1$, so that $dk/dB \approx 0$. Using this approximation, the above reduces to

$$\partial_\tau \left(\hat{u}_0\right) = \sqrt{-\beta} B_\tau dnz - Ak^2 snzcnz \left(\frac{B_\tau}{B} z - Bx_{0\tau}\right) \ , \tag{2.76}$$

so that

$$\begin{aligned} \partial_\tau \left(u_0\right) = e^{i\psi}\sqrt{-\beta} B_\tau dnz - e^{i\psi} Ak^2 snzcnz \left(\frac{B_\tau}{B} z - Bx_{0\tau}\right) \\ + i\left(\xi_\tau \frac{z}{B} - \xi x_{0\tau} - \sigma_{0\tau}\right) e^{i\psi} Adnz. \end{aligned} \tag{2.77}$$

This gives the following expression for the forcing term

$$\begin{aligned} \Im(\hat{F}) = F\cos\psi + \Re(e^{-i\psi}G) - \sqrt{-\beta} B_\tau dnz - Adnz \\ + Ak^2 \left(\frac{B_\tau}{B} z - Bx_{0\tau}\right) snzcnz, \end{aligned} \tag{2.78}$$

$$\begin{aligned} \Re(\hat{F}) = F\sin\psi - \Im(e^{-i\psi}G) + \sqrt{-\beta}\xi_\tau z dnz \\ - (\xi x_{0\tau} + \sigma_{0\tau}) Adnz \ . \end{aligned} \tag{2.79}$$

To constrain the forcing term $(\Im(\hat{F}), \Re(\hat{F}))^T$ to be in $\mathcal{M}$, Proposition 2 implies the following constraints

$$\langle \Im(\hat{F}), dnz \rangle = 0, \tag{2.80a}$$

$$\langle \Im(\hat{F}), \phi(z) \rangle = 0, \tag{2.80b}$$

$$\langle \Re(\hat{F}), snzcnz \rangle = 0, \tag{2.80c}$$

$$\langle \Re(\hat{F}), \varphi(z) \rangle = 0. \tag{2.80d}$$

These constraints require the slow evolution of the parameters to satisfy the following system of differential equations

$$\frac{dB}{d\tau} = \frac{\langle \Re(e^{-i\psi}G) + F\cos\psi, dnz\rangle - \sqrt{|\beta|}B\langle dnz, dnz\rangle}{\sqrt{|\beta|}(\langle dnz, dnz\rangle - k^2\langle zsnzcnz, dnz\rangle)}\,, \tag{2.81a}$$

$$\frac{dx_0}{d\tau} = \frac{\langle F\cos\psi + \Re(e^{-i\psi}G), \phi(z)\rangle}{\sqrt{|\beta|}B^2k^2\langle snzcnz, \phi(z)\rangle}\,, \tag{2.81b}$$

$$\frac{d\xi}{d\tau} = -\frac{\langle F\sin\psi - \Im(e^{-i\psi}G), snzcnz\rangle}{\sqrt{|\beta|}\langle zdnz, snzcnz\rangle}\,, \tag{2.81c}$$

$$\frac{d\sigma_0}{d\tau} + \xi\frac{dx_0}{d\tau} = \frac{\langle F\sin\psi - \Im(e^{-i\psi}G), \varphi(z)\rangle}{\sqrt{|\beta|}B\langle dnz, \varphi(z)\rangle}\,, \tag{2.81d}$$

where $\psi = \xi z/B + \sigma - \sigma_0$. We can further simplify the equations above by applying trigonometric identities, we have

$$\frac{dB}{d\tau} = \frac{\langle \Re(e^{-i\psi}G), dnz\rangle + F\cos(\sigma-\sigma_0)p_1(\xi)}{\sqrt{|\beta|}(q_1(k) - k^2q_2(k))} - \frac{\sqrt{|\beta|}B\langle dnz, dnz\rangle}{\sqrt{|\beta|}(q_1(k) - k^2q_2(k)}\,, \tag{2.82a}$$

$$\frac{dx_0}{d\tau} = \frac{\langle \Re(e^{-i\psi}G), \phi(z)\rangle - F\sin(\sigma-\sigma_0)p_2(\xi)}{\sqrt{|\beta|}B^2k^2q_3(k)}\,, \tag{2.82b}$$

$$\frac{d\xi}{d\tau} = \frac{\langle \Im(e^{-i\psi}G), snzcnz\rangle - F\cos(\sigma-\sigma_0)p_3(\xi)}{\sqrt{|\beta|}q_2(k)}\,, \tag{2.82c}$$

$$\frac{d\sigma_0}{d\tau} + \xi\frac{dx_0}{d\tau} = \frac{F\sin(\sigma-\sigma_0)p_4(\xi) - \langle \Im(e^{-i\psi}G), \varphi(z)\rangle}{\sqrt{|\beta|}Bq_4(k)}\,, \tag{2.82d}$$

where

$$p_1(\xi) = \langle \cos(\xi z/B), dnz\rangle\,, \tag{2.83a}$$

$$p_2(\xi) = \langle \sin(\xi z/B), \phi(z)\rangle\,, \tag{2.83b}$$

$$p_3(\xi) = \langle \sin(\xi z/B), snzcnz\rangle\,, \tag{2.83c}$$

$$p_4(\xi) = \langle \cos(\xi z/B), \varphi(z)\rangle\,, \tag{2.83d}$$

and

$$q_1(k) = \langle dnz, dnz \rangle \tag{2.84a}$$

$$q_2(k) = \langle zdnz, snzcnz \rangle \tag{2.84b}$$

$$q_3(k) = \langle snzcnz, \phi(z) \rangle \tag{2.84c}$$

$$q_4(k) = \langle dnz, \varphi(z) \rangle \ . \tag{2.84d}$$

In addition to these constraints, ξ should be an integer so that u_0 remains in H^1_{per}. Therefore the analysis is only rigorous when applied to perturbations for which $d\xi/d\tau = 0$, but we have found that the analysis provides insight in other cases.

Consider the stability of this system of differential equations around the center frequency, i.e. $\xi = 0$, so that $\psi = \sigma - \sigma_0$ and $p_2(\xi) = p_3(\xi) = 0$. For $k \approx 1$, we can approximate many of the inner products in the above expressions using the limiting forms of the Jacobi elliptic functions. We obtain the approximations $p_1(0) \approx \pi$, $p_4(0) \approx 0$, $q_1(k) \approx 2$, $q_2(k) \approx 1$, $q_3(k) \approx -1$, and $q_4(k) \approx 1$. With these approximations, the evolution equations simplify to

$$\frac{dB}{d\tau} = \frac{1}{\sqrt{|\beta|}}(\langle \Re(e^{-i\psi}G), dnz \rangle + F\pi\cos(\sigma - \sigma_0)) - 2B \ , \tag{2.85a}$$

$$\frac{dx_0}{d\tau} = -\frac{\langle \Re(e^{-i\psi}G), \phi(z) \rangle}{\sqrt{|\beta|}B^2} \ , \tag{2.85b}$$

$$\frac{d\xi}{d\tau} = \frac{1}{\sqrt{|\beta|}}\langle \Im(e^{-i\psi}G), snzcnz \rangle \ , \tag{2.85c}$$

$$\frac{d\sigma_0}{d\tau} + \xi\frac{dx_0}{d\tau} = -\frac{\langle \Im(e^{-i\psi}G), \varphi(z) \rangle}{\sqrt{|\beta|}B} \, . \tag{2.85d}$$

These slow evolution equations approximate the effect of a perturbation G on the microresonator comb.

2.4.4 Stability of dn solutions of the LLE (N = 1)

When the perturbation $G = 0$, the parameter evolution constraints Eq. (2.85) yield the following set of equations

$$\frac{dB}{d\tau} = \frac{F\pi\cos(\sigma-\sigma_0)}{\sqrt{|\beta|}} - 2B \ , \tag{2.86a}$$

$$\frac{dx_0}{d\tau} = 0 \ , \tag{2.86b}$$

$$\frac{d\xi}{d\tau} = 0 \ , \tag{2.86c}$$

$$\frac{d\sigma_0}{d\tau} + \xi\frac{dx_0}{d\tau} = 0 \ , \tag{2.86d}$$

which gives the solution with $B = F\pi\cos(\sigma-\sigma_0)/(2\sqrt{|\beta|})$ as a steady-state attractor to the dynamics. Specifically, values of B larger and smaller than this exponentially decay back to the steady-state value. In addition, the fast time scale dynamics give

$$\frac{dx_0}{dt} = -\beta\xi, \tag{2.87a}$$

$$\frac{d\sigma}{dt} = -\alpha - \frac{\beta}{2}B^2(2-k^2) - \frac{\beta}{2}\xi^2. \tag{2.87b}$$

Integrating the constant σ_0 into the second equation and setting $\xi = 0$, i.e. we are working around the center frequency, then

$$\frac{d(\sigma-\sigma_0)}{dt} = -\alpha - \frac{\beta}{2}B^2(2-k^2). \tag{2.88}$$

Since the first solvability condition gives the steady-state $B = F\pi\cos(\sigma-\sigma_0)/(2\sqrt{-\beta})$, then

$$\frac{d(\sigma-\sigma_0)}{dt} = -\alpha + \frac{F^2\pi^2(2-k^2)}{8}\cos^2(\sigma-\sigma_0) \ , \tag{2.89}$$

and

$$\cos(\sigma-\sigma_0) = \frac{2B\sqrt{-\beta}}{F\pi} \ , \tag{2.90}$$

which gives the time-independent phase of the microresonator comb. Specifically, the real part of the solution is $u_0 = Adn(B(x-x_0),k)\cos(\sigma-\sigma_0)$ and the imaginary part is $u_0 = Adn(B(x-x_0),k)\sin(\sigma-\sigma_0)$.

These asymptotic results show that $B \neq 0$ provided $F > 0$. Moreover, the stable microresonator solution has a fixed phase relation which does not evolve in time. Simulations show that these two predictions are accurate representations of the dynamics. More than that, the prediction here shows them to be attractors for general initial conditions, which is again borne out by simulation.

2.4.5 The case $N > 1$ in practice

Proposition 1 states that the nullspaces of L_+ and L_- are each spanned by one function, for any positive number of pulses N. However, in simulations of finite precision, this mathematical truth is not observed for $k \approx 1$. Indeed, the discretizations of these operators are observed to have N eigenfunctions corresponding to a zero (to numerical precision) eigenvalue when $k \approx 1$. Intuitively, this results from the fact that the dn function is nearly zero between pulses for $k \approx 1$ so that the pulses are essentially decoupled. Indeed, the set of N shifted copies of the eigenfunctions for $N = 1$, i.e. individual pulses in each of $[-K, K), [K, 3K), \ldots, [(2N-3)K, (2N-1)K)$, is seen to give a basis for these nullspaces, again to numerical precision.

Counterintuitively, it is this failure of Proposition 1 in practice which explains the predictive power of the modulation equations of the previous sections — which hold mathematically only when $N = 1$ — for numerical simulations with $N > 1$. In particular, for the LLE type perturbation alone ($G = 0$), we observe that the stabilizing effect on the amplitude of the comb as predicted by Eq.(2.86a) and the generation of a time independent phase as predicted by Eq.(2.90) for the $N = 1$ case also hold for $N > 1$ when $k \approx 1$. See Figures 2.7 and 2.8 for a comparison of the stability of a dn initial condition with and without the LLE terms, which we discuss in more detail in the next section. For nonzero G perturbations, as in the Raman effect and spontaneous emission noise examples below, the more qualitative $N = 1$ predictions are also observed numerically when $N > 1$. The fact that the behaviors of the pulses have decoupled is only apparent for the spontaneous emission noise example, as the perturbations acting on each pulse are identical in the other examples.

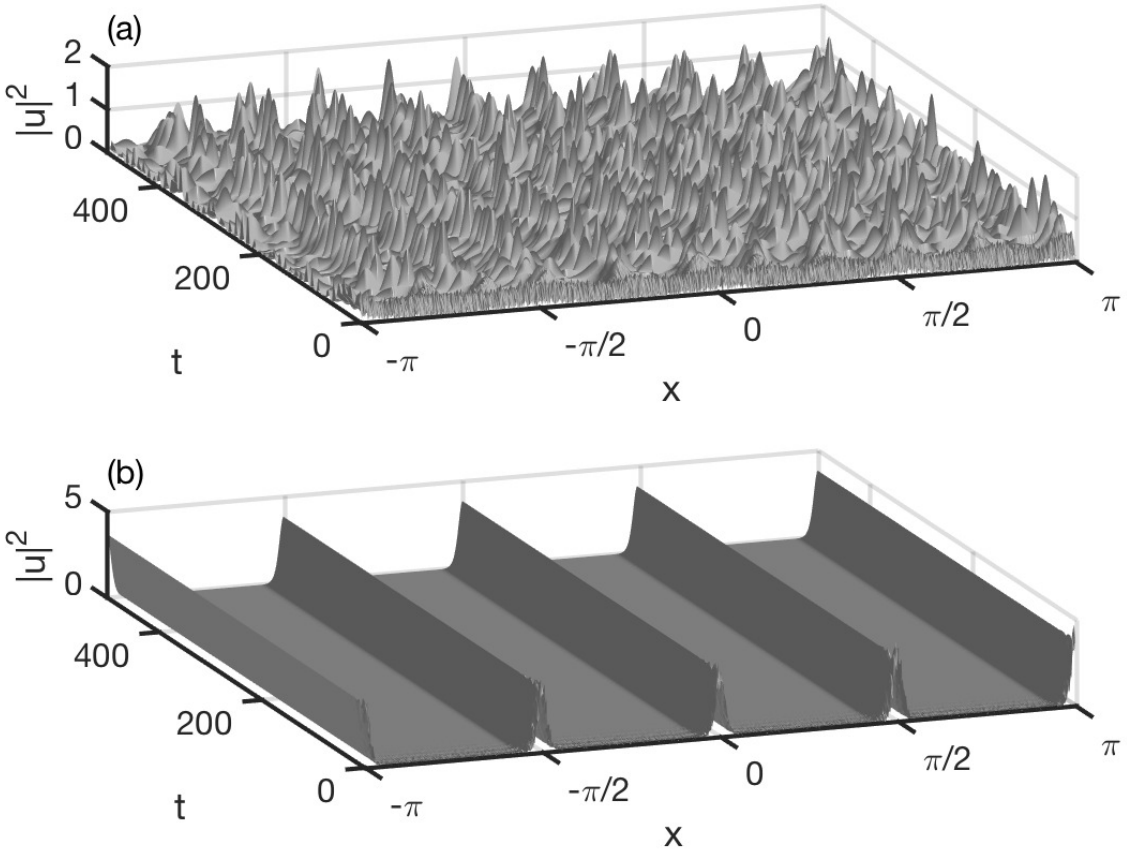

Figure 2.7: Numerical simulation of the ($N = 4$) dn solution of Eq.(2.13) with $\epsilon = 0.1$, $G = 0$, and the detuning α set to (a) $\alpha = 0.0593$ and (b) $\alpha = 1.8732$ so that the appropriate parameter for the initial waveform is (a) $k^2 = 0.9$ and (b) $k^2 = 1 - 10^{-12} \approx 1$, according to Eq.(2.26). The initial waveform was corrupted with white noises to induce instability in the evolution. The $k^2 = 0.9$ solution is shown to be unstable whereas the $k^2 = 1 - 10^{-12}$ solution is stable. This is consistent with our linear stability analysis and Fig. 2.5.

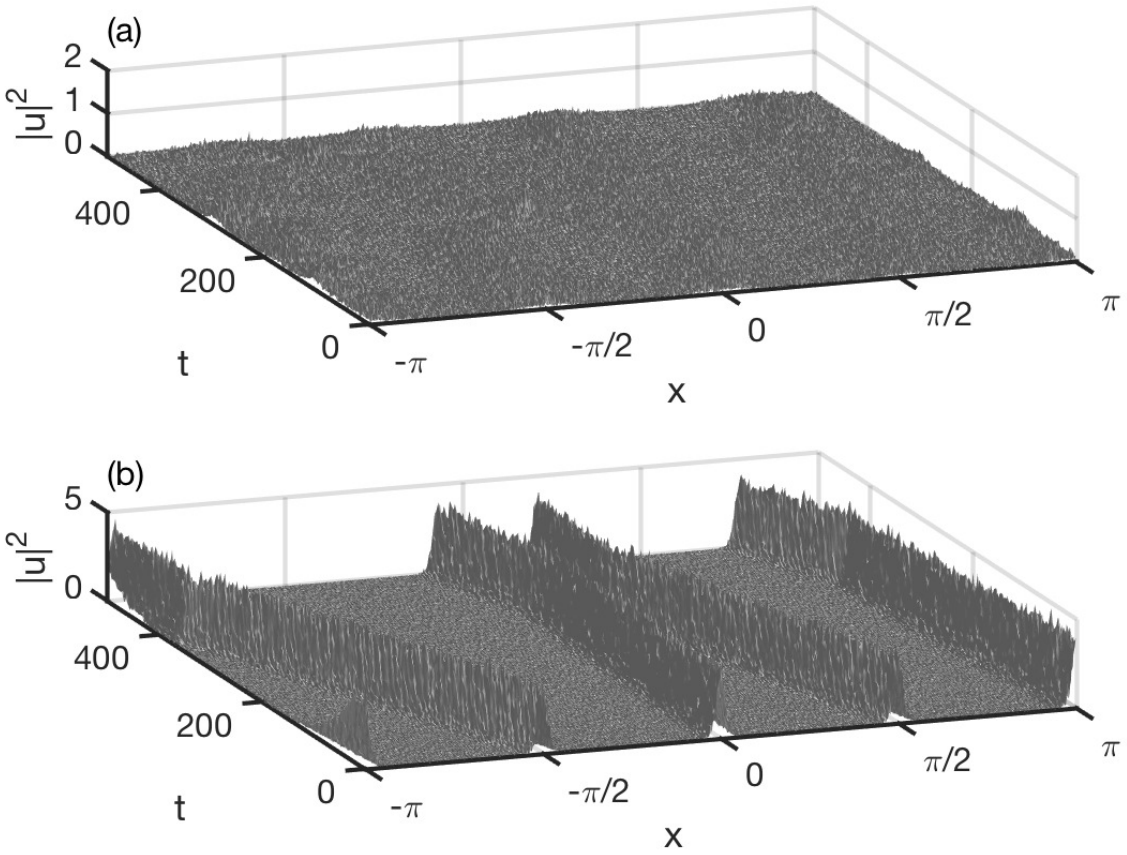

Figure 2.8: Numerical simulation of the ($N = 4$) *dn* solution of Eq.(2.13) with $\epsilon = 0$, $G = 0$, and the detuning α set to (a) $\alpha = 0.0593$ and (b) $\alpha = 1.8732$ so that the appropriate parameter for the initial waveform is (a) $k^2 = 0.9$ and (b) $k^2 = 1 - 10^{-12} \approx 1$, according to Eq.(2.26). The initial waveform was corrupted with the same white noises as Fig. 2.7 to induce instability in the evolution. Both the $k^2 = 0.9$ solution and the $k^2 = 1 - 10^{-12}$ solution are unstable. Comparing with Fig. 2.7, we observe that the $k^2 = 1 - 10^{-12}$ solution is stabilized by the LLE type perturbation.

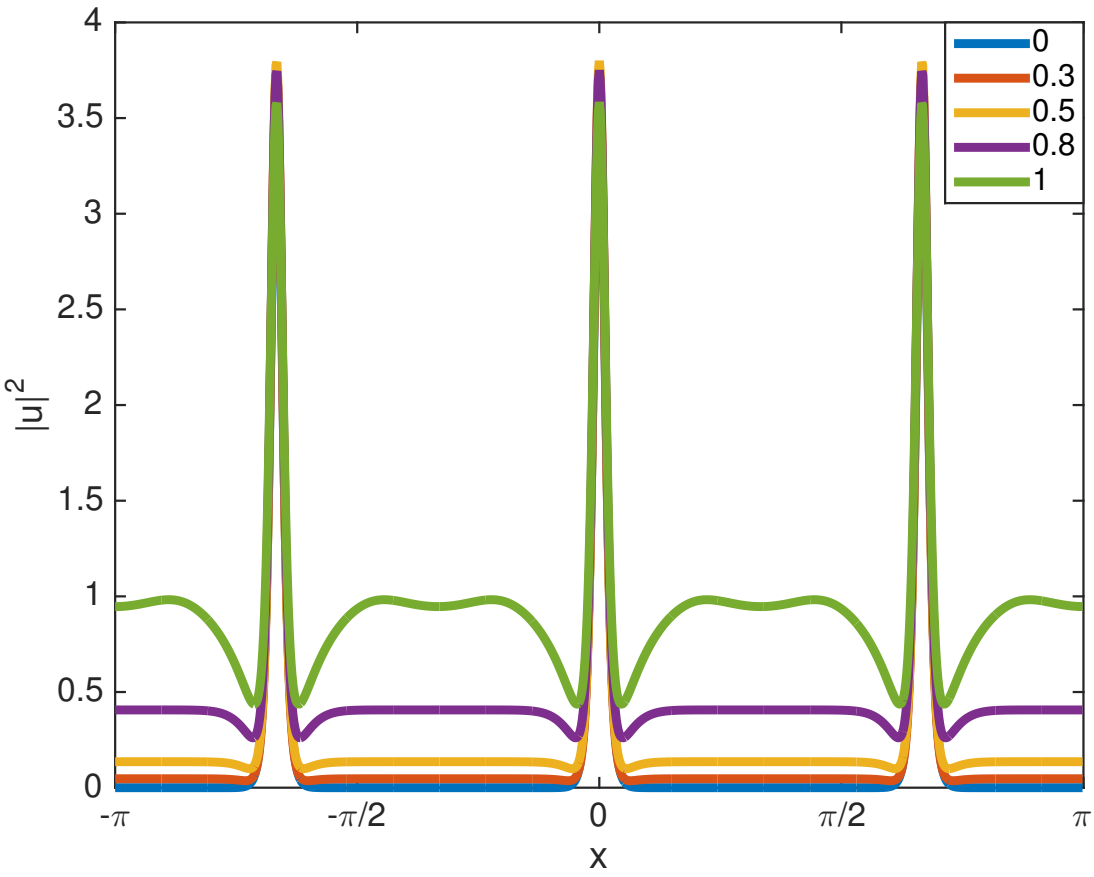

Figure 2.9: Stable numerical solutions of Eq.(2.13) with $G = 0$ and $\alpha = 1.7793$ for various values of ϵ. The initial waveform was set as a $(N = 3)$ dn solution with $k^2 = 1 - 10^{-16}$. As ϵ is increased from $\epsilon \ll 1$, the solutions deform from the asymptotic dn form to a localized structure that sits atop a shelf. Importantly, like the dn solution, the resulting evolution produces solutions which have no nodal separation between neighboring pulses.

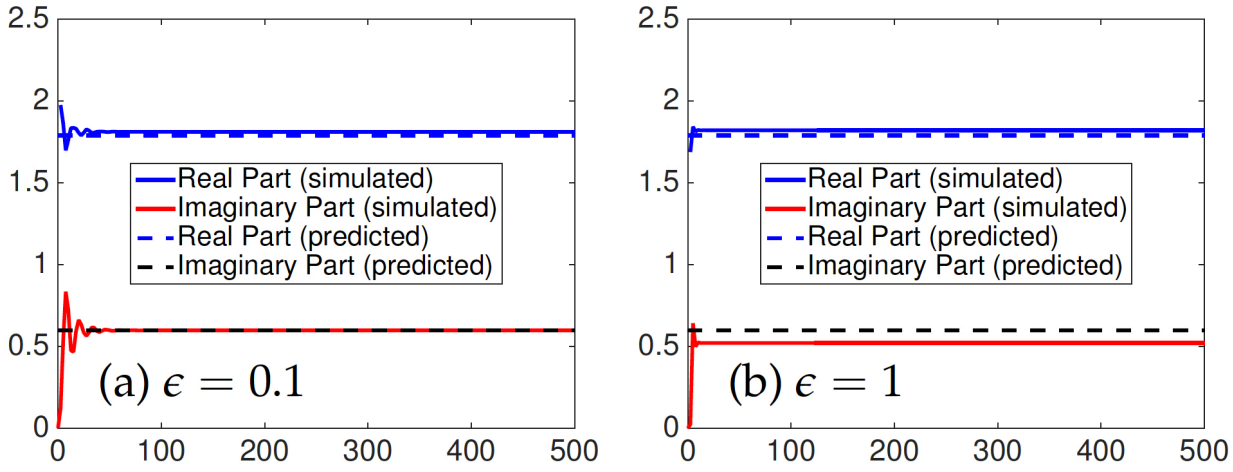

Figure 2.10: Evolution of the real and imaginary parts of a ($N = 3$) *dn* solution of Eq.(2.13) evaluated at $x = 0$, with $G = 0$, $\alpha = 1.7793$ (so that the initial waveform has $k^2 = 1-10^{-16}$), and ϵ set to (a) $\epsilon = 0.1$ and (b) $\epsilon = 1$. The dotted lines are the theoretically calculated real and imaginary parts that result from our perturbation theory, whereas the solid lines are from the direct LLE simulation. The perturbation theory holds remarkably well even at $\epsilon = 1$.

2.5 Numerical Simulations

In this section, we compare numerical simulations of Eq. (2.13) with predictions made by the theory outlined above. In all simulations the value of β is fixed, with $\beta = -0.01$. When $\epsilon \neq 0$, we set $F = (\rho(1 + (\rho - \alpha)^2))^{1/2}$ with $\rho = 0.95$ to remain in the right parameter space for the generation of frequency combs. The initial waveforms (u at time zero) are set according to Eq. (2.18) with $\xi = \sigma = \sigma_0 = x_0 = 0$ and the value of k determined by the detuning α as in Eq. (2.26). First, we simulate the LLE to show that the *dn* solution is stable, as opposed to the observed instability of the *cn* and *sn* solutions in Figure 2.2. Figure 2.7 shows the evolution of the *dn* solution for $\epsilon = 0.1$ and the detuning α chosen so that $k^2 = 0.9$ and $k^2 = 1 - 10^{-12} \approx 1$. Recall that for $k^2 = 0.9$ the linear stability analysis showed strong instability and for $k^2 = 1 - 10^{-12}$ the analysis showed weaker instability, see Figure 2.6. Further, recall that for both values of the parameter, the solution should be

unstable for generic perturbations of the equation. In both simulations, the initial waveforms are corrupted with white noises in order to induce instability if it exists. For $k^2 = 1 - 10^{-12}$, the pumping and damping terms of the LLE, i.e. the LLE-specific perturbations, have stabilized the *dn* solution. The $k^2 = 0.9$ solution is still unstable with this perturbation. In Fig. 2.8, we repeat these calculations without the LLE perturbation, i.e. setting $\epsilon = 0$. The $k^2 = 1 - 10^{-12}$ solution is seen to be less stable than that in Fig. 2.7.

In Fig. 2.9, we plot equilibrated solutions of Eq. (2.13) as ϵ is increased. In this example, the ($N = 3$) *dn*-type solutions for $k^2 = 1 - 10^{-16}$ remain stable, even for large values of ϵ. Note that the solutions deform away from the original *dn* waveform and develop a pedestal as ϵ is increased. Finally, Fig. 2.10 contains plots of the predicted time-independent phase, determined by Eq. (2.90), and the phase of a simulated microresonator solution with a *dn* initial waveform, showing good agreement between theory and simulation.

2.5.1 Raman term

An important modification to the LLE equation is the addition of the Raman effect which is known to induce a self-frequency shift in the microresonator [74, 105]. The Raman effect is included in the LLE as part of the perturbation term $G(u, x, t)$ in Eq. (2.13). Letting U denote the waveform and $G(U)$ denote the Raman perturbation in physical units, we have [74]

$$G(U) = i\left[-f_R|U|^2 + f_R h_R \bigotimes |U|^2\right] U \approx -i\left[f_R \tau_R \frac{\partial |U|^2}{\partial x}\right] U, \tag{2.91}$$

where the constants f_R and τ_R are the Raman fraction and the Raman shock time, respectively, and $\bigotimes$ denotes a convolution. In simulations, the Raman response function h_R is typically chosen to be [9]

$$h_R(x) = \frac{\tau_1^2 + \tau_2^2}{\tau_1 \tau_2^2} e^{-x/\tau_2} \sin(x/\tau_1), \tag{2.92}$$

where $\tau_1 = 12.2fs$ and $\tau_2 = 32fs$. In our numerical simulation of the dimensionless LLE, Eq. (2.13), the Raman term becomes $G(u) = -iC\frac{\partial |u|^2}{\partial x} u$, where $C = 0.001$.

The effect of the Raman perturbation of Eq. (2.91) can be substituted into the modula-

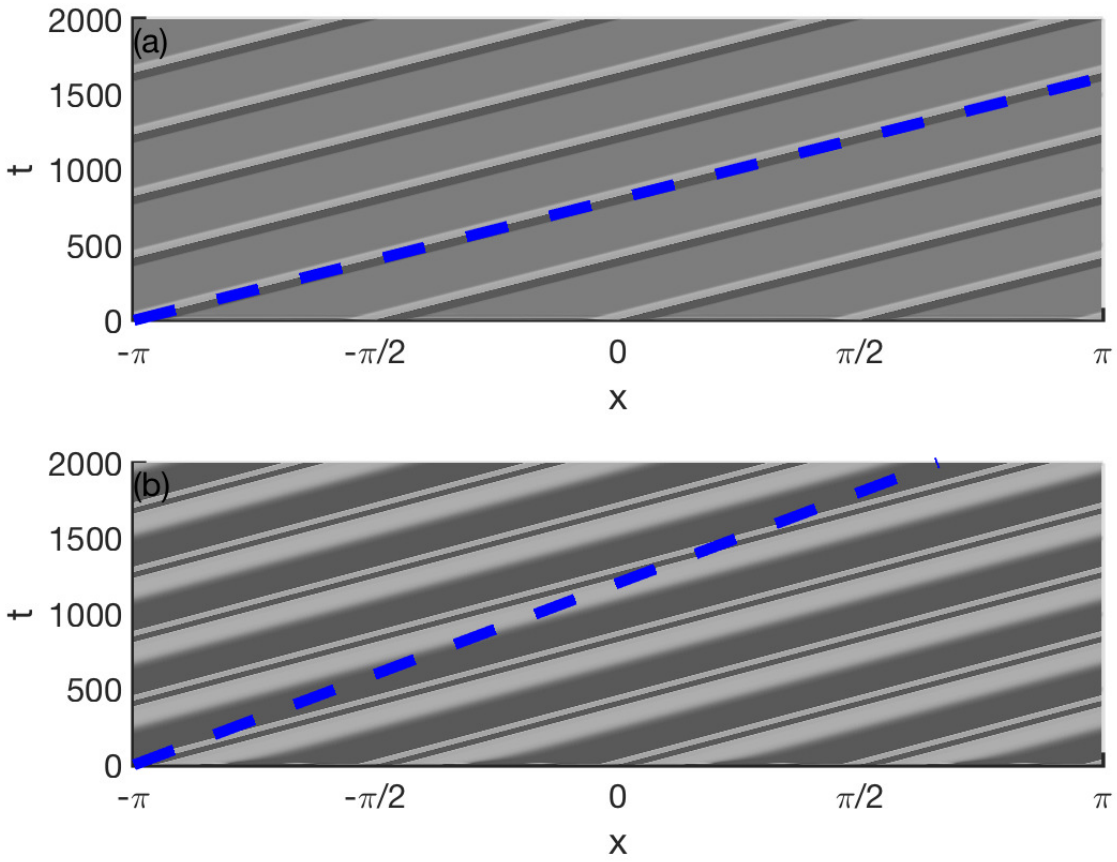

Figure 2.11: Top view of a numerical simulation of Eq.(2.13) with $\alpha = 1.8732$ and the addition of the Raman effect of Eq. (2.91). The perturbation parameter ϵ is set to (a) $\epsilon = 0.1$ and (b) $\epsilon = 1$. As predicted and quantified by our perturbation theory, the *dn* solution remains stable despite the induced drift of the solution. The drift velocity is compared with that computed from our theory using self-frequency shift in both cases. The dotted lines represent the theoretically calculated trajectories of the drift of the solutions. The perturbation theory holds well when ϵ is small.

tion constraints of Eq. (2.85) to evaluate the impact on the comb dynamics. The symmetry properties of the perturbation play a large role in determining the resulting behavior. Specifically, symmetry considerations yield

$$\frac{dx_0}{d\tau} = 0 \,, \tag{2.93a}$$

$$\frac{d\sigma_0}{d\tau} = 0 \,, \tag{2.93b}$$

with the additional constraints that

$$\frac{dB}{d\tau} = \frac{F\pi\cos(\sigma-\sigma_0)}{\sqrt{-\beta}} - 2B \,, \tag{2.94a}$$

$$\frac{d\xi}{d\tau} = \frac{\langle 2CBA^3k^2dn^2zsnzcnz, snzcnz\rangle}{\sqrt{-\beta}} \neq 0. \tag{2.94b}$$

This determines the self-frequency shift induced by the Raman term since the value of ξ gives the shift from the center frequency used to derive the LLE. In addition to the self-frequency shift, it should be recalled that

$$\frac{dx_0}{dt} = -\beta\xi \,. \tag{2.95}$$

As the term ξ is slowly evolving, it can be thought of as a constant over short time intervals so that the self-frequency shift generates a linear translation of the solution with a group velocity determined by the Raman term. Importantly, the Raman term does not destabilize the comb, rather it simply shifts it in frequency and forces a translation.

In Fig. 2.11, we plot simulations of the LLE with the addition of the Raman effect, i.e. $G(u) = -iC\frac{\partial|u|^2}{\partial x}u$, for both $\epsilon = 0.1$ and $\epsilon = 1$. The comb quickly forms and the induced translation is readily apparent. We also plot a line corresponding to the predicted drift velocity $dx_0/dt = -\beta\xi$. As noted above, only integer values of ξ are allowed by the model. Nonetheless, the frequency shift that ξ represents can be estimated from the simulation, and need not be integer valued. In particular, we take the empirical value of ξ to be the center of mass of the Fourier coefficients of the simulated waveform (computed using the FFT). After the first few time steps, this value holds steady at approximately $\xi = 0.3890$ for the $\epsilon = 0.1$ simulation and $\xi = 0.2608$ for the $\epsilon = 1$ simulation. The theoretical drift velocity matches

well with the observed drift velocity of the simulation when $\epsilon = 0.1$, whereas, for $\epsilon = 1$, the prediction is not quantitatively satisfactory but corresponds to the qualitative behavior of the simulation (note that $\epsilon = 1$ is far from the asymptotic regime).

2.5.2 Spontaneous emission noise

Spontaneous emission noise from pumping/amplification has always been a significant source of performance limitations in optical systems. For instance, in optical communication systems, the noise from amplification results in the Gordon-Haus timing jitter [54] which imposes a fundamental limit on transmission lengths for a given bit-error-rate constraint in lightwave communication systems. Soliton perturbation theory provided the fundamental calculation of this limitation. It also provided a number of engineering design strategies for trying to overcome the Gordon-Haus limitations, including sliding filters [102, 107] and dispersion management [140, 129, 90].

The LLE perturbation theory developed here can also be used to evaluate the effects of spontaneous emission noises in the microresonator, something that has only recently been studied experimentally [62, 96]. Specifically, for this case the perturbation in Eq. (2.13) takes the form

$$G(u, x, t) = S(x, t) \ , \tag{2.96}$$

where $S(x, t)$ is a white noise process modeling the spontaneous emission [148]. In this case, for a specific realization of noise, the effects on the LLE comb parameters can be evaluated using Eq. (2.85). Generically, the noise generates amplitude, phase, center-position and center-frequency jitter. But the most pronounced effect comes from the fast scale dependency of the center position on the center frequency. Thus the evolution

$$\frac{d\xi}{d\tau} = \frac{1}{\sqrt{-\beta}}(\langle \Re(e^{-i\psi} S(x, t)), snzcnz \rangle) \tag{2.97}$$

produces a center frequency with mean $\langle \xi \rangle$ and variance $\langle \xi^2 \rangle$ which then drives the center position through the relation $dx_0/dt = -\beta\xi$. As with the Gordon-Haus jitter, this produces a jitter in the pulse position, leading to a degradation in performance. Figure 2.12 provides

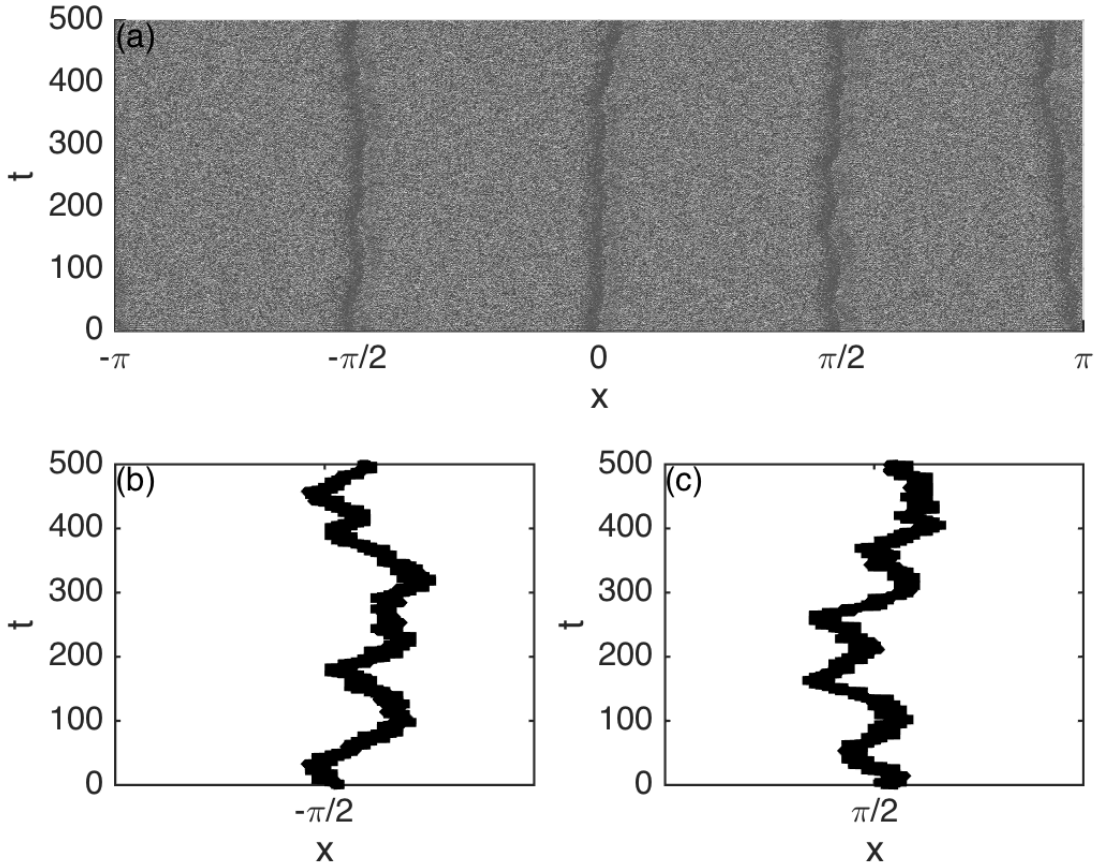

Figure 2.12: (a) Top view of a numerical simulation of Eq.(2.13) with $\epsilon = 0.1$, $\alpha = 1.8732$, and the addition of spontaneous emission noises as defined in Eq.(2.96). As predicted and quantified by our perturbation theory, the *dn* solution remains stable despite the induced random walk (drift) of the individual pulse solutions. Much like the Gordon-Haus jitter, our perturbation theory captures the effect of the timing variance of individual pulses. To highlight the random walk of each pulse, panels (b) and (c) show a detail of the pulses near $x = -\pi/2$ and $x = \pi/2$ respectively.

a simulation of the LLE under the influence of white noise perturbations Eq. (2.96). Note that the comb is stable, with fluctuations induced in the various solution parameters. Most notably, the zoom in of the individual pulses shows the random-walk generated as a result of the noise. As with Gordon-Haus jitter, the statistics of this random walk could be evaluated with the LLE perturbation theory we have developed.

2.5.3 Gaussian noises in the pump

The LLE perturbation theory developed here can also characterize the intra-cavity dynamics when the enforcing pump is corrupted by Gaussian shaped nosies in spectrum, which has been recently observed experimentally.

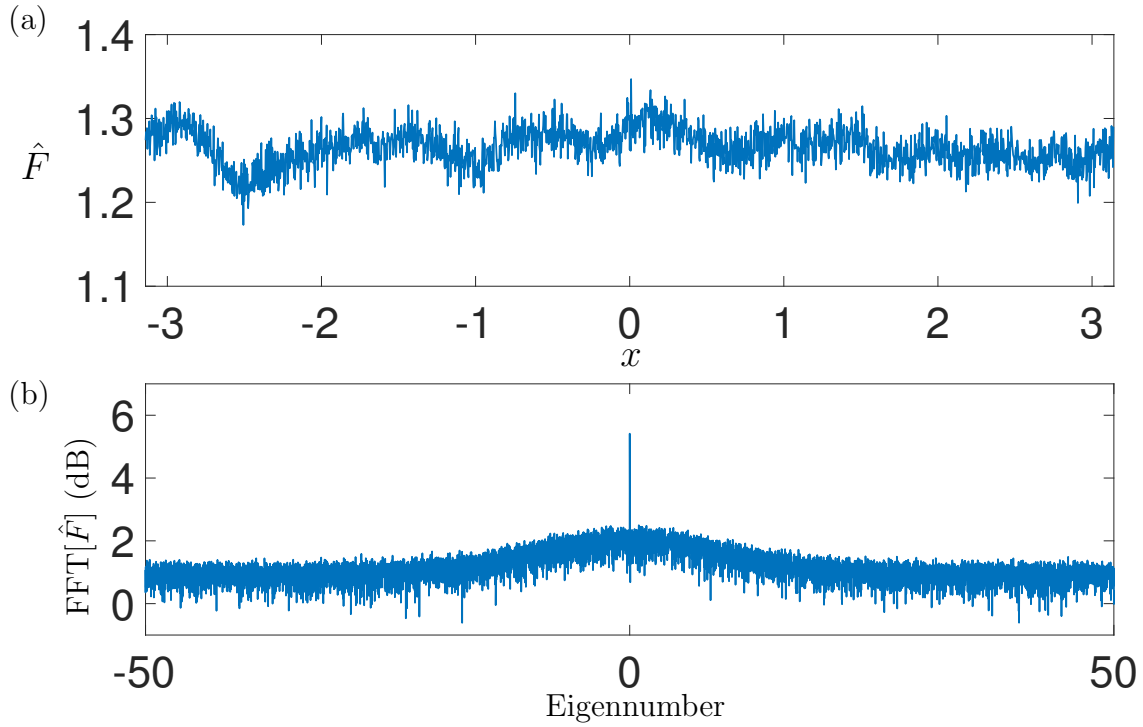

Figure 2.13: Noise-corrupted pump $\hat{F}$ in (a) time domain and (b) spectrum domain.

To be consistent with the experimental observations, we model the noises in the form of $G(u, x, t)$ as follows. The enforcing pump F is corrupted by white noises in spectrum. A

Gaussian filter is then applied to the noise-corrupted pump spectrum in the log scale, with controllable amplitude and width, to get the noise-corrupted pump $\hat{F}$, as shown in Fig. 2.13. The perturbation in Eq. (2.13) thus takes the form

$$G(u,x,t) = \hat{F}(x,t) - F. \tag{2.98}$$

Considering both fast and slow time-dependence, the intra-cavity dynamic is characterized by a combination of Eq. (2.85) and Eq. (2.24). The intra-cavity fields can be reconstructed using the leading order solution Eq. (2.18), with $A, B, \sigma, \sigma_0, \xi$ and x_0 propagating accordingly. To accommodate time-dependence in difference scales, Eq. (2.85) is modified and the governing equations are given:

$$\frac{dB}{dt} = \epsilon\left(\frac{\langle \Re(e^{-i\psi}G), dnz\rangle + F\cos(\sigma-\sigma_0)p_1(\xi)}{\sqrt{|\beta|}(q_1(k)-k^2q_2(k))} - \frac{\sqrt{|\beta|}B\langle dnz, dnz\rangle}{\sqrt{|\beta|}(q_1(k)-k^2q_2(k))}\right), \tag{2.99a}$$

$$\frac{dx_0}{dt} = -\beta\xi + \epsilon\frac{\langle \Re(e^{-i\psi}G), \phi(z)\rangle - F\sin(\sigma-\sigma_0)p_2(\xi)}{\sqrt{|\beta|}B^2k^2q_3(k)}, \tag{2.99b}$$

$$\frac{d\xi}{dt} = \epsilon\frac{\langle \Im(e^{-i\psi}G), snzcnz\rangle - F\cos(\sigma-\sigma_0)p_3(\xi)}{\sqrt{|\beta|}q_2(k)}, \tag{2.99c}$$

$$\frac{d\sigma_0}{dt} + \xi\frac{dx_0}{dt} = \epsilon\frac{F\sin(\sigma-\sigma_0)p_4(\xi) - \langle \Im(e^{-i\psi}G), \varphi(z)\rangle}{\sqrt{|\beta|}Bq_4(k)}, \tag{2.99d}$$

$$\frac{d\sigma}{dt} = -\alpha - \frac{\beta}{2}B^2(2-k^2) - \frac{\beta}{2}\xi^2. \tag{2.99e}$$

In the case of $\epsilon \ll 1$, we set $\epsilon = 0.1$ in our simulations. With a clean pump, we observe a stable soliton in time and clean comblines in the spectrum of the intra-cavity field, as shown in Fig. 2.14.

When the forcing term is corrupted by a Gaussian shaped noise as defined, numerical simulations of the LLE confirm the existence of noises around each comb line in the intra-cavity field spectrum, as shown in Fig. 2.15. Furthermore, we find both amplitude and width of the output noises are determined by the input Gaussian noises.

With LLE perturbation theory, we embed the full intra-cavity dynamics into the coupled ordinary differential equations Eq. (2.99), which model the time-dependence of the five parameters (B, x_0, ξ, σ_0 and σ) in the leading order solution of Eq. (2.13). We demonstrate

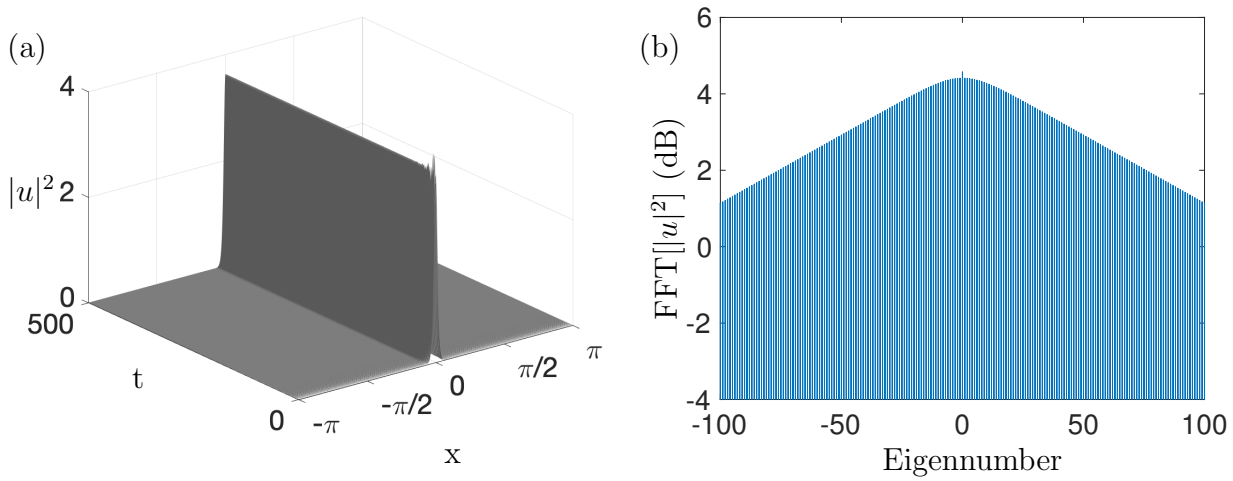

Figure 2.14: Numerical simulation of Eq.(2.13) with a clean pump ($\epsilon = 0.1$) in (a) time domain and (b) spectrum domain.

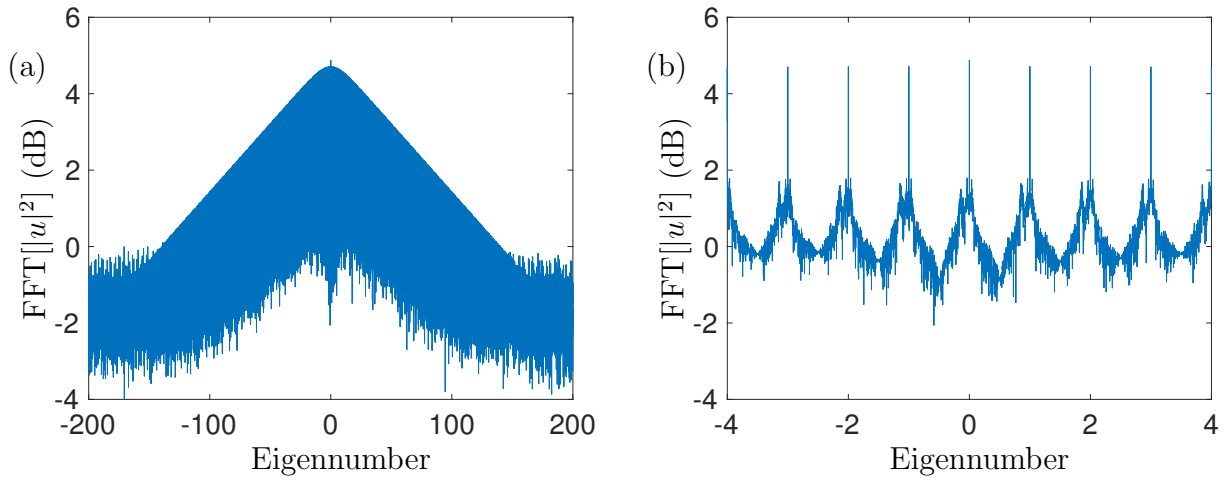

Figure 2.15: (a) Numerical simulation of Eq.(2.13) ($\epsilon = 0.1$) with a pump corrupted by Gaussian shaped noises (amplitude=1, width=0.05). (b) When zoomed in, we observe Gaussian shaped noises around each comb line in the intra-cavity field spectrum.

that this significantly reduced model can correctly recover the intra-cavity dynamics with Gaussian shaped noises in the pump, thus serves as an efficient tool for characterizing the intra-cavity dynamics.

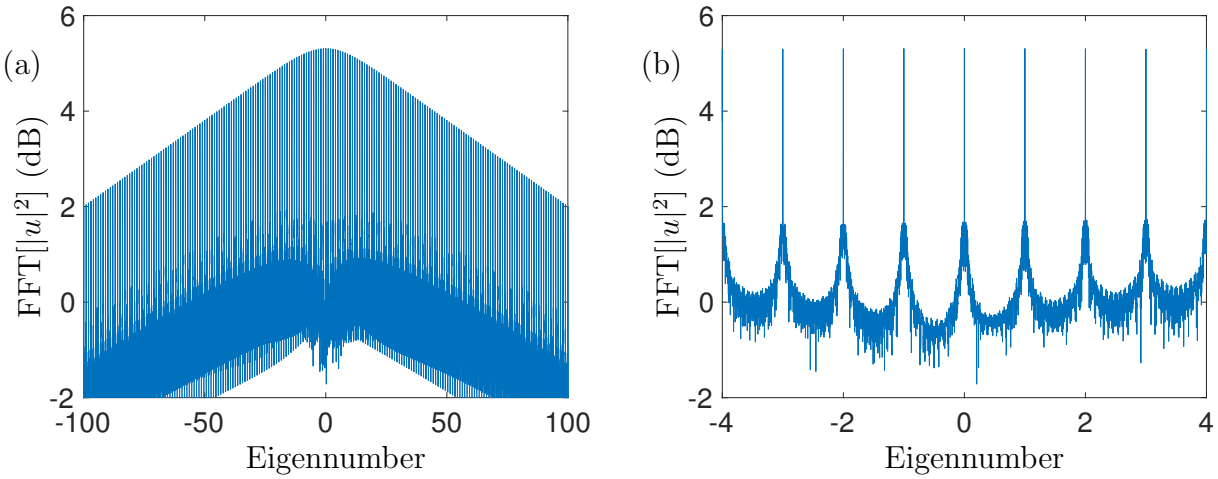

Figure 2.16: (a) Spectrum of the reconstructed intra-cavity field with pump corrupted by Gaussian shaped noises (amplitude=1, width=0.05, $\epsilon = 0.1$). (b) We observe Gaussian shaped noises around each comb line in the intra-cavity field spectrum when zoomed in. This spectrum given by the reduced model matches with the simulation of Eq.(2.13), showing that our LLE perturbation theory correctly characterizes the intra-cavity dynamics with a significantly reduced model.

When input pumps are corrupted by weak noises, the reduced model provided by LLE perturbation theory correctly captures the Gaussian shaped noises around each comb line in the intra-cavity field spectrum, as shown in Fig. 2.16. Compared to the simulation of Eq. (2.13), noises around each comb line in Fig. 2.16 is narrowed and slightly decreased in amplitude when same noises are added to the enforcing pump. This is expected as the reduced model neglects not only the modes at higher orders, but also their energies. Regardless, the reduced model captures the majority of the noise energy, and successfully characterizes the noises in the intra-cavity fields when the input noises change. Note that the reduced model fails to restore the overall noise level in the spectrum, as compared in Fig. 2.15 (a) and Fig. 2.16 (a), confirming that LLE perturbation theory only specializes in characterizing the local

intra-cavity dynamics.

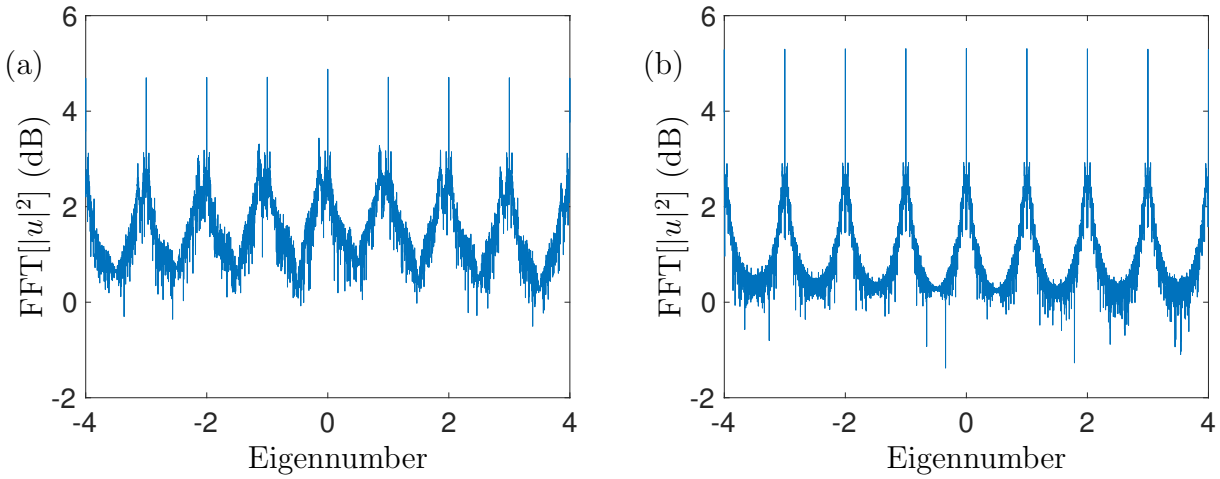

Figure 2.17: (a) Numerical simulation of Eq.(2.13) ($\epsilon = 0.1$) with a pump corrupted by Gaussian shaped noises (amplitude=50, width=0.05). (b) We observe similar Gaussian shaped noises around each comb line in the intra-cavity field spectrum when reconstructed with LLE perturbation theory.

When the enforcing pump is corrupted by a stronger noise, similarities are spotted as the noises around each comb line are narrowed and slightly decreased in amplitude, as shown in Fig. 2.17. Furthermore, simulations show LLE perturbation theory holds well in the large limit of ϵ. As shown in Fig. 2.18, the limit of $\epsilon = 1$ is taken to recover the regular LLE in our scaling. Notice that as ϵ is increased, the intra-cavity field deforms from the leading order solution *dn* and forms to sit atop a shelf [134]. In the spectrum, this is characterized by the increased strength of the central frequency and its surrounding plateau. This shelf, however, is the second order correction in the LLE perturbation theory, and is excluded from the leading order reconstruction in the following simulations. Similarly when the input pumps are corrupted by weak noises, LLE perturbation theory correctly captures the output noises in the intra-cavity field spectrum, as shown in Fig. 2.19. As expected, LLE perturbation theory fails to capture the enhanced central frequency in the spectrum, but it successfully recovers the Gaussian shaped noises around each comb line, albeit in a slightly narrowed and

weakened form.

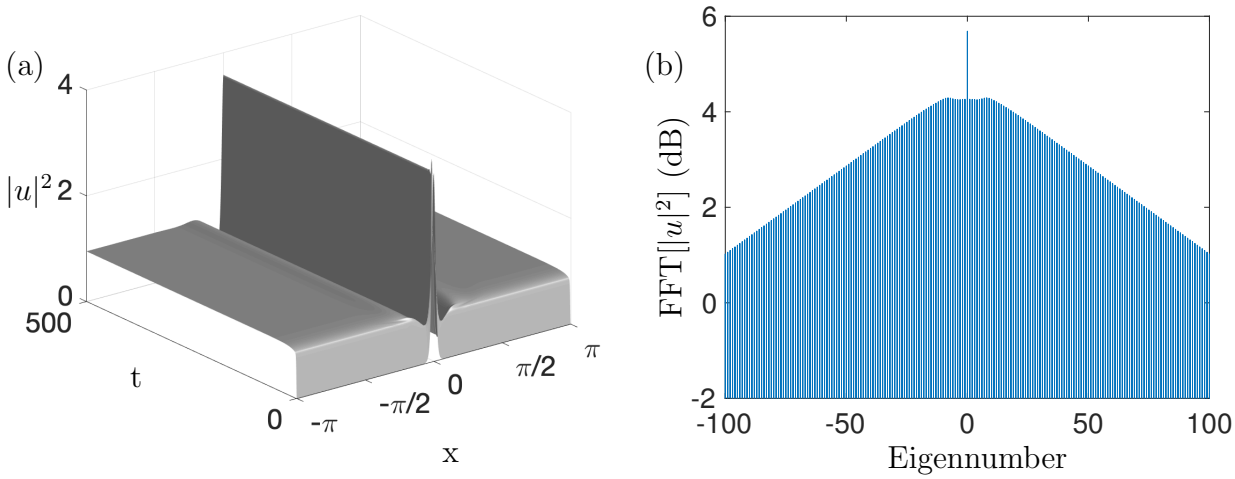

Figure 2.18: Numerical simulation of Eq.(2.13) with a clean pump ($\epsilon = 1$) in (a) time domain and (b) spectrum domain.

When the enforcing pump is corrupted by strengthened noises, simulations of Eq. (2.13) show increased number of localized pulses per round trip, as shown in Fig. 2.20. Consequently LLE perturbation theory fails to recover the intra-cavity dynamics with a fixed number of localized pulses in the leading order approximation.

In the form of Jacobi elliptic function *dn*, LLE perturbation theory provides a reduced model to characterize the intra-cavity dynamics with only five parameters. This significantly reduced model not only captures the noises in the spectrum of the intra-cavity fields, but serves as an efficient tool to quantify the impacts of the input noises on the intra-cavity fields. Fig. 2.21 describes how the amplitude of the output noise changes when the input Gaussian shaped noises change in both amplitude and width. As expected, the amplitude of output noise is increased when the input noise is stronger in amplitude, as shown in Fig. 2.21 (a). More interestingly, Fig. 2.21 (b) shows that the width of the input noise contributes to the amplitude variation of output noises as well. Nevertheless, the amplitude or width changes of the input noise barely have impacts on the width of the output noises, and we only

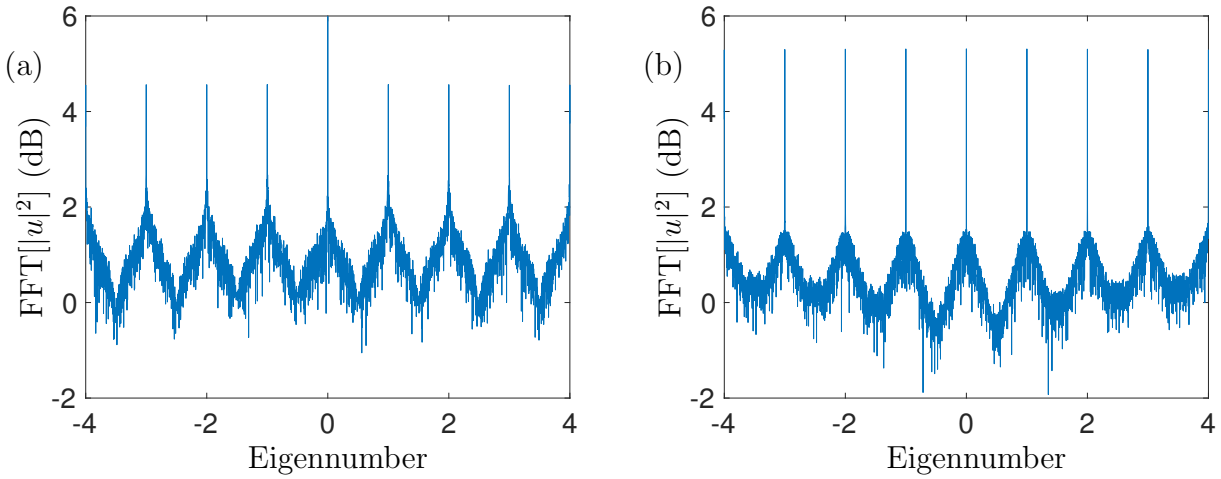

Figure 2.19: (a) Numerical simulation of Eq.(2.13) ($\epsilon = 1$) with a pump corrupted by Gaussian shaped noises (amplitude=1, width=0.05). (b) We observe similar Gaussian shaped noises around each comb line in the intra-cavity field spectrum when reconstructed with LLE perturbation theory.

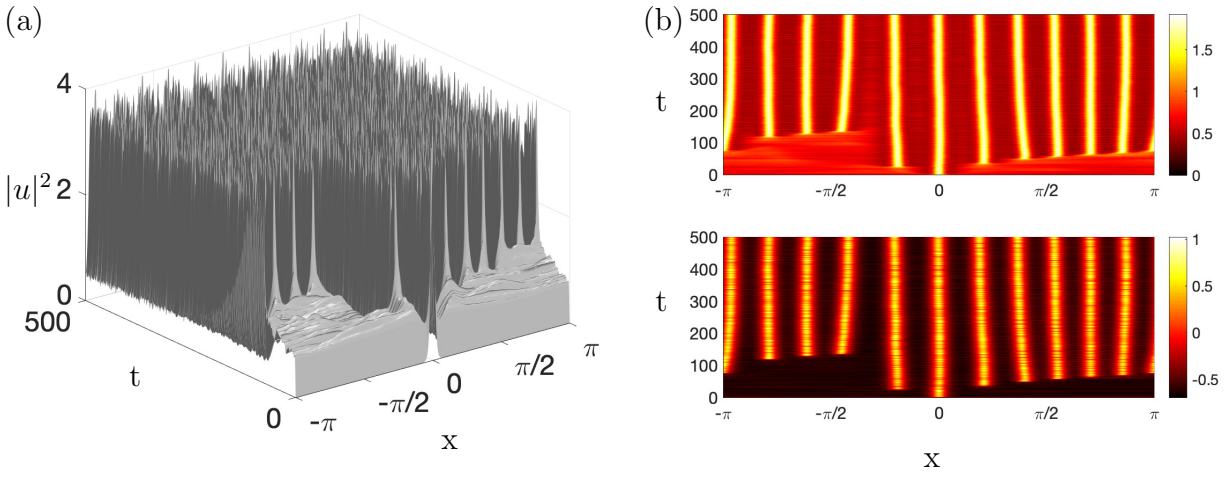

Figure 2.20: (a) Numerical simulation of Eq.(2.13) ($\epsilon = 1$) with a pump corrupted by Gaussian shaped noises (amplitude=50, width=0.05). (b) Top view of the simulation shows that the number of localized pulses per round trip increases with a stronger noise in the enforcing pump.

observe random fluctuations in the width of the output noises, as shown in Fig. 2.22. Notice that simulations are repeated for six times at each point, with both average and standard deviation shown in Fig. 2.21 and Fig. 2.22.

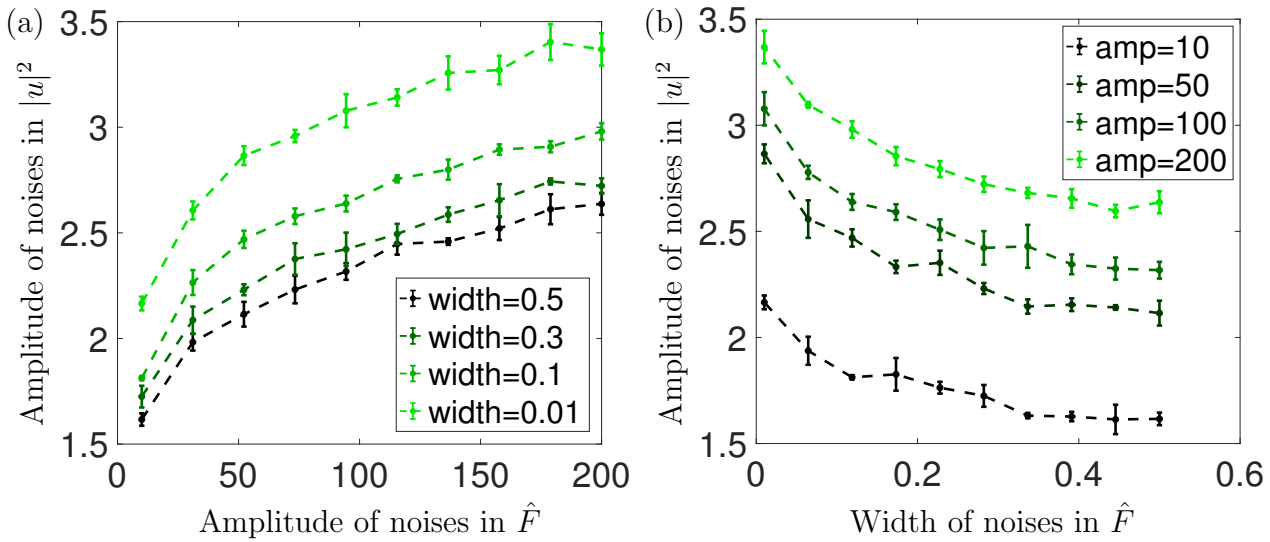

Figure 2.21: Dependence of the amplitude of noises in intra-cavity field spectrums on (a) amplitude and (b) width of the input noises. The amplitude of output noises increases with stronger and broader Gaussian shaped noises in the enforcing pumps.

2.6 Conclusion

In this chapter, we have shown that the LLE equation supports stable solutions of the Jacobi elliptic type. These solutions model periodic pulse trains of soliton-like solutions for which the pumping F is critical for stabilization. Our rigorous stability analysis also results in a perturbation theory for characterizing the effects of higher-order terms in the microresonator, such as may arise from Raman scattering, higher-order dispersion, spontaneous emission noise and enforcing pump noise. The historical success of soliton perturbation theory in describing, for instance, Gordon-Haus timing jitter and/or the soliton self-frequency shifts, was critical in characterizing lightwave transmission systems and mode-locked lasers. Similarly, the LLE perturbation theory presented here can be a critically enabling tool for characterizing a host

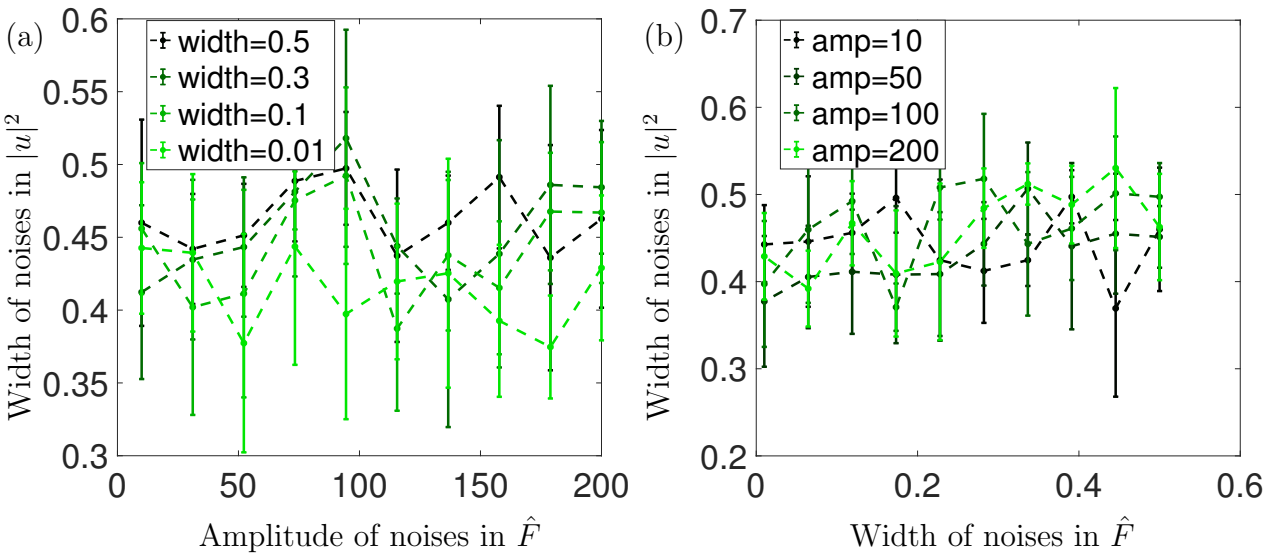

Figure 2.22: Dependence of the width of noises in intra-cavity field spectrums on (a) amplitude and (b) width of the input noises. The width of output noises is barely impacted by the amplitude or width of the Gaussian shaped noises in the enforcing pumps.

of additional microresonator phenomenon and potentially engineering new resonator designs with improved performance metrics.

Our stability analysis helps confirm several experimental observations. Most notably, it supports the recent observations that soliton states in the microresonator are not detuning degenerate, and can be individually addressed by laser detuning. Indeed, the theory rigorously confirms that the detuning can be used to lock the microresonator to any target multiple-pulse state, where the stability of each multiple-pulse state is explicitly computed and its minimum detuning assessed. The theory additionally shows that the phase-locking of the *dn* comb solution is an attractor to the resonator. Moreover, only solutions with no nodal separation (a zero separating pulses) are stabilized. Finally, the application of our theory to Raman scattering and stimulated emission perturbations show that neither effects destabilizes the comb. Rather, they both generate a drift in the pulse train, one which is deterministic in nature (Raman) and one which produces a random walk (noise).

Chapter 3

FREQUENCY COMB GENERATION AT 800NM IN WAVEGUIDE ARRAY QUANTUM WELL DIODE LASERS

In this chapter[1], we present a quantum well based traveling wave model for a semiconductor diode laser, and demonstrate a comprehensive theoretical model of the laser systems with intensity discrimination and controllable loss based on mode-coupling in a waveguide array. Specifically, we characterize the temporal shaping effects of the nonlinear mode-coupling induced by the waveguide arrays with a model developed for the detailed semiconductor gain dynamics. The waveguide array provides an enhanced pulse shaping and loss to generate stable frequency combs at a wavelength of 800 nm in a GaAs device. Within this parameter regime, a single waveguide is not capable of achieving stable and broad comb generation, whereas stable waveform could be generated and optimized by a waveguide array designed with appropriate parameters. Extensive numerical simulations show that the quantum well depth, the linear waveguide coupling coefficient, and the input currents to the first and second waveguides are significantly important to design an effective waveguide array for producing a compact, efficient and robust on-chip comb source in GaAs.

3.1 Introduction

Optical frequency comb generation on chip scale devices are critical for practical engineering design and commercial applications ranging from frequency metrology and optical spectroscopy [33, 143], multi-heterodyne spectroscopy [29], optical atomic clocks [38], and arbitrary waveform synthesis [32]. However, reduction to chip scale diode lasers remains an important technological challenge due to practical physics considerations such as the non-

[1]Content of this chapter is published in journal article [135].

linear phase shifts that occur from the fast carrier dynamics [35], and limit the pulse width within the cavity. A recent work [42] has theoretically developed a quantum wells based traveling wave model for a semiconductor diode laser in detail. This work leveraged well known results that single-section diode lasers without saturable absorbers can also generate frequency-modulated (FM) mode locking [141]. Numerical simulations demonstrated the generation of frequency modulated comb and provided potential for a compact, chip-scale comb source without additional external components at wavelength of 1550 nm. However, the generation of a broad, stable comb was difficult at the modified parameter settings of 800 nm where many engineering applications are relevant. In this chapter, we modify the detailed physics model introduced in the recent work [42] and include coupled waveguide arrays (WGAs) for the generation of stable frequency combs at 800nm. Considering WGAs have been demonstrated to enhance the necessary nonlinear pulse shaping effects for mode-locking generation [152], they are introduced in our model to promote stable waveform generation at 800nm. Indeed, we demonstrate the generation of stable waveforms in a diode laser configuration with the addition of the WGAs, providing the possibility of chip scale frequency comb generation at 800nm.

Optical frequency comb generation can be accomplished in a diverse number of laser settings. For instance, they can be generated in now standard mode-locked lasers such as Ti:Sapphire [138] and fiber lasers [46]. Generation in passive microresonators due to Kerr nonlinearity is also reported [61] as well as others based on microcavities, gain-switching lasers and phase modulators [142, 111, 10]. These standard and successful methods require a number of optical and fiber components that must be carefully aligned. They further often require bulky pump lasers and amplifiers for operation. So although they are ideally suited for laboratory experiments, they are difficult to implement outside of such laboratory settings. Diode lasers, in contract, provide direct frequency comb generation, are portable and efficient from a chip-scale device and have been reduced to practice in numerous technologies [108, 119]. Two competing dynamics are at work in a typical laser of this type: a gain dynamic and a reverse-biased saturable absorber dynamic. A periodic train of short pulses is formed as a

consequence of competition between these two effects, and its Fourier transform results in an optical frequency comb generation. It turns out that the stabilization of such pulses is limited by the nonlinear phase shifts that occur due to fast carrier dynamics [35]. However, as noted earlier, the FM mode-locked state in a single-section diode laser results in a continuous wave in time but a fixed, non-zero phase difference between comb lines because of the frequency modulation.

Quantum dot (QD) [50, 118] and quantum lasers (QDash) [120] have been an ideal source for studying FM mode-locking operation, with quantum well (QW) [122, 20] and bulk semiconductor lasers [141] also exhibiting this phenomenon. Given their practical importance, computational and theoretical models of semiconductor quantum well lasers have been extensively developed. Models can be fairly simple, including only a single rate equation and photon density variable [63, 2]. More complex models include multiple rate equations and material polarization [6, 76, 101, 69, 145, 53, 92, 68, 131] with various phenomenological parameters inserted. Existing models have failed to explain consistently the origin of the FM comb generation. This is, in part, due to the diverse and numerous nonlinear effects in the laser cavity. Following on previous QD single-section laser models [25, 50], Dong et al [42] developed a more comprehensive detailed model for the QW diode laser dynamics. At 1550 nm, this model was able to produce stable waveforms and excellent performance characteristics. But in the application important 800 nm parameter regime, the model did not produce broad, stable combs.

The difficulty of generating combs at the shorter wavelength has been ascribed to the absence of spatial hole burning on the scale of a half-wavelength owing to carrier diffusion [41]. In the absence of the "fast" spatial holes due to standing waves, the "slow" spatial holes on the length scale of the cavity length yield multiple longitudinal modes that exchange energy in a periodic or chaotic manner, resulting in an unstable spectrum [124]. The difficulty in producing FM combs in such a detailed QW diode laser model at 800 nm motivates our exploration of using WGAs to enhance nonlinear pulse shaping for mode-locking and stabilize wave generation. Mode-coupling in WGAs has been shown to produce the inten-

sity discrimination necessary to produce mode-locking [114, 89, 22]. Indeed, semiconductor WGAs studied for CW lasing [117, 116] motivated a recent phenomenological model for mode-locking on a chip [152]. Here, we integrate the detailed semiconductor physics model of Dong et al. [42] into a WGA in order to achieve stable waveform generation at 800 nm. Indeed, we show that the extra pulse shaping and controllable loss induced by the WGAs is capable of producing frequency combs in this important parameter regime.

As for the integrated device structure, a dispersion-compensating fiber is not necessary. Specifically, an OFC generator does not have to produce a train of short pulses. The integrated device described here operates in a frequency-modulated (FM) mode and produces coherent comb lines that have a deterministic quadratic phase relationship. A dispersion-compensating fiber is used here only to demonstrate the coherent nature of the comb. It is not required for any applications of frequency combs.

The chapter is outlined as follows: Sec. 3.2 details the theoretical model constructed for characterizing the electric field evolution dynamics and complex semiconductor gain physics. Section 3.3 shows detailed simulations of the full model and the resulting wave form generation, followed by Sec. 3.4 which briefly summarizes our results.

3.2 Theoretical models

In the following subsections we present the key modeling components in details to characterize the laser cavity dynamics, of which the interplay results in the generation of stable waveforms at 800nm.

3.2.1 Waveguide Arrays

A quantum well based traveling wave model of a semiconductor diode laser for the generation of stable frequency combs at 1550nm has been well studied [42]. The model was introduced in a single waveguide built with InGaAs. Here we extend this model to the GaAs device, which has a higher central transition energy and typically operates at around 800 nm. However, numerical simulations show no generation of stable waveforms in this new

parameter regime with the single waveguide model. We generalize the model by including WGAs considering their effects in pulse shaping by introducing the intensity discrimination, to help promote stable waveform generation at the desired parameter regime. The schematic of a waveguide array mode-locked laser is shown in Figure 3.1. With the low-intensity light coupled out to the neighboring waveguides, the electric field propagating in the first waveguide is shaped according to the interplay of intensity, dispersion and gain dynamics. This intensity discrimination introduced by WGAs is necessary for stable waveform generation in a mode-locked laser cavity [114, 89, 22]. Moreover, the coupled waveguides in WGAs provide a controllable loss mechanism to filter out very high order longitudinal modes and tailor the output spectrum into an improved form.

The leading-order equations governing the electric field dynamics and the linear, evanescent electric field coupling to the neighboring waveguides are given by

$$i\frac{dE_n}{dx} + C(E_{n-1} + E_{n+1}) + \beta|E_n|^2 E_n = 0, \tag{3.1}$$

where E_n represents the electric field envelope in the nth waveguide in the array, C represents the linear coupling coefficient, x represents the normalized distance in the waveguide array and β the nonlinear self-phase modulation parameter [26, 112, 5].

Though the waveguide array can be formed with different numbers of waveguides, numerical studies and stability analysis show that robust pulse shaping and intensity discrimination can be produced with three or more waveguides [5]. Furthermore, early WGA experiments [112] show that a three waveguide structure has almost identical properties to the 41 waveguides. Consequently, we consider a WGA architecture with three waveguides here. More specifically, in the waveguide array, the first waveguide is designed as forward biased and gets a net gain from the pump. The second waveguide is close to transparency with zero net gain. Waveguide three is engineered to attenuate the electromagnetic energy that enters it. Specifically, it is reversely biased and sweeps out optically generated carriers to increase the linear loss and shorten the recovery lifetime. It should be noted that there are many other mechanisms that can produce saturable absorption in a laser cavity, with a diverse set

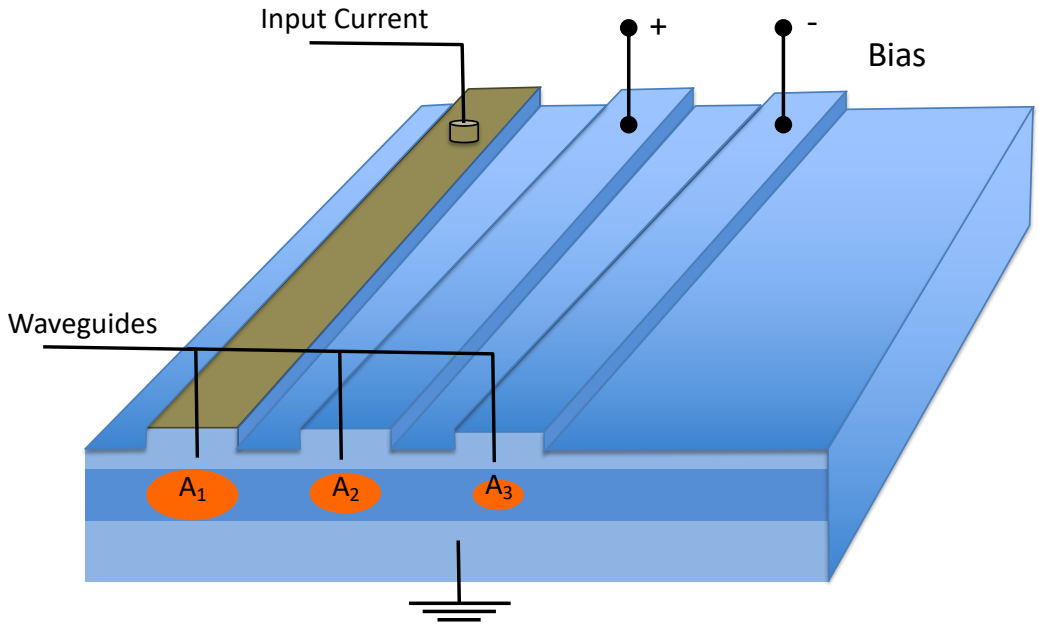

Figure 3.1: Schematic of a waveguide array diode laser. The input current on the first waveguide provides with the saturable absorption and amplification while the following waveguides two and three are for intensity discrimination and pulse shaping. Only waveguide one has net gain, the following waveguides two and three experience net losses.

of quantitative and qualitative models for characterizing its physical effects [85]. Here, we have chosen a quantitative model that can be engineered within the laser chip structure, i.e. we forego as much as possible any empirical or generic models.

3.2.2 Gain model and governing equations

Here we briefly describe the non-trivial gain model [42], and extend it to the three waveguide array structure. Relaxation of the electrons from N-side to the separate confinement heterostructure (SCH) layer traps carriers inside the quantum well, as shown in Figure 3.2. In addition to the discretization and propagation of the wave equations, the carrier equations in the energy space are discretized as well in the gain model [42]. Despite the increased calculation expenses of the carrier equations, this model successfully captures the detailed cavity dynamics [42].

For the carriers trapped in the quantum well, light emitted is centered around different central frequencies because of the varied transverse energy E_t. As opposed to the confined x direction, carriers in the quantum well have transverse momenta in the unconfined directions of y and z. Specifically, the transverse energy E_t is derived from the joint density of states as an integrated combination of carrier transverse energies, and contributes to light generation and recombination. Experimentally by changing the depth of the quantum well, we can constrain the carrier energy otherwise the carriers would easily escape. That is, the maximum transverse energy $\max(E_t)$ can be equivalently adjusted by varying the quantum well depth. In this non-trivial gain model, all carrier Lorentzians are integrated in energy space [42].

The electric field, including forward and backward propagation is given by

$$E(x,t) = E_+(x,t)e^{ik_0x} + E_-(x,t)e^{-ik_0x}. \tag{3.2}$$

Deriving from the slowly-varying envelope equation of $E_\pm(x,t)$, combined with semiconductor Bloch equations of the total material polarization, and the carrier grating effects, the

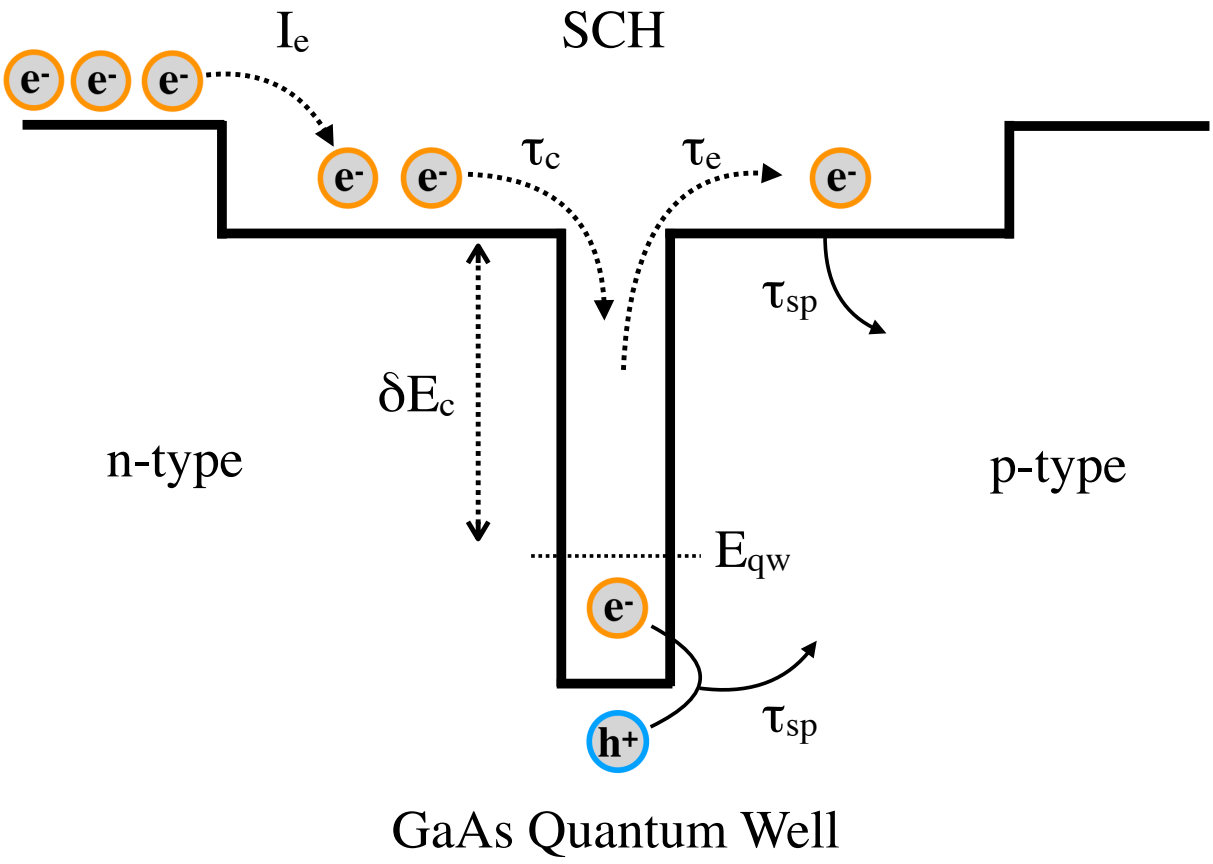

Figure 3.2: Schematic of a quantum well laser diode. Electrons can be trapped into the quantum well from the input current injection, and they have a probability of escaping from the quantum well as well.

model [42] obtains

$$\pm\frac{\partial E_\pm}{\partial x}+\frac{1}{v_g}\frac{\partial E_\pm}{\partial t}+i\frac{k''}{2}\frac{\partial^2 E_\pm}{\partial t^2}=-\frac{\alpha}{2}E_\pm-\left(\frac{\alpha_S}{2}+i\beta_S\right)(|E_\pm|^2+2|E_\mp|^2)E_\pm+S_{sp}$$
$$+n_{qw}\frac{g_0}{2}\int\frac{dE_t}{\hbar\omega_0}(\rho^e_{qw,E_t}+\rho^h_{qw,E_t}-1)F_\pm(E_t,x,t) \tag{3.3}$$
$$+n_{qw}g_0\int\frac{dE_t}{\hbar\omega_0}\rho^{(*)}_{g,E_t}F_\mp(E_t,x,t)$$

where k'' is the dispersion coefficient, α is the linear waveguide loss, α_S the two-photon absorption and β_S the Kerr nonlinear coefficients. Electron (e) or hole (h) occupation probabilities are notated as $\rho^{e,h}$. $\rho^{(*)}_{g,E_t}$ is the grating term and S_{sp} and $F_\pm(E_t,x,t)$ are respectively the spontaneous emission term and the filtered field derived in ref. [42].

The coupled carrier rate equations are given [42]

$$\frac{\partial\rho^{e,h}_{sch}}{\partial t}=\frac{\eta J_{in}}{qN_{c,v,sch}h_{sch}}(1-\rho^{e,h}_{sch})-\frac{\rho^{e,h}_{sch}}{\tau_{sp}}+n_{qw}\sum_{E_t}\left[\rho^{e,h}_{qw,E_t}\frac{(1-\rho^{e,h}_{sch})}{\tau^{e,h}_e}-\rho^{e,h}_{sch}\frac{(1-\rho^{e,h}_{qw,E_t})}{\tau^{e,h}_c}\right], \tag{3.4a}$$

$$\frac{\partial\rho^{e,h}_{qw,E_t}}{\partial t}=\frac{h_{sch}N_{c,v,sch}}{n_{qw}h_{qw}N_{r,qw}}\left(\rho^{e,h}_{sch}\frac{(1-\rho^{e,h}_{qw,E_t})}{\tau^{e,h}_c}-\rho^{e,h}_{qw,E_t}\frac{(1-\rho^{e,h}_{sch})}{\tau^{e,h}_e}\right)-\frac{\rho^{e,h}_{qw,E_t}}{\tau_{sp}}-R_{st}-R_g, \tag{3.4b}$$

$$\frac{\partial\rho_{g,E_t}}{\partial t}=-\frac{\rho_{g,E_t}}{\tau_{sp}}-4k_0^2D\rho_{g,E_t}-2g_0\frac{\Delta E_t}{(\hbar\omega_0)^2h_{qw}WN_{r,qw}}$$
$$\times\left[\frac{1}{2}(E^*_+F_-+F^*_+E_-)(\rho^e_{qw}+\rho^h_{qw}-1)+2\mathrm{Re}(E^*_+F_++E^*_-F_-)\rho_{g,E_t}\right], \tag{3.4c}$$

where R_{st} and R_g are the recombination rates of population decay for stimulated emission and carrier grating, $N_{c,v,sch}$ and N_r are the effective 3-D and 2-D density of states. The parameter g_0 is the gain coefficient defined as

$$g_0=\frac{\Gamma_{yz}n_{qw}q^2m_r|\hat{\mathbf{e}}\cdot\mathbf{p}|^2}{12\pi\hbar c\epsilon_0m_0n_0\Gamma h_{qw}}, \tag{3.5}$$

where $m_r=1/(1/m_{e,qw}+1/m_{h,qw})$ is the reduced effective mass. Other parameters are listed in Table 3.1 in details.

For simplicity, we rewrite the complicated gain term as a function of $G_{\pm}(E_{\pm})$ so that Eq. (3.3) is more compactly represented

$$\pm\frac{\partial E_{\pm}}{\partial x}+\frac{1}{v_g}\frac{\partial E_{\pm}}{\partial t}+i\frac{k''}{2}\frac{\partial^2 E_{\pm}}{\partial t^2}=-\frac{\alpha}{2}E_{\pm}-\left(\frac{\alpha_S}{2}+i\beta_S\right)(|E_{\pm}|^2+2|E_{\mp}|^2)E_{\pm}+S_{sp}+G_{\pm}(E_{\pm}). \tag{3.6}$$

These field equations are coupled with the carrier rate equations for the SCH and QW sections, of which the complete forms are shown in Dong et al. [42].

We extend this gain model to the waveguide array structure with three waveguides. By coupling out low-intensity components of the electric field to the neighboring waveguides, we can effectively shape the electric field propagating in the first waveguide through controllable loss and intensity discrimination, thus achieving highly robust stable waveform generation in the laser cavity.

The resulting equations describing the approximate dynamics of waveguide array mode-locking are thus given by

$$\begin{aligned}&\pm\frac{\partial E^1_{\pm}}{\partial x}+\frac{1}{v_g}\frac{\partial E^1_{\pm}}{\partial t}+i\frac{k''}{2}\frac{\partial^2 E^1_{\pm}}{\partial t^2}\\&\qquad=-\frac{\alpha}{2}E^1_{\pm}-\left(\frac{\alpha_S}{2}+i\beta_S\right)(|E^1_{\pm}|^2+2|E^1_{\mp}|^2)E^1_{\pm}+S_{sp}+G^1_{\pm}+iCE^2_{\pm},\end{aligned} \tag{3.7}$$

$$\begin{aligned}&\pm\frac{\partial E^2_{\pm}}{\partial x}+\frac{1}{v_g}\frac{\partial E^2_{\pm}}{\partial t}+i\frac{k''}{2}\frac{\partial^2 E^2_{\pm}}{\partial t^2}\\&\qquad=-\frac{\alpha}{2}E^2_{\pm}-\left(\frac{\alpha_S}{2}+i\beta_S\right)(|E^2_{\pm}|^2+2|E^2_{\mp}|^2)E^2_{\pm}+S_{sp}+G^2_{\pm}+iC(E^1_{\pm}+E^3_{\pm}),\end{aligned} \tag{3.8}$$

$$\begin{aligned}&\pm\frac{\partial E^3_{\pm}}{\partial x}+\frac{1}{v_g}\frac{\partial E^3_{\pm}}{\partial t}+i\frac{k''}{2}\frac{\partial^2 E^3_{\pm}}{\partial t^2}\\&\qquad=-\frac{\alpha}{2}E^3_{\pm}-\left(\frac{\alpha_S}{2}+i\beta_S\right)(|E^3_{\pm}|^2+2|E^3_{\mp}|^2)E^3_{\pm}+S_{sp}+G^3_{\pm}+iCE^2_{\pm}.\end{aligned} \tag{3.9}$$

For simplicity, the dimensionless coupling factor C is maintained the same in our simulation between different waveguides. C is determined by the designed parameters of the WGA, such as the waveguide separation along with its width and depth [150]. Specifically, with

the linear coupling coefficient c (m^{-1}) and waveguide length L (m), $C = cL$. Thus it can be adjusted via designing the waveguide array to realize optimal mode-locking of the output.

The carrier rate equations are also modified to simulate the weakly forward biased state and reverse biased state in the second and third waveguides. We simply set $J_{in} = 0$ in the rate equations for the second waveguide to get zero net gain. For the third waveguide, we simulate the voltage driven bias with an equivalent carrier drift with lifetime $\tau_d^{e,h}$ and replace the gain term as

$$\frac{\partial \rho_{sch}^{e,h}}{\partial t} = n_{qw} \sum_{E_t} \left[\rho_{qw,E_t}^{e,h} \frac{(1 - \rho_{sch}^{e,h})}{\tau_e^{e,h}} - \rho_{sch}^{e,h} \frac{(1 - \rho_{qw,E_t}^{e,h})}{\tau_c^{e,h}} \right] - \frac{\rho_{sch}^{e,h}}{\tau_d^{e,h}} - \frac{\rho_{sch}^{e,h}}{\tau_{sp}}. \tag{3.10}$$

3.3 Numerical Results for Stable Waveform generation

We solve the forward and backward wave equations (Eqs. (3.7)-(3.9)), coupled with the carrier rate equations [42] numerically using a robust predictor-corrector scheme which generically improves stability properties compared to the Euler algorithm [137]. We simulate 100 ns of operation of the waveguide array starting from noise with a time step of $\Delta t = 30$ fs. Our full model takes approximately 4 hours to run parallelized on x2 6-Core Intel Xeon CPU. The full simulation parameters are listed in Table 3.1. Note that the major difference between GaAs and the previous material considered, InGaAsP, is that GaAs has a larger central transition frequency $E_0 = \hbar\omega_0$ and diffusion coefficient D while the two-photon absorption α_s is significantly decreased. These changes of parameters affect the formation of stable combs in the single waveguide model. Given the large parameter space to be explored using WGAs for optimal design, we focus on (i) the linear waveguide coupling coefficient C between the three waveguides, (ii) the input pump to the waveguide array, and (iii) the depth of the quantum well. The third waveguide is set to be reversed biased and maintains the same setup in the following experiments, while the first two waveguides have varied input pumps in different experiments. The other parameters are chosen to be the feasible parameters for an experimental design [42].

Similar to the single waveguide model, we specify the limits of E_t, that is, $\max(E_t)$, and

Table 3.1: **Simulation parameters for the GaAs system.**

Symbol	Description	Value
L	Length of device	500 μm
W	Width of waveguide	4 μm
h_{sch}	Height of SCH layer	50 nm
h_{qw}	Height of quantum well	5 nm
n_0	Group refractive index	3.5
n_{qw}	Number of quantum wells	2
α	Intrinsic waveguide loss	5 cm^{-1}
Γ_{yz}	Optical confinement factor	0.02
α_S	Two-photon absorption	580 W^{-1}m^{-1}
β_S	Kerr coefficient	430 W^{-1}m^{-1}
$\hbar\omega_0$	Central transition energy	1.55 eV
$\lvert\hat{\mathbf{e}} \cdot \mathbf{p}\rvert^2$	Momentum matrix element	25 meV$\times m_0/6$
Γ	Homogenous half linewidth	11 meV/$\hbar$
$m^*_{e,sch}$	Effective electron mass in SCH layer	0.125 m_0
$m^*_{h,sch}$	Effective mass of holes in SCH layer	0.703 m_0
$m^*_{e,qw}$	Effective electron mass in GaAs QW	0.093 m_0
$m^*_{h,qw}$	Effective mass of holes in GaAs QW	0.53 m_0
$\tau_c^{e,h,qw}$	Electron, hole capture time	1, 10 ps
$\tau_d^{e,h}$	Electron, hole drift time	0.1, 0.3 ps
δE_c	Conduction band quantum well barrier	50 meV
δE_v	Valence band quantum well barrier	25 meV
β_{sp}	Spontaneous emission coupling factor	1×10^{-4}
τ_{sp}	Spontaneous emission lifetime	1 ns
D	Ambipolar diffusion coefficient	20 cm$^2 s^{-1}$

the number of energy bins. As discussed previously, max(E_t) can be adjusted by varying the quantum well depth, and thus is experimentally controllable with appropriate fabrication design. The size of the energy bin (dE_t) is the energy discretization for numerical computation. It is chosen to be small relative to the homogeneous linewidth for numerical convergence of the gain integral. Smaller size of energy bins will greatly increase computation time. Note that our simulations also suggested that higher energy carriers can contribute to the total gain and thus affect the generation of the lasing dynamics. We choose max(E_t) = 50 meV, with 25 energy bins to guarantee a small energy step for an accurate gain integral.

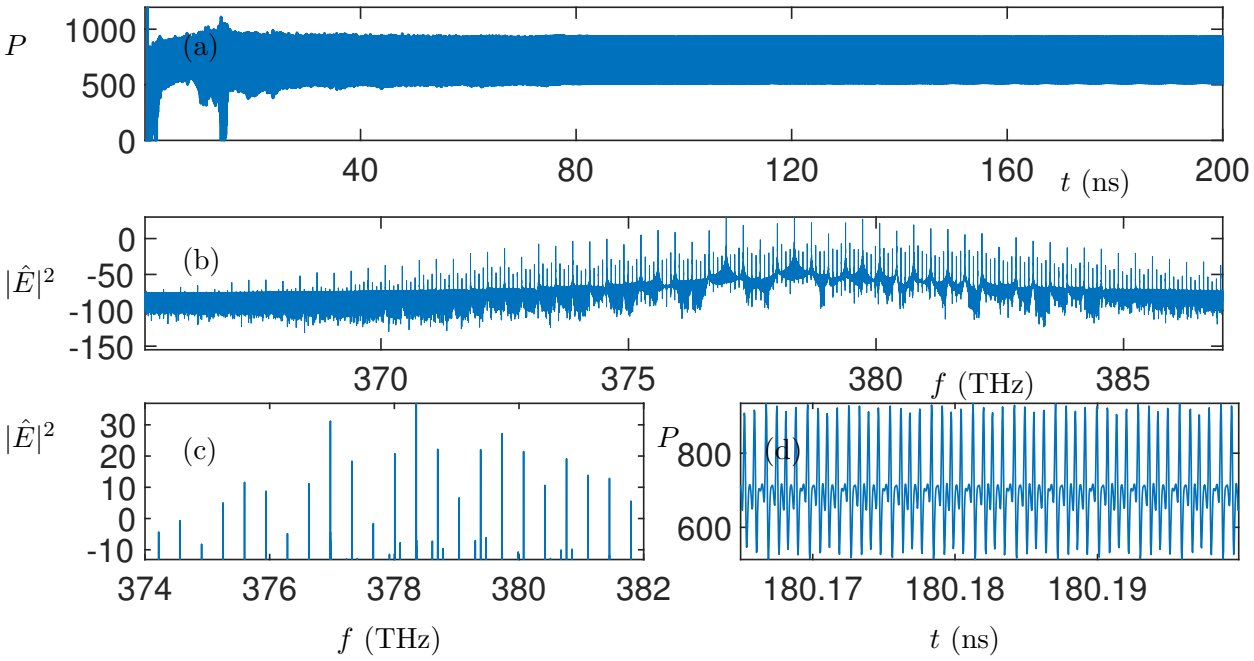

Figure 3.3: Evolution of output power P (mW) and power spectral density $|\hat{E}|^2$ (dBm/Hz) in the first waveguide with I_{in} = 100 mA and the coupling factor C=0. (a) The temporal output and (b) the power spectral density of the temporal output in log scale. (c) (d) The zoomed power spectral density and temporal output of the first waveguide. The output electric field is quasiperiodic and takes more than 200 ns to reach steady state.

We first solved a single waveguide model by setting the coupling factor of $C = 0$ so there is no coupling between waveguide. The input currents to the first two waveguides are set to be

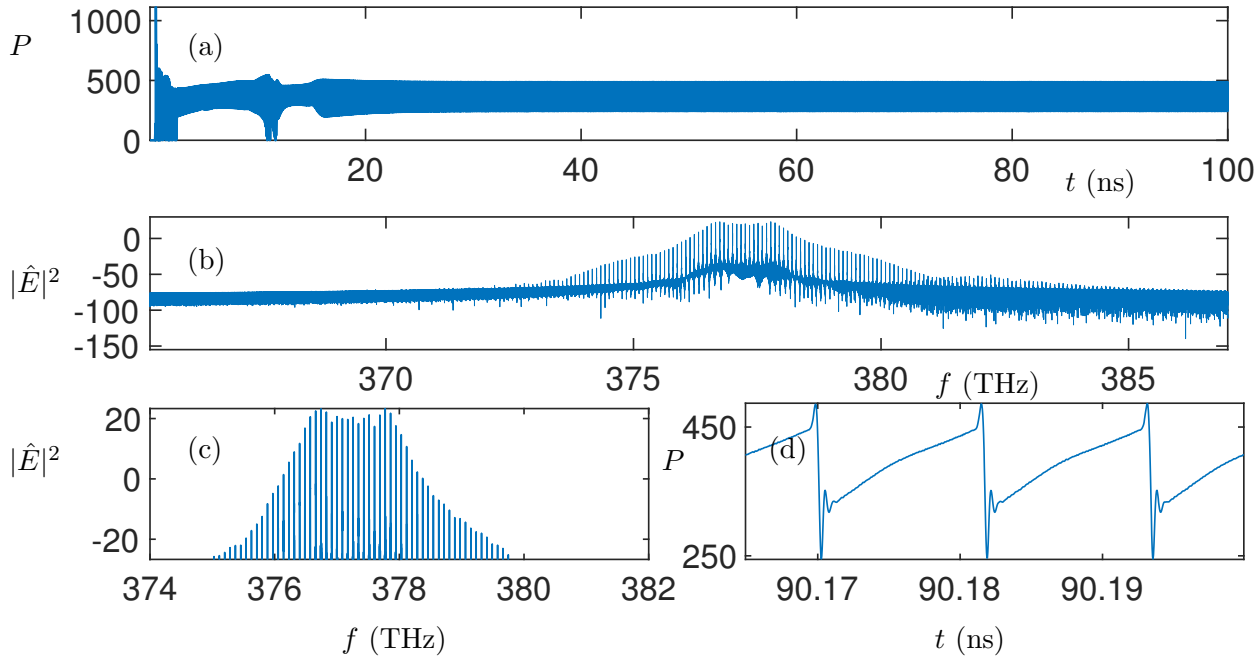

Figure 3.4: Evolution of output power P (mW) and power spectral density $|\hat{E}|^2$ (dBm/Hz) in the first waveguide with $I_{1in} = 100$ mA, $I_{2in} = 0$ and the coupling factor C=1. (a) The temporal output inside waveguide 1. A stable state is achieved for $t > 30$ ns. (b) A broad comb is shown in the power spectral density of the temporal output in log scale. (c) (d) The zoomed power spectral density and temporal output of the first waveguide. The output includes a periodic short burst on top of a continuous wave. Although it narrows down in the power spectral density, the spectrum is of higher intensity and a flatter plateau.

(a)

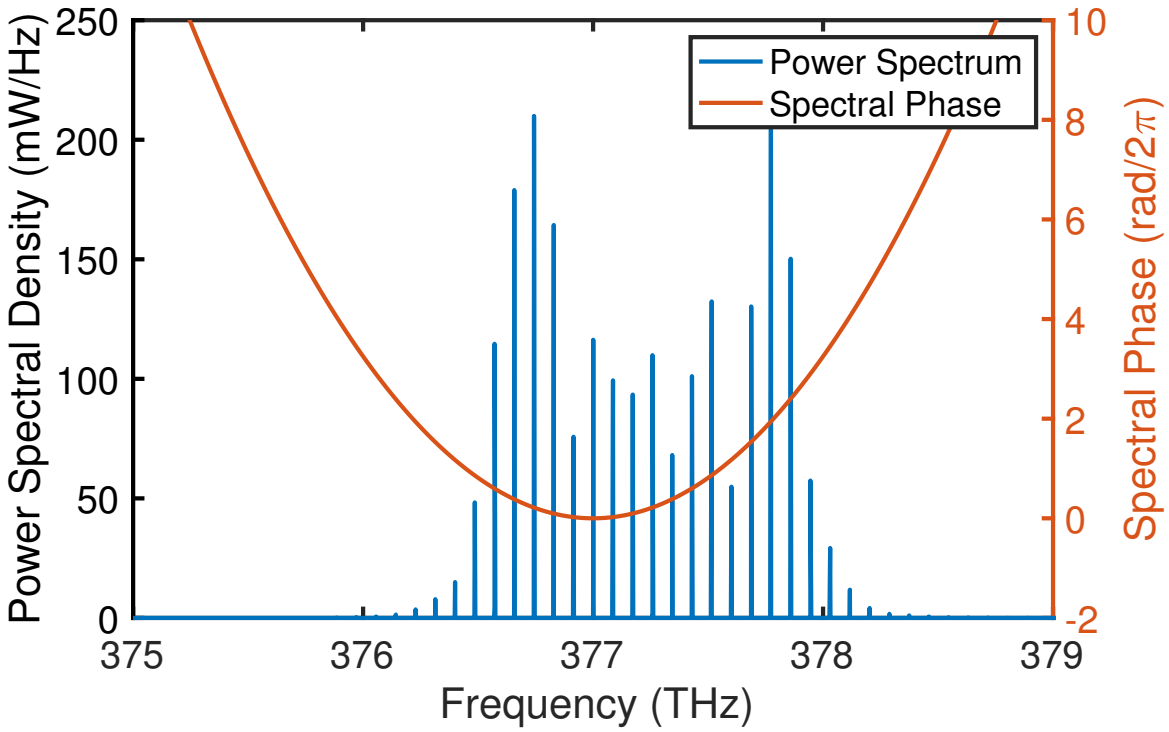
Power Spectrum
Spectral Phase
Power Spectral Density (mW/Hz)
Spectral Phase (rad/2π)
Frequency (THz)
250
200
150
100
50
0
10
8
6
4
2
0
-2
375
376
377
378
379

(b)

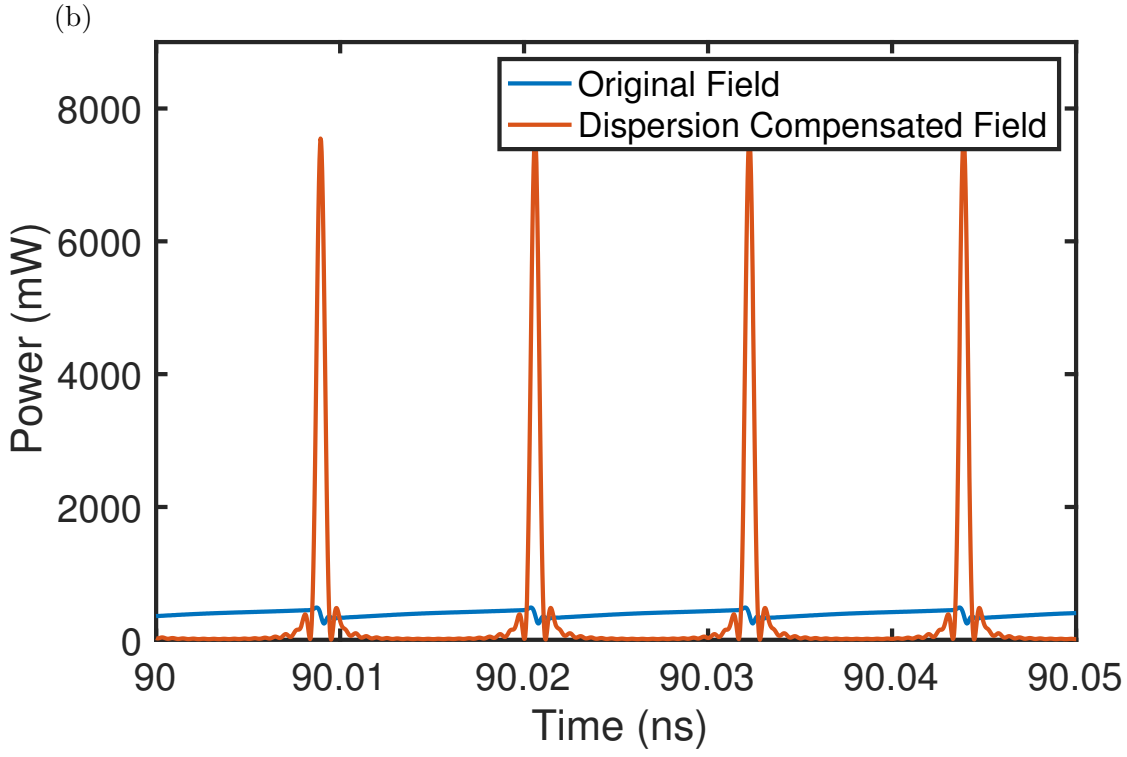
Original Field
Dispersion Compensated Field
Power (mW)
Time (ns)
8000
6000
4000
2000
0
90
90.01
90.02
90.03
90.04
90.05

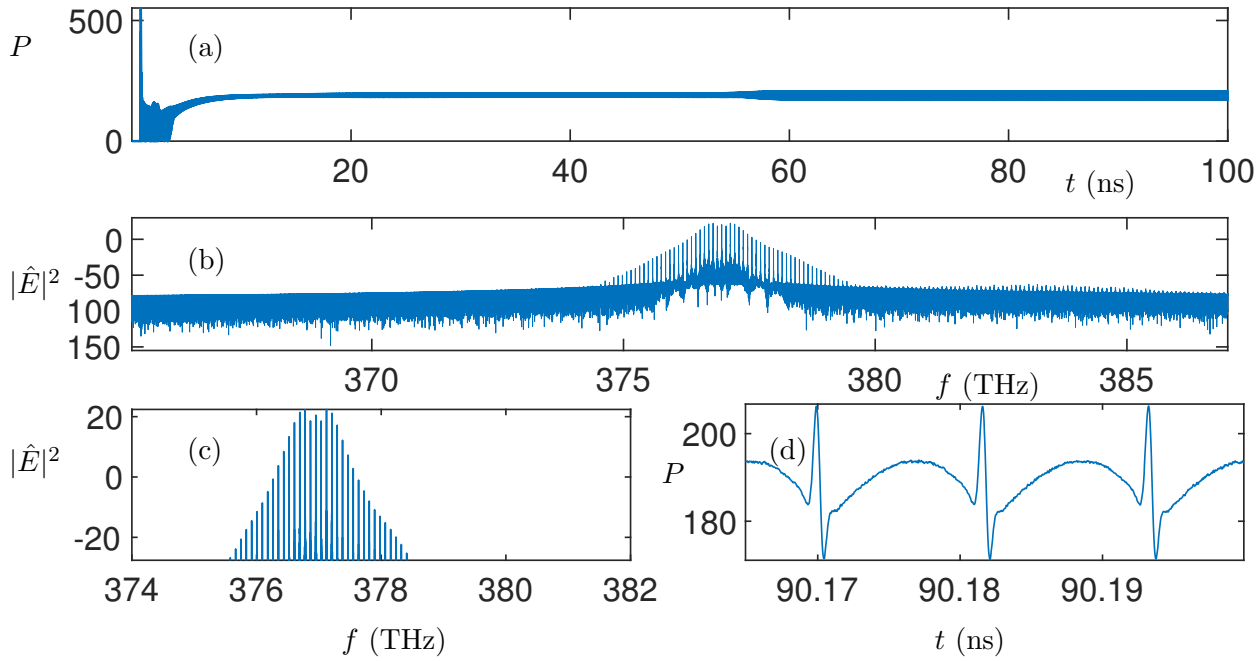

Figure 3.6: Evolution of output power P (mW) and power spectral density $|\hat{E}|^2$ (dBm/Hz) in the first waveguide with $I_{1in} = 100$ mA, $I_{2in} = 0$ and the coupling factor C=2. (a) The temporal output and (b) power spectral density of the temporal output in log scale of the first waveguide. Longer time is needed to reach a steady state ($t > 60$ ns). (c) (d) The zoomed power spectral density and temporal output of the first waveguide. The output power is further lowered and the spectral density is narrowed down as well. Note that simulations of the laser evolution for much longer times confirm that it stabilizes to the dynamics shown in (c) and (d).

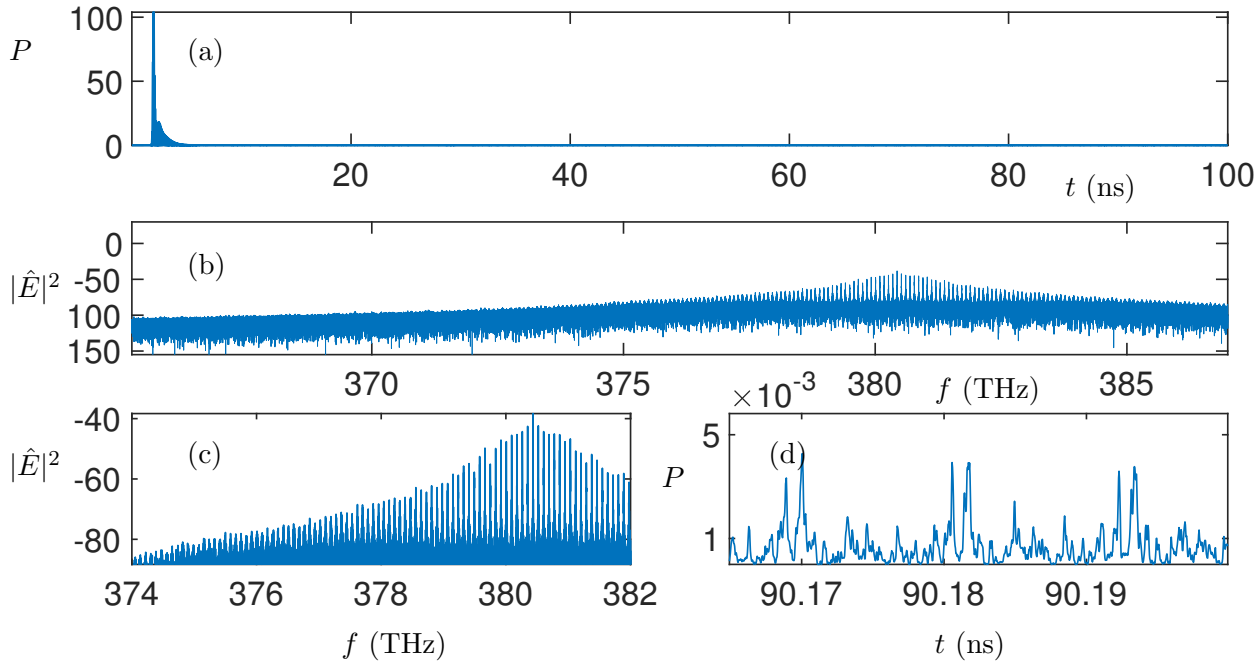

Figure 3.7: Evolution of output power P (mW) and power spectral density $|\hat{E}|^2$ (dBm/Hz) in the first waveguide with $I_{1in} = 100$ mA, $I_{2in} = 0$ and the coupling factor C=3. (a) The temporal output and (b) power spectral density of the temporal output in log scale of the first waveguide. The output power quickly dies to a low value. (c) (d) The zoomed power spectral density and temporal output of the first waveguide. The gain is insufficient to pump the wave compared to the energy loss and we are left with the low-power white noises in the cavity.

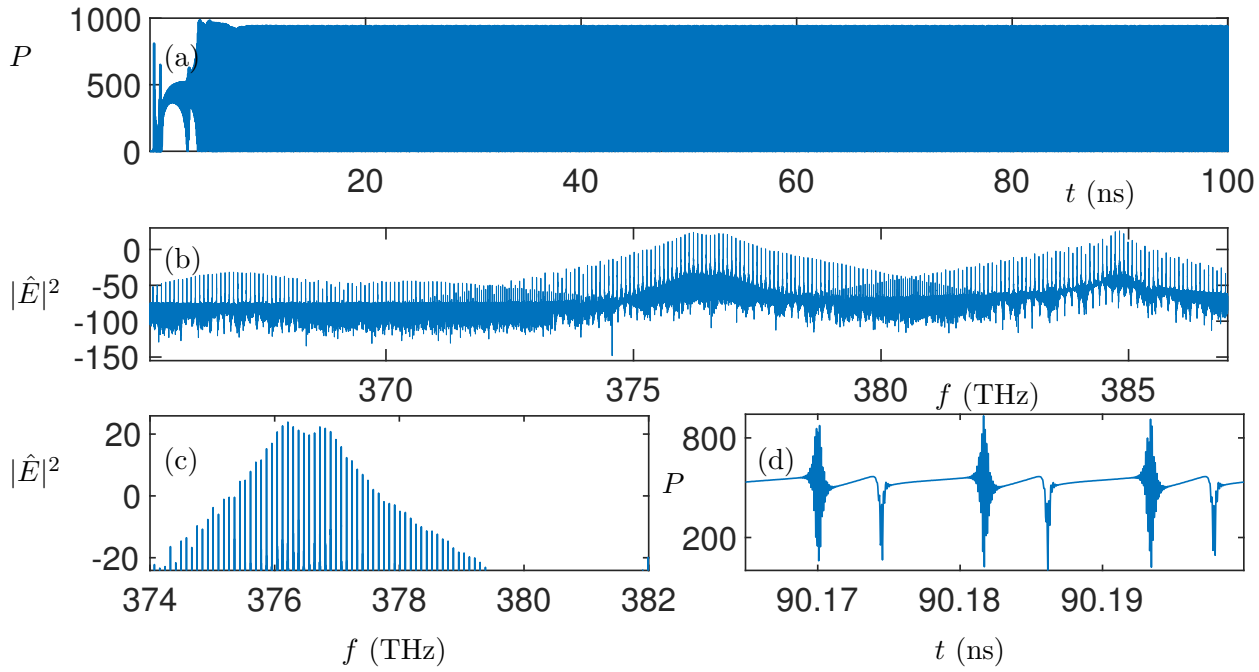

Figure 3.8: Evolution of output power P (mW) and power spectral density $|\hat{E}|^2$ (dBm/Hz) in the first waveguide with $I_{1in} = 350$ mA, $I_{2in} = 0$ and the coupling factor C=3. (a) The temporal output and (b) power spectral density of the temporal output in log scale of the first waveguide. (c) (d) The zoomed power spectral density and temporal output of the first waveguide. With increased input current to the first waveguide, the gain is sufficient to pump the wave compared to the energy loss. Interestingly, a second peak in the spectrum is generated, suggesting that the second waveguide is lasing as well.

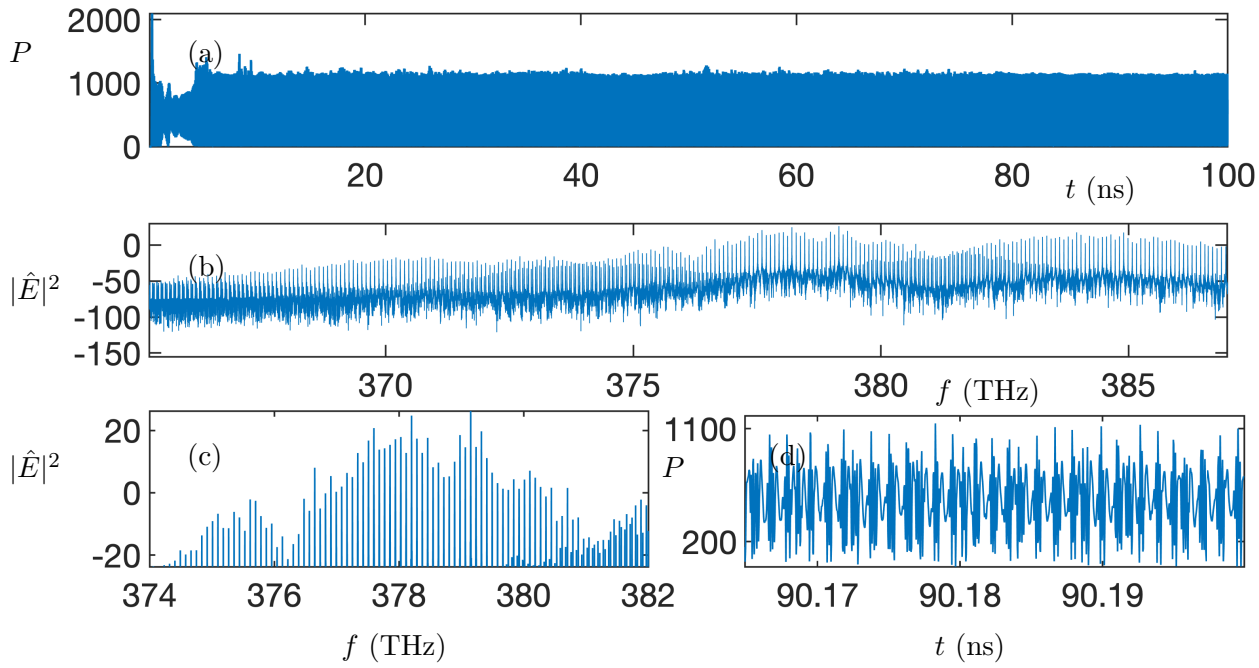

Figure 3.9: Evolution of output power P (mW) and power spectral density $|\hat{E}|^2$ (dBm/Hz) in the first waveguide with $I_{1in} = 100$ mA, $I_{2in} = 0$ and the coupling factor C=1. The maximum of E_t is increased from 50meV to 100meV in this case. (a) (b) The temporal output and the power spectral density of the temporal output in log scale of the first waveguide. (c) (d) The zoomed power spectral density and temporal output of the first waveguide. Increased quantum well depth in the simulation contributes to the gain and causes a split in the spectrum. The mode-locked state falls to chaos in the cavity.

$I_{1in} = 100$ mA and $I_{2in} = 0$ for the following experiments studying the impact of varying the coupling factor C. The quantum well depth $\max(E_t)$ is set to be 50 meV. As shown in Fig. 3.3, it took nearly 200 ns for the output to reach a quasi-periodic steady state with very high frequency oscillations and a spectrum indicating the presence of mode competition. Turning on the coupling factor with a small value, e.g. $C = 0.5$, does not stabilize the chaotic electric field in the cavity. When the coupling factor C is increased to unity, the electric field inside the cavity rapidly stabilizes to a mode-locked periodic state, see Fig. 3.4 in less than 50 ns and the spectrum exhibits a frequency comb with lines spaced by the round-trip frequency of 85.7 GHz. To show the periodic and coherent output is mode-locked, the spectrum and spectral phase are plotted on a linear scale, as shown in Fig. 3.5(a). The quadratic spectral phase shows that the frequency comb from this chip-scale device is coherent and can thus be used in applications such as spectroscopy and metrology. If one desires short pulses the quadratic phase can be compensated by propagating through another waveguide or fiber with anomalous dispersion, resulting in the output shown in Fig. 3.5(b). The required group delay dispersion is calculated to be 0.52 ps^2. If we increase the value of the coupling factor C from 1 to 2 (Fig. 3.6), the mode-locked state still holds in the cavity, and the distance between comb lines is not changed. However, the output power of the electric field in the first waveguide is decreased. This is reasonable since more energy gets coupled to the neighboring waveguides and dissipated in the 3rd waveguide. If the coupling factor gets too large, for example, $C = 3$ in this case (Fig. 3.7), a large amount of energy gets coupled to the neighboring waveguides and we are no longer able to get to an equilibrium, or balance, of the gain and the loss dynamics, thus the mode locked state disappears. Interestingly, if the input current to the first waveguide is increased to $I_{1in} = 350$ mA with C=3, the output power of the first waveguide is prevented from dying. Instead, we are left with a two-peak spectrum, as shown in Fig. 3.8. This suggests that the second waveguide is also lasing. Considering the second waveguide has no input current, the lasing is likely pumped by increased energy coupled out from the first waveguide with a larger coupling factor C=3, and it equivalently balances the energy loss of cavity.

In the simulations above, the input current to the first waveguide is set to be I_{in}=100 mA. There is no energy pumping (gain from current injection) applied to the second and third waveguides in the array. Waveguide two experiences a net intrinsic loss with $\alpha = 5$ cm^{-1}, whereas an extra electron and hole sweep out with lifetime 0.1 ps and 0.3 ps exists in waveguide three as it is reverse biased.

With the energy step remaining as 2 meV but the quantum well depth max(E_t) increased to 100 meV, the mode-locked state does not hold with the coupling factor $C = 1$ and the electric field inside waveguide one falls back to the chaotic state, as shown in Fig. 3.9. Since the limit of E_t equivalently contributes to the gain, we test another case when max(E_t) remains 50 meV but the input pump on the first waveguide is increased to 200 mA. Neither of these parameter regimes are capable of producing a repeatable waveform.

An extra gain to the second waveguide is added to make it nearly neutral from a gain-loss perspective in order to better shape the frequency combs. The results are shown in Fig. 3.10-3.13, where the input current to the first waveguide is maintained as 100 mA and the coupling factor C is set to be 1. Meanwhile, the input current to the second waveguide is increased from 10 mA to 100 mA. Applying low input current, e.g. current less than 30 mA, to the second waveguide can slightly increase the output power but does not affect the results significantly, as shown in Fig. 3.10. In contrast, when the input current is increased to 50 mA, the distance between each comb line is increased to about 1 THz and the electric field oscillates in a shorter period in the time domain, perhaps indicating a harmonically mode-locked state. When the input current is increased to 80 mA, secondary comb lines appear around the central ones in the power spectral density but the electric field remains in the periodic state in the time domain. Increasing the input current to 100 mA destroys the balance between the loss and gain and the system falls into the chaotic state.

3.4 Conclusion

In this chapter, we have presented computational evidence that a traveling wave model for a quantum well and the mode-coupling in a waveguide array can generate frequency combs

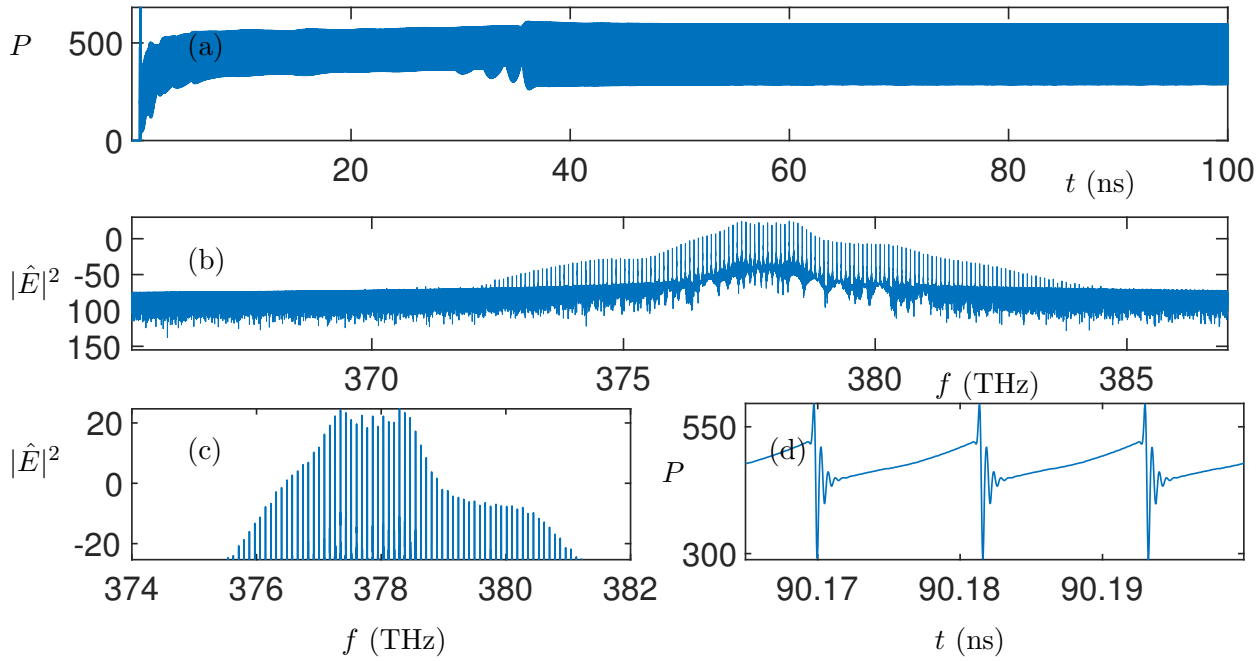

Figure 3.10: Evolution of output power P (mW) and power spectral density $|\hat{E}|^2$ (dBm/Hz) in the first waveguide with I_{1in}=100 mA, I_{2in}=30 mA and the coupling factor C=1. (a) The temporal output and (b) the power spectral density of the temporal output in log scale of the first waveguide. (c) (d) The zoomed power spectral density and temporal output of the first waveguide. Compared to Fig. 3.6, the electric output still remains in a similar shape with a higher output power in the time domain.

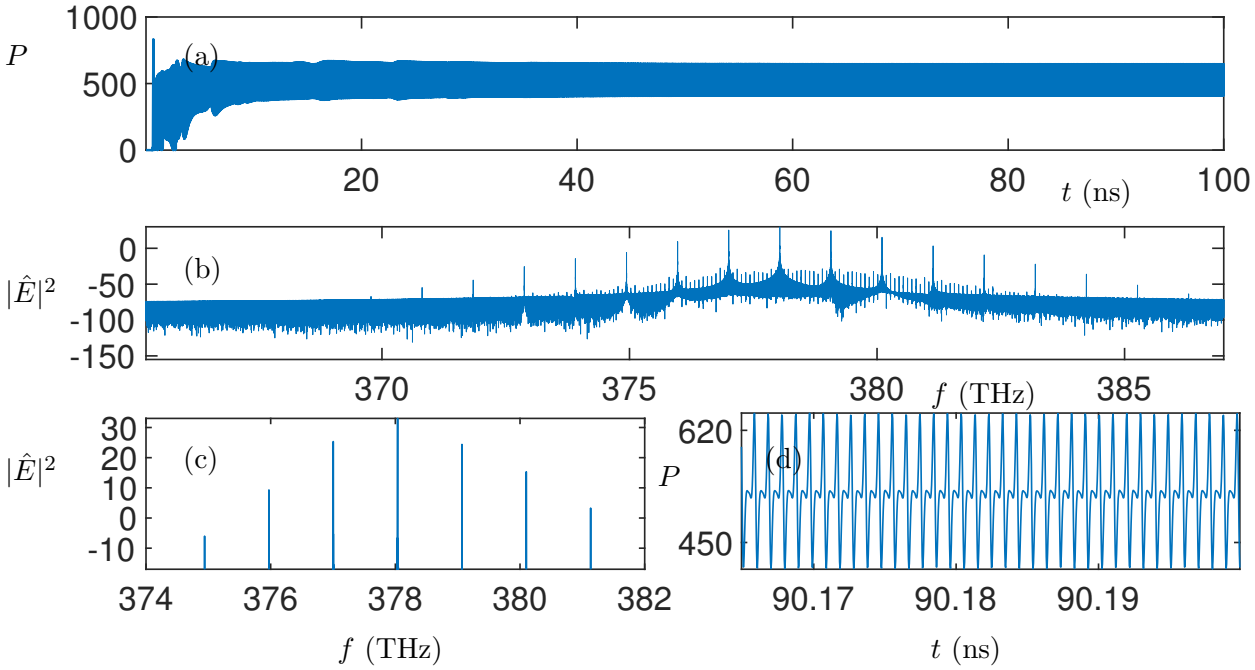

Figure 3.11: Evolution of output power P (mW) and power spectral density $|\hat{E}|^2$ (dBm/Hz) in the first waveguide with I_{1in}=100 mA, I_{2in}=50 mA and the coupling factor C=1. (a) The temporal output and (b) the power spectral density of the temporal output in log scale of the first waveguide. (c) (d) The zoomed power spectral density and temporal output of the first waveguide. The increased input pump to the second waveguide has a significant impact on the output of the waveguide array. The period of the electric output in the time domain is largely decreased while the power spectral density has a wider separation between each comb line.

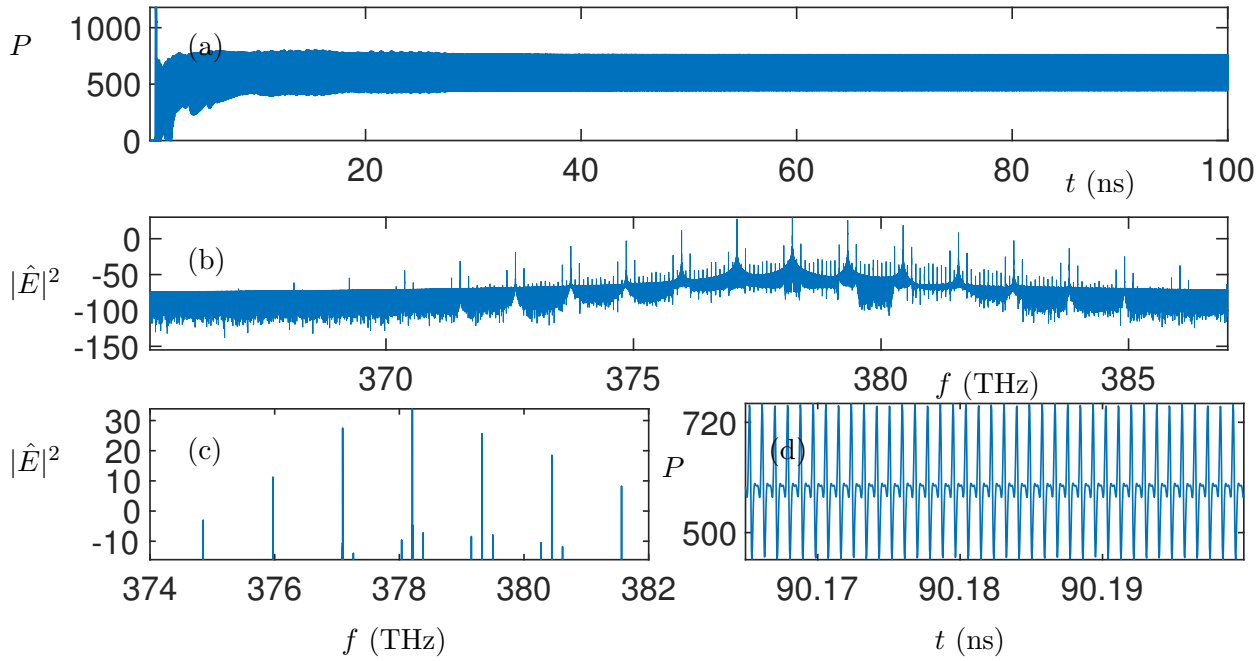

Figure 3.12: Evolution of output power P (mW) and power spectral density $|\hat{E}|^2$ (dBm/Hz) in the first waveguide with I_{1in}=100 mA, I_{2in}=80 mA and the coupling factor C=1. (a) The temporal output and (b) the power spectral density of the temporal output in log scale of the first waveguide. (c) (d) The zoomed power spectral density and temporal output of the first waveguide. Compared to Fig. 3.11, extra comb lines arise around the central lines due to a higher input pump.

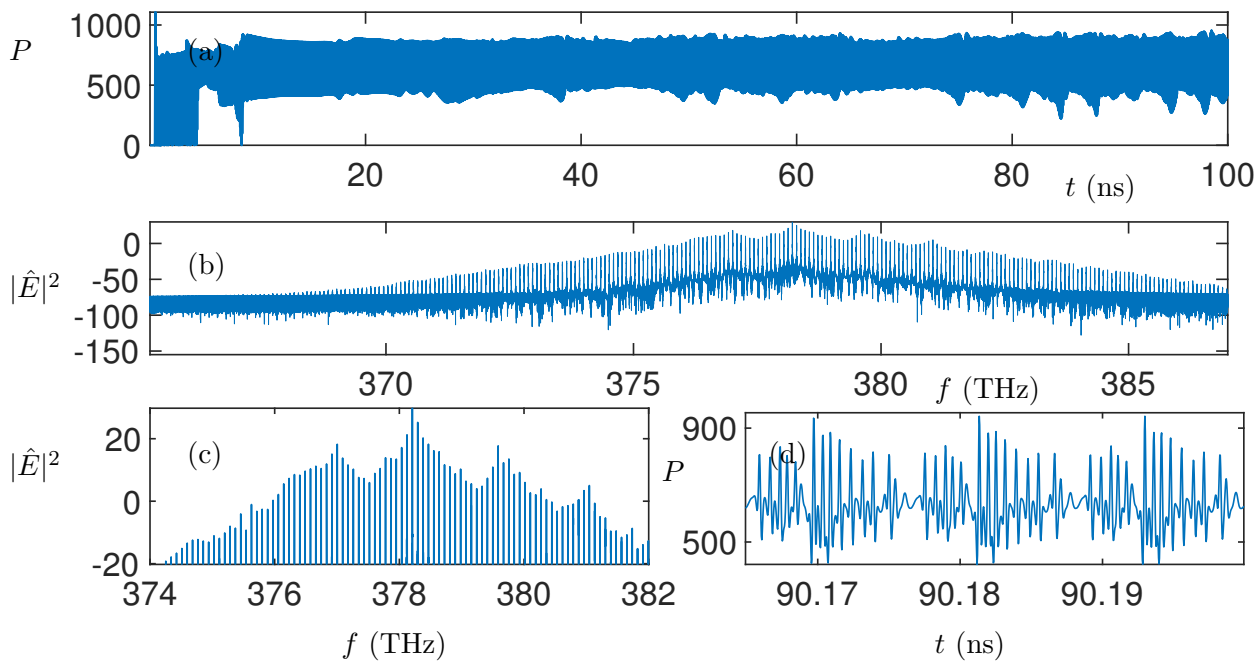

Figure 3.13: Evolution of output power P (mW) and power spectral density $|\hat{E}|^2$ (dBm/Hz) in the first waveguide with I_{1in}=100 mA, I_{2in}=100 mA and the coupling factor C=1. (a) The temporal output and (b) the power spectral density of the temporal output in log scale of the first waveguide. (c) (d) The zoomed power spectral density and temporal output of the first waveguide. The input pump to the second waveguide is sufficiently strong to break the balance between the gain and loss in the waveguide array, thus the mode-locked state is destroyed in this case.

at 800 nm. The mode coupling of the waveguide array provides the necessary intensity discrimination and controllable loss for pulse shaping stabilizing the generation of a repeatable waveform and frequency comb in the cavity. To experimentally realize stable, robust comblines, the coupling factor between waveguides in the array must be optimized.

We explored the parameter space of WGA coupling factor C, input currents to the waveguides, waveguide biases, energy steps and energy limits, to understand the different performance characteristics of the waveguide array model and its dependency on the WGA parameters. The mode-locking behavior is sensitive to certain directions of the parameter space. In particular, if the coupling factor C is too large, the excess coupling loss can lead to quenching of laser action. For properly chosen parameters the numerical results demonstrate the generation of frequency combs at 800 nm with the coupled waveguide array for a quantum well. This combined model of diode lasers can serve as an excellent candidate for compact, efficient and robust comb sources experimentally.

Chapter 4

STABLE NUMERICAL SCHEMES FOR NONLINEAR DISPERSIVE EQUATIONS WITH COUNTER-PROPAGATION AND GAIN DYNAMICS

This chapter[1] provides details of the numerical realization of the model discussed in Chapter 3. We develop a stable and efficient numerical scheme for modeling the optical field evolution in a nonlinear dispersive cavity with counter propagating waves and complex, semiconductor physics gain dynamics that are expensive to evaluate. Our stability analysis is characterized by a von-Neumann analysis which shows that many standard numerical schemes are unstable due to competing physical effects in the propagation equations. We show that the combination of a predictor-corrector scheme with an operator-splitting not only results in a stable scheme, but provides a highly efficient, single-stage evaluation of the gain dynamics. Given that the gain dynamics are the rate-limiting step of the algorithm, our method circumvents the numerical instability induced by the other cavity physics when evaluating the gain in an efficient manner.

4.1 Introduction

Computational methods play a fundamental role in scientific exploration and model development across the physical and engineering sciences. Simulations help provide critical understanding of physical processes and their interactions in complex systems. Further, they can provide proof-of-concept engineering designs before expensive manufacturing and/or experiments are performed. From the aerospace industry to optical laser physics, initial designs are now often simulated with physics-based models in order to achieve a qualitative under-

[1]Content of this chapter is published in journal article [137].

standing of the physical interactions, good parameter regimes, and robustness of a physical design. Critical in this process is the construction of stable numerical schemes that provides both accuracy and stability for modeling the underlying physics. Here we develop a robust and stable time-stepping algorithm for modeling counter-propagating waves in a diode laser subject to gain and loss dynamics. Specifically, we show that an operator splitting scheme with predictor-corrector time-stepping can circumvent the numerical instabilities generated by standard algorithms that are typically used for either counter-propagating waves or for modeling the complex gain dynamics, but not both. Moreover, the proposed method allows for computational efficiency when modeling the complex semiconductor gain dynamics, thus leading to a robust, stable, and computationally efficient numerical scheme. The analysis also shows that the scheme can be more broadly applied to nonlinear dispersive wave equations that include competing instability effects from counter-propagating waves and gain dynamics.

Diode lasers are a ubiquitous technology that have been well developed in theory and experiment. Emerging research efforts aim to exploit diode lasers in order to generate repeatable waveforms, or mode-locked diode lasers (MLDL), that can be used for robust frequency combs [42]. As previously stated, while theoretical comb generation in a QD single-section laser [50] has been reported, only recently has a detailed model for the FM comb generation in the QW diode laser been developed [42]. To properly account for how FM combs are formed in QW lasers, the electric field modulation of multiple cavity modes, cavity dispersion, carrier induced refractive index shift, spectral and spatial hole burning and some intraband carrier dynamics are considered in this model. The gain model builds on recent semiconductor gain models [25, 50], but is tailored to quantum well nanostructures [42].

Robust and efficient simulations of the detailed governing equations of the diode laser physics are critical [42]. Not only must a time-stepper be developed that is stable, but the complexity of the semiconductor physics requires the implementation of an efficient scheme. Typically the gain dynamics is modeled with a simple Euler method [25, 50, 42] since this requires only a single stage and can greatly reduce the computational costs. However, such

Euler schemes generate numerical instabilities when the effects of counter-propagating waves and chromatic dispersion are included in the cavity. Leap-frog schemes, which are at the core of FDTD (finite-difference, time-domain) methods, are quite effective in handling the counter-propagating waves, but they generate numerical instability when modeling the gain dynamics. Thus the standard schemes produce competing instabilities. The stability of a numerical scheme is typically evaluated using a von-Neumann analysis [84], where conditions for stability, such as constraints on the CFL (Courant-Frederiks-Lewy) number can be explicitly evaluated. Here we show that an operator splitting technique and predictor-corrector structure allows us to posit a stable and robust scheme for nonlinear, dispersive optical field propagation that is computationally efficient and accurate. We explicitly demonstrate the instability mechanisms present in the various physics of our model and motivate the development of our stable method.

This chapter is outlined as follows: In Sec. 2, we briefly restate the governing equations for the diode laser physics. Section 3 evaluates the numerical stability of a variety of time-stepping schemes, showing that the various physical effects in our model produce competing instabilities that require the development of our method. The numerical stability analysis is performed using a standard von-Neumann analysis. Section 4 develops the numerical scheme for the application of the diode laser physics of interest. Numerical results of our simulation are shown in Sec. 5, with concluding comments in Sec. 6.

4.2 Governing Equations

The diode laser model captures the physics of counter-propagating of the electric fields $E^{\pm}(x,t)$. For the specific application where mode-locking is of interest, the standard CW dynamics models must be modified to include chromatic dispersion. Thus a variety of dominant physical effects are present in the laser: counter-propagating waves, dispersion, self-phase modulation due to the Kerr effect, dissipation due to cavity losses, and semiconductor gain dynamics. Aside from the gain dynamics, which is extremely detailed and complex [25, 50, 42], the remaining physical effects can be easily incorporated into a simple

model with distinct interacting terms. With the four-wave-mixing cross terms neglected, the governing propagation equations for the electric field are

$$\frac{\partial E^+}{\partial x} + \frac{1}{v_g}\frac{\partial E^+}{\partial t} + i\frac{k''}{2}\frac{\partial^2 E^+}{\partial t^2} = -(\frac{\alpha_s}{2} + i\beta_s)(|E^+|^2 + 2|E^-|^2)E^+ + G^+(E^\pm) - \frac{\alpha}{2}E^+ + S^+_{sp}, \tag{4.1a}$$

$$-\frac{\partial E^-}{\partial x} + \frac{1}{v_g}\frac{\partial E^-}{\partial t} + i\frac{k''}{2}\frac{\partial^2 E^-}{\partial t^2} = -(\frac{\alpha_s}{2} + i\beta_s)(|E^-|^2 + 2|E^+|^2)E^- + G^-(E^\pm) - \frac{\alpha}{2}E^+ + S^-_{sp}, \tag{4.1b}$$

where k'' measures the chromatic dispersion in the waveguide [66, 65], $v_g = c/n_0$ is the group velocity, α_s is the two-photon absorption and β_s is the Kerr nonlinear coefficient. α is the linear waveguide loss, and S_{sp} is a spontaneous emission term derived in [42]. The interplay of nonlinearity with dispersion is typically critical for stabilizing a waveform once energy balance is achieved between cavity losses and gain saturation [85].

The complex, semiconductor gain physics is included in the term $G^\pm$. This term is discussed in more detail in Sec. 3. The gain dynamics is computationally expensive to evaluate [42], thus a numerical scheme that can efficiently evaluate the $G^\pm$ is required. Specifically, a standard scheme such as 4th-order Runge-Kutta requires a four-stage evaluation process that would require evaluating $G^\pm$ four times before updating the solution in the time-stepper. While the Runge-Kutta scheme has superior stability properties, the four state evaluation would render an already expensive computation significantly longer.

To simulate the governing equations, appropriate numerical schemes must be considered. In addition to speed and accuracy, the stability of the underlying scheme is of paramount importance. As will be shown in the next section, the simple structure of the linear terms gives rise to competing numerical instabilities. Thus a scheme that is ideal for handling counter-propagation, generates an instability due to the presence of the dispersion. And conversely, a scheme that is well suited for the dispersion easily leads to an instability from the counter-propagation. These competing instabilities must be circumvented while maintaining a simple evaluation (one-stage) of $G^\pm$.

4.3 Stability of Time-Stepping Schemes and von-Neumann Analysis

We consider the numerical stability properties with standard finite difference discretization schemes. Although an Euler stepping scheme appears to work for the cavity dynamics without dispersion [42], the introduction of dispersion guarantees the solution technique is unstable. We consider a subset of the terms in Eqs. (4.1), the interaction of propagation and dispersion:

$$\frac{\partial E}{\partial x} = \frac{1}{v_g}\frac{\partial E}{\partial t} + iD\frac{\partial^2 E}{\partial t^2}. \tag{4.2}$$

This describes the interaction of one-way wave propagation with speed v_g and chromatic dispersion with strength D. A von-Neumann analysis provides the stability of different numerical discretization schemes of the electric field. A von-Neumann analysis proceeds by letting [84]

$$E(x_m, t_n) = E_n^m = g^m exp(i\xi_n h), \tag{4.3}$$

where h is the fundamental frequency, $\xi_n = n\xi$ with ξ defining the numerical step size taken in the propagation direction t. The index n denotes the discretization of the field in time, while m denotes the discretization along the propagation direction x. Substituting E_n^m into the discretized equations associated with Eq. (4.2) yields an iterative equation for g. Importantly, the norm of $|g|$ determines the stability of the time stepping scheme. If $|g| > 1$ the iteration scheme is unstable, while $|g| < 1$ ensures linear stability. A von-Neumann analysis determines $|g|$ to evaluate stability.

4.3.1 Euler time-stepping scheme

Defining Δx and Δt as the discretization in x and t respectively, and implementing Euler time-stepping scheme [84] of Eq. (4.2) results in

$$\frac{E_n^{m+1} - E_n^m}{\Delta x} = \frac{E_{n+1}^m - E_{n-1}^m}{2v_g\Delta t} + \frac{iD}{\Delta t^2}(E_{n+1}^m - 2E_n^m + E_{n-1}^m). \tag{4.4}$$

Substituting the von-Neumann decomposition, Eq. (4.3), into Eq. (4.4) and simplifying yields

$$g = 1 + i(\frac{v_g\Delta x}{\Delta t}sin\xi h - 4\frac{D\Delta x}{\Delta t^2}sin^2\frac{\xi h}{2}). \tag{4.5}$$

We find

$$|g|^2 = 1 + \left(\frac{\Delta x}{v_g \Delta t} sin\xi h - 4 \frac{D\Delta x}{\Delta t^2} sin^2 \frac{\xi h}{2} \right)^2 > 1, \tag{4.6}$$

which ensures that $|g| > 1$ for all Δx and Δt. Therefore, the Euler time-stepping scheme in this case is guaranteed to produce numerical instability. Thus the inclusion of these terms in the full model of Eq. (4.1) makes an Euler scheme unstable. Note that without the dispersion and counter-propagation, the Euler method was exactly what was used previously [25, 50].

4.3.2 Backward Euler time-stepping scheme

A standard way to stabilize the Euler scheme is implicit formulation [84]. Indeed, implicit methods are generally more favorable when the algorithm stability is considered. However, the implicit formulation comes at a price as will be shown. Specifically, applying the backward Euler scheme on the wave equation with both propagation and chromatic dispersion, we obtain

$$\frac{E_n^{m+1} - E_n^m}{\Delta x} = \frac{E_{n+1}^{m+1} - E_{n-1}^{m+1}}{2 v_g \Delta t} + \frac{iD\Delta x}{\Delta t^2} (E_{n+1}^{m+1} - 2E_n^{m+1} + E_{n-1}^{m+1}). \tag{4.7}$$

This can be compared with the standard Euler time-stepping algorithm to see that the future state of the system is required to evaluate the time-step. For linear equations, this is not necessarily problematic, but it is often difficult to accomplish for nonlinear schemes.

Again substituting the von-Neumann decomposition Eq. (4.3) into the above and simplifying yields

$$|g| = \frac{1}{\sqrt{1 + (\frac{\Delta x}{v_g \Delta t} \sin \xi h + \frac{2D\Delta x}{\Delta t^2} (\cos \xi h - 1))^2}} < 1. \tag{4.8}$$

Consequently the backward Euler stepping scheme is more robust than the forward Euler scheme since $|g| < 1$ is satisfied with no constrains on the discretization size Δx and Δt. In fact, implicit stepping schemes are known to be exceptionally stable but are less used since it is more expensive than the explicit stepping schemes. Specifically, to obtain information of the future steps, the predictor-corrector scheme is consequently used, which can be extremely time-consuming when it is applied to the full wave equation with the existence of the gain

term. We are thus interested in developing a less time-consuming but more generally robust stepping scheme.

4.3.3 Leap-frog (2,2) time-stepping scheme

The discretized form of the equation including propagation and dispersion with a leap-frog (2,2) method [84] is

$$\frac{E_n^{m+1} - E_n^{m-1}}{2\Delta x} = \frac{E_{n+1}^m - E_{n-1}^m}{2v_g\Delta t} + \frac{iD}{\Delta t^2}(E_{n+1}^m - 2E_n^m + E_{n-1}^m). \tag{4.9}$$

Again substituting the von-Neumann decomposition Eq. (4.3) into the above and simplifying yields

$$g = \frac{1}{2}(iM \pm \sqrt{4 - M^2}). \tag{4.10}$$

where

$$M = 2\frac{\Delta x}{v_g\Delta t}\sin\xi h + 4\frac{D\Delta x}{\Delta t^2}(\cos\xi h - 1). \tag{4.11}$$

Depending on whether $4 - M^2 \geq 0$, we have

$$g = \begin{cases} \pm\frac{1}{2}\sqrt{4 - M^2} + i\frac{M}{2}, & 4 - M^2 \geq 0, \\ \frac{i}{2}(M \pm \sqrt{M^2 - 4}), & 4 - M^2 < 0, \end{cases} \tag{4.12}$$

For $4 - M^2 < 0$,

$$|g|^2 = \frac{1}{4}(M \pm \sqrt{M^2 - 4})^2 = \frac{1}{2}(M^2 - 2 \pm M\sqrt{M^2 - 4}). \tag{4.13}$$

In this case $M^2 > 4$ which gives

$$|g|^2 = \frac{1}{2}(M^2 - 2 + M\sqrt{M^2 - 4}), \tag{4.14}$$

so that $|g|^2 > 1$ and the leap-frog (2,2) time-stepping scheme is unstable.

For $4 - M^2 \geq 0$,

$$|g|^2 = \frac{1}{4}(4 - M^2) + \frac{M^2}{4} = 1, \tag{4.15}$$

thus the algorithm is at the stability boundary $|g| = 1$. For this case, we obtain the constraints on M as $-2 \leq M \leq 2$, that is,

$$-1 \leq \frac{\Delta x}{v_g \Delta t} sin\xi h + 2\frac{D\Delta x}{\Delta t^2}(cos\xi h - 1) \leq 1. \tag{4.16}$$

This constraint can be satisfied by selecting the discretization sizes Δx and Δt as shown in Fig. 4.1. The associated simulation results are shown in Fig. 4.2. Without the constraint of stability satisfied, the propagation along direction of x grows unexpectedly whereas within the stable region, this propagation is smooth and constrained. However, the inclusion of the gain terms into the leap-frog (2,2) scheme generates instability, thus we need a more robust numerical scheme for the more general case.

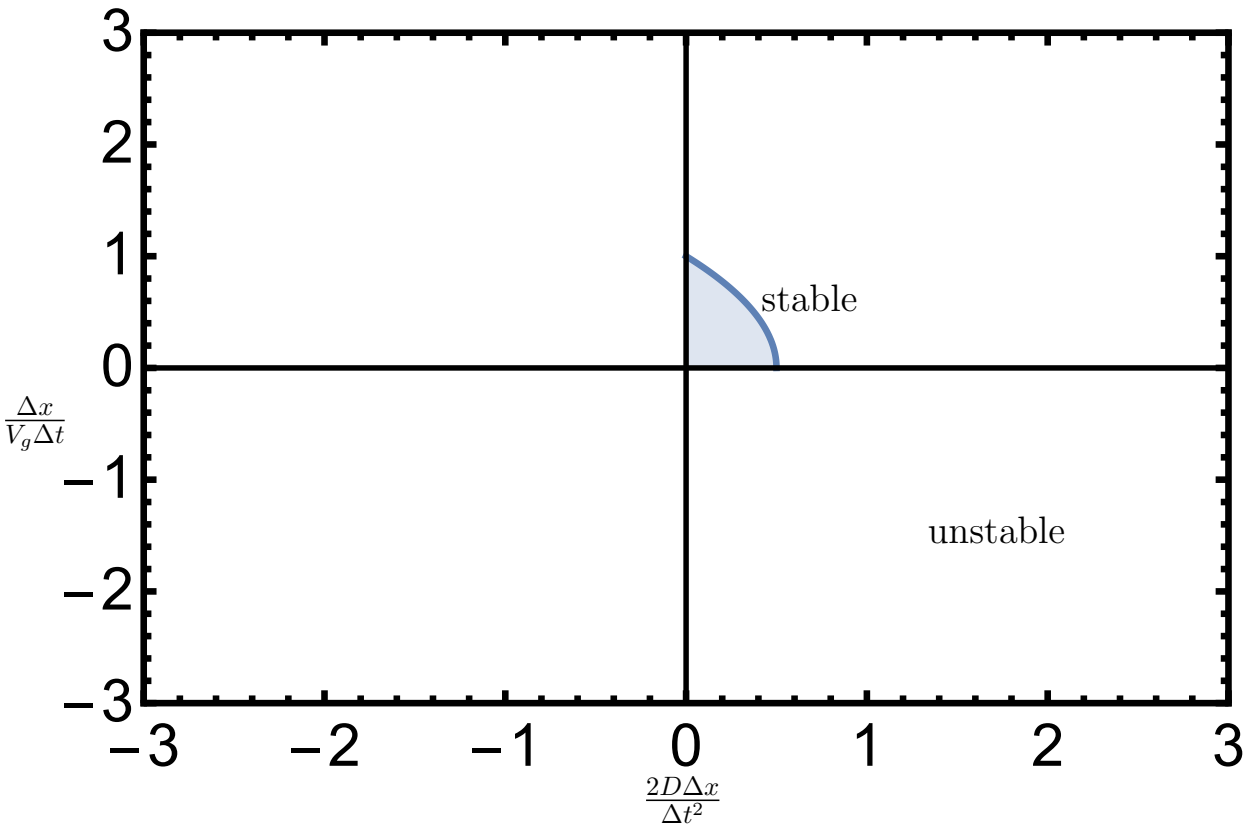

Figure 4.1: Regions for stable stepping of the wave equation with propagation and chromatic dispersion using the leap-frog (2,2) scheme.

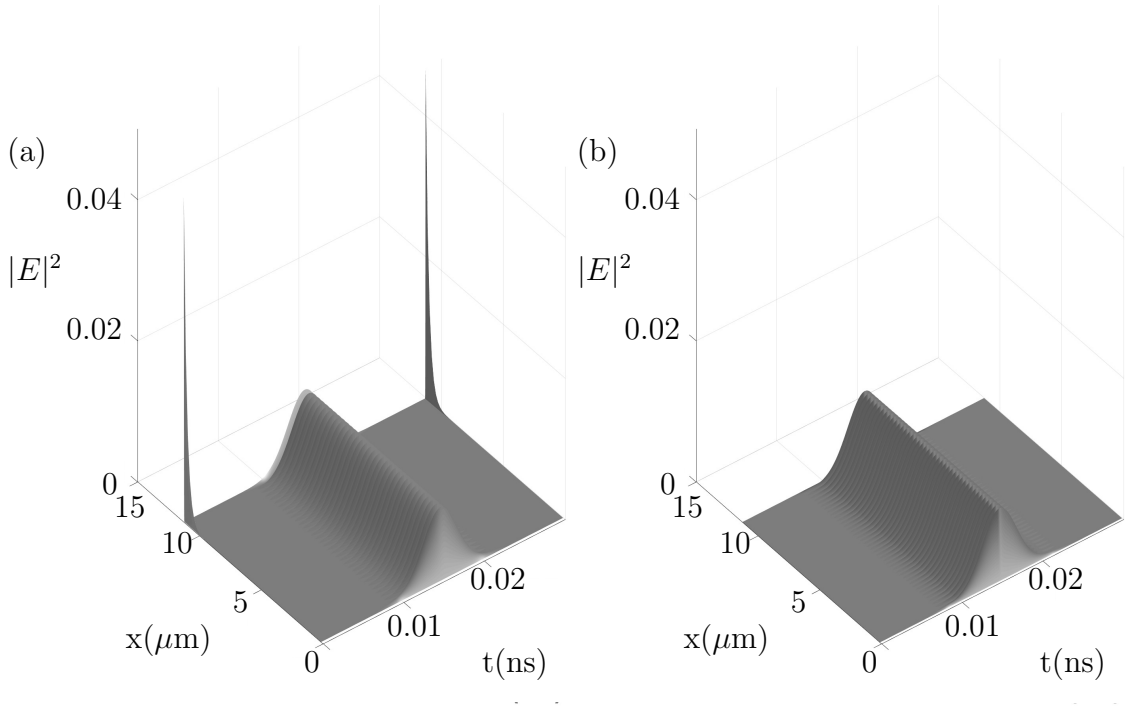

Figure 4.2: Associated numerical results of the unstable and stable region using leap frog (2,2). (a) The numerical solution quickly blows up without satisfying the constraints on the discretized steps Δx and Δt. (b) Numerical result consistently demonstrates the stability within the shaded region in Fig. 4.1.

4.3.4 Predictor-corrector time-stepping scheme

Considering the more general case that includes propagation, chromatic dispersion and gain, the predictor-corrector scheme provides an appropriate stable implementation that makes use of both forward and backward Euler time-stepping due to their speed and stability respectively. Consider the more general equation

$$\frac{\partial E}{\partial x} = \frac{1}{v_g}\frac{\partial E}{\partial t} + iD\frac{\partial^2 E}{\partial t^2} + f(E), \tag{4.17}$$

where gain terms are now included as the function $f(E)$. Euler time-stepping of the full equations is used in the predictor step and estimates the propagated electric field as

$$E_n^{pred} = E_n^m + \Delta x\left[\frac{E_{n+1}^m - E_{n-1}^m}{2v_g\Delta t} + \frac{iD}{\Delta t^2}(E_{n+1}^m - 2E_n^m + E_{n-1}^m) + f(E_n^m)\right]. \tag{4.18}$$

Substituting E_n^{pred} into the backward Euler time-stepping scheme yields

$$E_n^{m+1} = E_n^m + \Delta x\left[\frac{E_{n+1}^{pred} - E_{n-1}^{pred}}{2v_g\Delta t} + \frac{iD}{\Delta t^2}(E_{n+1}^{pred} - 2E_n^{pred} + E_{n-1}^{pred}) + f(E_n^m)\right]. \tag{4.19}$$

This numerical scheme is stable without constraints on the discretized steps of Δx and Δt, as shown in Fig. 4.3. Separate stability analysis of the forward and backward Euler methods baed on Von Neumann analysis has been discussed previously. Full stability analysis would require the specific gain terms. The equation with both propagation and dispersion is evaluated with the predictor-corrector scheme along the characteristic of $\frac{\Delta x}{\Delta t} = v_g$, and is compared to the case in which the identical equation is evaluated by the spectral method FFT [84]. The consistency shows the reliability of this predictor-corrector scheme. Note that the predictor-corrector scheme works with non-periodic boundary conditions, while the spectral schemes are only capable of dealing with specific types of boundary conditions. For modeling of diode lasers, the boundary conditions do not allow us to use spectral methods.

This time-stepping scheme gives a robust numerical implementation for the full wave equation including the gain term, propagation and dispersion. However, the algorithm also forces one to evaluate the gain term two time per numerical step: once for the prediction

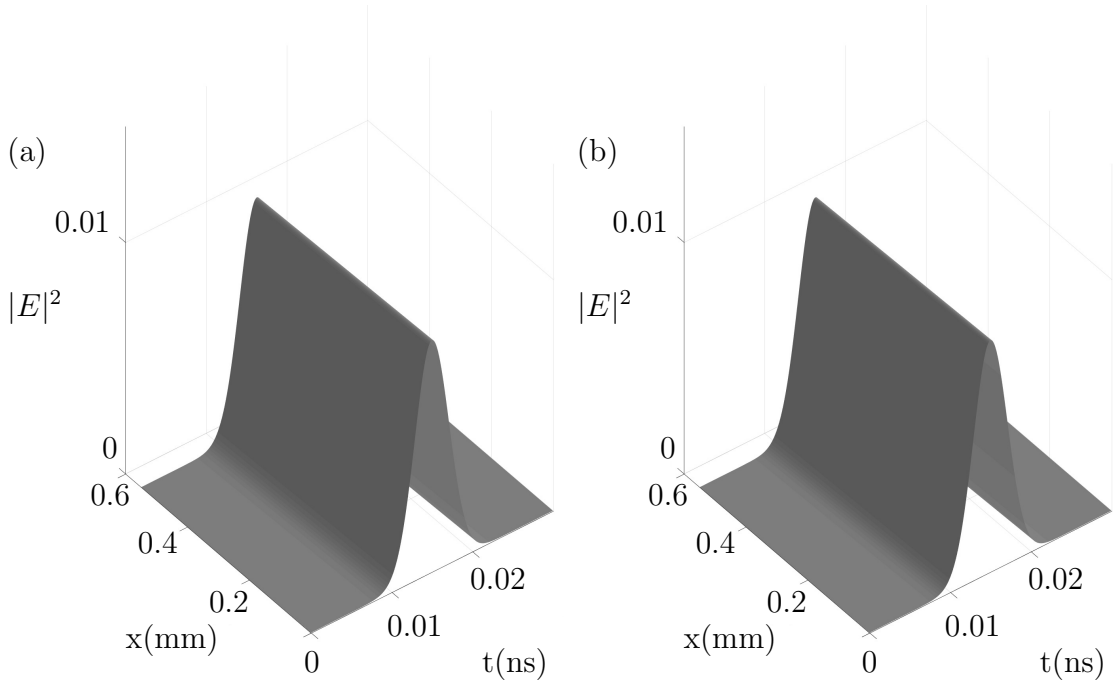

Figure 4.3: Numerical results of the wave equation with propagation and dispersion. (a) Predictor-corrector efficiently prevents the solution from explosion without constraints on the size of discretization. (b) Numerical simulation using FFT shows consistency with the predictor corrector scheme.

step, and once for the corrector step. But the evaluation of the semiconductor gain dynamics is extremely expensive and time-consuming [25, 50, 42]. We will use operator splitting techniques to reduce evaluation of the gain dynamics to once per time step.

4.3.5 Operator splitting techniques

Linearly coupled physical effects can be decoupled from each other, thus the partial differential equation of propagating, dispersion and complex gain terms can be discretized separately [84]. We asusme the wave propagation and dispersion act approximately independently of the gain over short time steps, and vice versa for the gain. By defining the gain term to be $f(E)$, we can consequently split the equation into two pieces as below:

$$\frac{\partial E}{\partial x} = \frac{1}{v_g}\frac{\partial E}{\partial t} + iD\frac{\partial^2 E}{\partial t^2}, \tag{4.20}$$

and

$$\frac{\partial E}{\partial x} = f(E). \tag{4.21}$$

The first equation is on the stability boundary of the leap-frog (2,2) scheme, while the second equation can be stably solved with Euler time stepping as already demonstrated in previous work [25, 50, 42]. This numerical scheme with the operator-splitting technique is stable and efficient for solving the full wave equation with all terms included. Note that leap-frog (2,2) is only capable of pushing g to the stability boundary of $|g| = 1$ with $M^2 \leq 4$ satisfied as shown in Eq. (4.14), while $|g| < 1$ can be satisfied without constraints using the backward Euler scheme. A new time stepping method making use of both operator-splitting techniques and predictor-corrector is preferable. Specifically, we make use of the Euler method for the propagation of the gain term while applying the predictor-corrector to the propagation and chromatic dispersion terms:

$$E_n^{pred} = E_n^m + \frac{\Delta x(E_{n+1}^m - E_{n-1}^m)}{2v_g\Delta t} + \frac{iD\Delta x}{\Delta t^2}(E_{n+1}^m - 2E_n^m + E_{n-1}^m), \tag{4.22}$$

and

$$E_n^{m+1} = E_n^m + \frac{\Delta x}{2v_g\Delta t}(E_{n+1}^{pred} - E_{n-1}^{pred}) + \frac{iD\Delta x}{\Delta t^2}(E_{n+1}^{pred} - 2E_n^{pred} + E_{n-1}^{pred}). \tag{4.23}$$

By combing predictor-corrector and operator-splitting, we are capable of evaluating the gain term more effectively (at half the computational cost) while maintaining stability of the entire numerical scheme.

4.4 Numerical scheme for the laser cavity

To stably and efficiently incorporate the dispersion, wave propagation and gain into the numerical scheme, we employ the advocated combination of predictor-corrector and operator splitting methods. To write Eq. (4.1) more compactly, the semiconductor dynamics are grouped into f_p and f_b:

$$\begin{aligned} f_p(E^+, E^-) = &-(\alpha_s + i\beta_s)(|E^+|^2 + 2|E^-|^2)E^+ \\ &-i\frac{\omega_0}{2c\eta\epsilon_0}\Gamma_{yz}P^+ - \frac{\alpha}{2}E^+ + S^+_{sp}, \end{aligned} \tag{4.24}$$

$$\begin{aligned} f_b(E^+, E^-) = &-(\alpha_s + i\beta_s)(|E^-|^2 + 2|E^+|^2)E^- \\ &-i\frac{\omega_0}{2c\eta\epsilon_0}\Gamma_{yz}P^- - \frac{\alpha}{2}E^- + S^-_{sp}. \end{aligned} \tag{4.25}$$

Making these substitutions into the governing equations and rearranging we construct our system of equations

$$\frac{\partial E^+}{\partial x} = -\frac{1}{v_g}\frac{\partial E^+}{\partial t} - i\frac{k''}{2}\frac{\partial^2 E^+}{\partial t^2} + f_p(E^+, E^-), \tag{4.26}$$

$$-\frac{\partial E^-}{\partial x} = -\frac{1}{v_g}\frac{\partial E^-}{\partial t} - i\frac{k''}{2}\frac{\partial^2 E^-}{\partial t^2} + f_b(E^+, E^-). \tag{4.27}$$

4.4.1 Operator-splitting technique and predictor-corrector scheme

We separate the dispersion and propagation from the gain dynamics so that the it can be discretized using a simple forward Euler scheme. Thus we can propagate along the x direction

$$E^+_{m+1,n} = E^+_{m,n} + \Delta x f_p(E^+_{m,n}, E^-_{m,n}), \tag{4.28}$$

$$E^-_{m+1,n} = E^-_{m,n} - \Delta x f_b(E^+_{m,n}, E^-_{m,n}). \tag{4.29}$$

We now consider the remaining terms in the governing equation which include the propagation and dispersion,

$$\frac{\partial E^+}{\partial x} = -\frac{1}{v_g}\frac{\partial E^+}{\partial t} - i\frac{k''}{2}\frac{\partial^2 E^+}{\partial t^2}, \tag{4.30}$$

$$-\frac{\partial E^-}{\partial x} = -\frac{1}{v_g}\frac{\partial E^-}{\partial t} - i\frac{k''}{2}\frac{\partial^2 E^-}{\partial t^2}. \tag{4.31}$$

Leap-frog (2,2) is used as the predictor step:

$$\frac{E^+_{m+1,n} - E^+_{m-1,n}}{2\Delta x} = -\frac{1}{2v_g\Delta t}(E^+_{m,n+1} - E^+_{m,n-1}) + \frac{iD}{\Delta t^2}(E^+_{m,n+1} - 2E^+_{m,n} + E^+_{m,n-1}), \tag{4.32}$$

$$\frac{E^-_{m-1,n} - E^-_{m+1,n}}{2\Delta x} = -\frac{1}{2v_g\Delta t}(E^-_{m,n+1} - E^-_{m,n-1}) + \frac{iD}{\Delta t^2}(E^-_{m,n+1} - 2E^-_{m,n} + E^-_{m,n-1}), \tag{4.33}$$

from which we obtain the predicted $E^{\pm}$ as

$$E^+_{pre,n} = E^+_{m-1,n} + \frac{\Delta x}{v_g\Delta t}(E^+_{m,n-1} - E^+_{m,n+1}) + \frac{2iD\Delta x}{\Delta t^2}(E^+_{m,n+1} - 2E^+_{m,n} + E^+_{m,n-1}), \tag{4.34}$$

$$E^-_{pre,n} = E^-_{m-1,n} - \frac{\Delta x}{v_g\Delta t}(E^-_{m,n-1} - E^-_{m,n+1}) - \frac{2iD\Delta x}{\Delta t^2}(E^-_{m,n+1} - 2E^-_{m,n} + E^-_{m,n-1}). \tag{4.35}$$

Substituting $E^+_{pre,n}$ and $E^-_{pre,n}$ into the backward Euler scheme shown in Eq. (4.7) we obtain

$$E^+_{m+1,n} = E^+_{m,n} + \frac{\Delta x}{2v_g\Delta t}(E^+_{pre,n-1} - E^+_{pre,n+1}) + \frac{iD\Delta x}{\Delta t^2}(E^+_{pre,n+1} - 2E^+_{pre,n} + E^+_{pre,n-1}), \tag{4.36}$$

$$E^-_{m+1,n} = E^-_{m,n} - \frac{\Delta x}{2v_g\Delta t}(E^-_{pre,n-1} - E^-_{pre,n+1}) - \frac{iD\Delta x}{\Delta t^2}(E^-_{pre,n+1} - 2E^-_{pre,n} + E^-_{pre,n-1}). \tag{4.37}$$

Note that for the last two time steps, $E^{\pm}_{m,n}$ and $E^{\pm}_{m,n-1}$ must both be saved. Further note that leap-frog (2,2) can be employed directly without the corrector step if the discretization sizes Δx and Δt are elaborately selected for $|g|$ to be on the stability boundary. But with the backward Euler stepping as a corrector, we are capable of achieving a more robust time-stepping algorithm without constraints on Δx and Δt.

4.4.2 Propagation along the direction of time

The algorithm presented in the previous section advanced the solution along the propagation direction x in increments of Δx. This follows the traditional time-stepping schemes of the nonlinear Schrödinger (NLS) based on a moving reference frame. Alternatively, one can discretize in both space and time, but advance the solution in t in increments of Δt. In this case, we re-arrange the governing equations as follows:

$$\frac{1}{v_g}\frac{\partial E^+}{\partial t} = -\frac{\partial E^+}{\partial x} - i\frac{k''}{2}\frac{\partial^2 E^+}{\partial t^2} + f_p(E^+, E^-), \tag{4.38}$$

$$\frac{1}{v_g}\frac{\partial E^-}{\partial t} = \frac{\partial E^-}{\partial x} - i\frac{k''}{2}\frac{\partial^2 E^-}{\partial t^2} + f_b(E^+, E^-). \tag{4.39}$$

We then can time-step by evaluating the electric field time derivatives along characteristics. This is equivalent to discretizing each time and spatial step so that $\frac{\Delta x}{\Delta t} = v_g$. This is highly stable for the traveling wave equations, allowing large time steps. Neglecting the dispersion term for the moment, and discretizing the rest of the equations we obtain

$$\frac{E^+_{j+1,n+1} - E^+_{j+1,n}}{\Delta t} = v_g(-\frac{E^+_{j+1,n} - E^+_{j,n}}{\Delta x} + f_p(E^+, E^-)), \tag{4.40}$$

$$\frac{E^-_{j,n+1} - E^-_{j,n}}{\Delta t} = v_g(\frac{E^-_{j+1,n} - E^-_{j,n}}{\Delta x} + f_b(E^+, E^-)). \tag{4.41}$$

The indices j and n, indicate spatial discretization and temporal discretization respectively. Note that the temporal discretization for the forward wave, E^+, is at spatial index j while the backward wave, E^- is at $j+1$. Rearranging the equations

$$E^+_{j+1,n+1} = E^+_{j,n} + \Delta x f_p(E^+, E^-), \tag{4.42}$$

$$E^-_{j,n+1} = E^-_{j+1,n} + \Delta x f_b(E^+, E^-). \tag{4.43}$$

To incorporate the dispersion term, we use a predictor-corrector method in the time-stepping approximation for the dispersion using a second-order accurate scheme,

$$\frac{\partial^2 E^\pm_{j,n}}{\partial t^2} = \frac{E^\pm_{j,n+1} - 2E^\pm_{j,n} + E^\pm_{j,n-1}}{\Delta t^2}. \tag{4.44}$$

The predictor step calculates $E^{\pm}$ without dispersion as

$$E^{+}_{j+1,pred} = E^{+}_{j,n} + \Delta x f_p(E^{+}_{j,n}, E^{-}_{j,n}), \tag{4.45}$$

$$E^{-}_{j,pred} = E^{-}_{j+1,n} + \Delta x f_b(E^{+}_{j+1,n}, E^{-}_{j+1,n}). \tag{4.46}$$

Then the corrector step calculates $E^{\pm}$ with dispersion, using the predicted values as

$$E^{+}_{j+1,n+1} = E^{+}_{j,n} - i\frac{k''\Delta x}{2}\frac{E^{+}_{j,pred} - 2E^{+}_{j,n} + E^{+}_{j,n-1}}{\Delta t^2} + \Delta x f_p(E^{+}_{j,n}, E^{-}_{j,n}), \tag{4.47}$$

$$E^{-}_{j,n+1} = E^{-}_{j+1,n} - i\frac{k''\Delta x}{2}\frac{E^{-}_{j+1,pred} - 2E^{-}_{j+1,n} + E^{-}_{j+1,n-1}}{\Delta t^2} + \Delta x f_b(E^{+}_{j+1,n}, E^{-}_{j+1,n}). \tag{4.48}$$

Note that in the last two time steps, it is also required that $E^{\pm}_{j,n-1}$ and $E^{\pm}_{j,n}$ must both be saved. This algorithm can be further accelerated when combined with the operator-splitting technique. Specifically, we can propagate the gain terms f_p and f_b separately using Euler stepping, whereas the chromatic dispersion and wave propagation are evaluated using the predictor-corrector. We can consequently obtain a second robust and efficient numerical method of the full wave equation.

Notice that this algorithm is capable of numerically evaluating the wave equations with unconventional boundary conditions. For example, the dynamics inside a cavity may require the reflecting boundary conditions

$$\begin{aligned} E^{+}_{0,n+1} &= -rE^{-}_{0,n}, \\ E^{-}_{L,n+1} &= -rE^{+}_{L,n}, \end{aligned} \tag{4.49}$$

where L is the left most spatial index, and r is the reflection coefficient. Other applications may have a filter at the boundary. A filter may be modeled by multiplying the electric field at the edge in frequency domain by a Lorentzian:

$$\tilde{E}^{-}(x = L, \omega) = r\tilde{E}^{+}(x = L, \omega)\mathbf{L}(\omega), \tag{4.50}$$

$$\mathbf{L}(\omega) = \frac{\Gamma}{i(\omega_0 - \omega) - \Gamma}. \tag{4.51}$$

The filter function is dimensionless and has a maximum of $\mathbf{L}(\omega = \omega_0) = 1$. Transforming this back into time domain, we find

$$E^-(x = L, t) = r\Gamma \int_{-\infty}^{t} dt' e^{i\omega_0(t-t')-\Gamma(t-t')} E^+(x = L, t'). \tag{4.52}$$

Spectral methods are not appropriate for implementing systems with these boundary conditions. For example, Fourier based methods require periodic boundary conditions while Chebychev polynomials require either Dirichlet or Neumann condition [84]. With a filter on one side of the cavity and a reflector on the other side we cannot use these fast spectral methods. In contrast, the standard finite difference discretization schemes requires no assumption on the boundary conditions. In this case, the boundary filter integral can be discretized in time and the resulting sum performed at each time step of the simulation [42].

4.5 Numerical Simulations

The numerical scheme is demonstrated by simulation of the model developed in Chapter 3, which characterizes the optical field evolution in a nonlinear dispersive cavity with counter propagating waves and complex gain dynamics for a quantum well based semiconductor laser [42].

Following Chapter 3 the governing equations are given

$$\begin{aligned} \pm\frac{\partial E_\pm}{\partial x} + \frac{1}{v_g}\frac{\partial E_\pm}{\partial t} + i\frac{k''}{2}\frac{\partial^2 E_\pm}{\partial t^2} = \\ -\frac{\alpha}{2}E_\pm - \left(\frac{\alpha_S}{2} + i\beta_S\right)(|E_\pm|^2 + 2|E_\mp|^2)E_\pm + S_{sp} + G_\pm(E_\pm), \end{aligned} \tag{4.53}$$

where α is the linear waveguide loss, k'' is the dispersion coefficient, α_S represents the two-photon absorption coefficient and β_S is Kerr nonlinear coefficient. Spontaneous emission term represented by S_{sp} is derived in the [42], and the complicated gains are combined as a function of $G_\pm(E_\pm)$. These field equations describing the cavity dynamics are combined with the carrier rate equations modeling the separate confinement heterostructure (SCH) and quantum well (QW), of which the complete form is shown in [42]. Briefly, the complicated carrier dynamics comprise a set of coupled partial differential equations characterizing the

electron and hole occupation probability of SCH and QW, which result in high computational expenses solving numerically.

As stated in Chapter 3, implementation of this model developed [42] on materials with higher central emission frequency requires including multiple waveguides for enhancing nonlinear pulse shaping and mode-locking [152]. By coupling out low-intensity components to the neighboring waveguides, we can effectively shape the electric field propagating in the first waveguide and achieve highly performed mode-locked pulses in the laser cavity [114, 89, 22]. For nearest neighbor coupling, the equations describing the waveguide array mode-locking are given by

$$\begin{aligned}\pm\frac{\partial E_{\pm}^{1}}{\partial x}+\frac{1}{v_g}\frac{\partial E_{\pm}^{1}}{\partial t}+i\frac{k''}{2}\frac{\partial^2 E_{\pm}^{1}}{\partial t^2}=\\ -\frac{\alpha}{2}E_{\pm}^{1}-\left(\frac{\alpha_S}{2}+i\beta_S\right)(|E_{\pm}^{1}|^2+2|E_{\mp}^{1}|^2)E_{\pm}^{1}+S_{sp}+G_{\pm}^{1}+iCE_{\pm}^{2},\end{aligned} \tag{4.54}$$

$$\begin{aligned}\pm\frac{\partial E_{\pm}^{2}}{\partial x}+\frac{1}{v_g}\frac{\partial E_{\pm}^{2}}{\partial t}+i\frac{k''}{2}\frac{\partial^2 E_{\pm}^{2}}{\partial t^2}=\\ -\frac{\alpha}{2}E_{\pm}^{2}-\left(\frac{\alpha_S}{2}+i\beta_S\right)(|E_{\pm}^{2}|^2+2|E_{\mp}^{2}|^2)E_{\pm}^{2}+S_{sp}+G_{\pm}^{2}+iC(E_{\pm}^{1}+E_{\pm}^{3}),\end{aligned} \tag{4.55}$$

$$\begin{aligned}\pm\frac{\partial E_{\pm}^{3}}{\partial x}+\frac{1}{v_g}\frac{\partial E_{\pm}^{3}}{\partial t}+i\frac{k''}{2}\frac{\partial^2 E_{\pm}^{3}}{\partial t^2}=\\ -\frac{\alpha}{2}E_{\pm}^{3}-\left(\frac{\alpha_S}{2}+i\beta_S\right)(|E_{\pm}^{3}|^2+2|E_{\mp}^{3}|^2)E_{\pm}^{3}+S_{sp}+G_{\pm}^{3}+iCE_{\pm}^{2}.\end{aligned} \tag{4.56}$$

Here the dimensionless coupling factor C is determined by the design parameters and spacing of the waveguide array. Thus it can be easily adjusted via designing the waveguide array to realize optimal mode-locking of the output.

With both propagating and counter propagating waves in the cavity, as well as the existence of chromatic dispersion and complex gain dynamics, we consider using the predictor-corrector scheme with transmission and reflection at the boundary and propagate in the direction of time. For our simulation, we use material parameters of GaAs for a higher central transition energy, the full material parameters are listed in table 3.1 in Chapter 3.

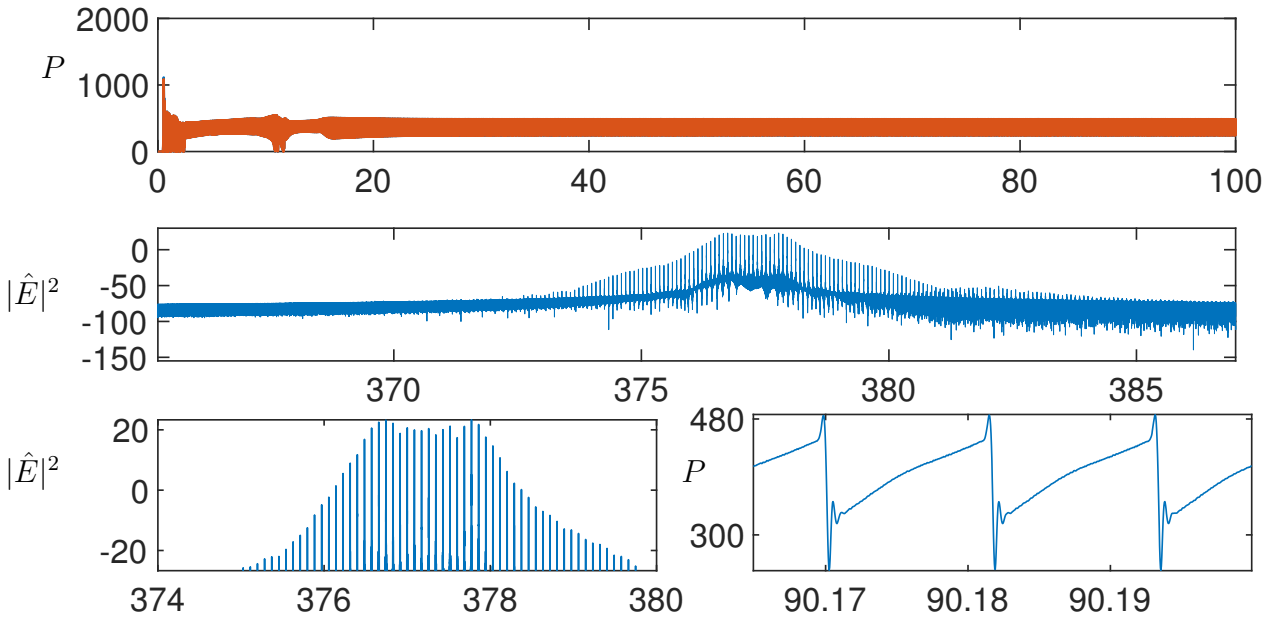

Figure 4.4: Evolution of output power P (mW) and power spectral density $|\hat{E}|^2$ (dBm/Hz) of the full propagating model evaluated with the predictor corrector scheme. (a) (b) The temporal output and the power spectral density of the temporal output in log scale of the first waveguide at I_{1in}=100 mA with the coupling factor C=1. (c) (d) The zoomed power spectral density and temporal output of the first waveguide. The predictor corrector scheme shows robust stability numerically with $\Delta t = 30fs$.

To numerically demonstrate the stability of the predictor-corrector scheme developed in Sec. 4.4, the waveguide array governing equations are simulated over a large number of round trips in the cavity. The propagating and counter propagating waves in the first waveguide stably evolve as shown in Fig. 4.4. Here we use the method of characteristics with $\Delta x/\Delta t = v_g$, and $\Delta t = 30fs$. The output power and spectral density show a repeatable waveform and broad spectral lines consistent with a mode-locked state over a long simulation time. Moreover, the predictor-corrector scheme shows robust stability compared to other methods with both wave propagation and chromatic dispersion included. It can become unstable if the time step is taken to be too large as shown in Fig. 4.5, where the time step size is increased from $30fs$ to $50fs$ in the simulation. The predictor-corrector scheme is unstable with increased stepping size and generates numerical blowup quickly at around $t = 0.5ns$.

4.6 Conclusion

In this chapter, we have explored the stability of a number of numerical time-stepping schemes including Euler stepping, backward Euler, leap frog (2,2), predictor-corrector, and two new numerical schemes that integrate predictor-corrector and operator-splitting strategies. Given the diversity of physics for our models of interest, including nonlinear dispersive wave equations with counter propagating waves and complex gain dynamics (semiconductor physics), these new schemes provide viable strategies that are not only stable, but computationally efficient when evaluating the semiconductor physics. The predictor-corrector scheme shows reliable stability with a properly chosen step size. Operator splitting allows us to maintain stability and reduce expensive computation of the gain model. The combination of the operator-splitting scheme with the predictor-corrector provides both stability and efficiency.

We have numerically validated the reliability of the predictor-corrector scheme with operator-splitting by applying it to the model developed in Chapter 3, which is a comprehensive traveling wave model for a quantum well and the mode-coupling in a waveguide array. The propagating and counter propagating waves are stably evolved by the predictor-

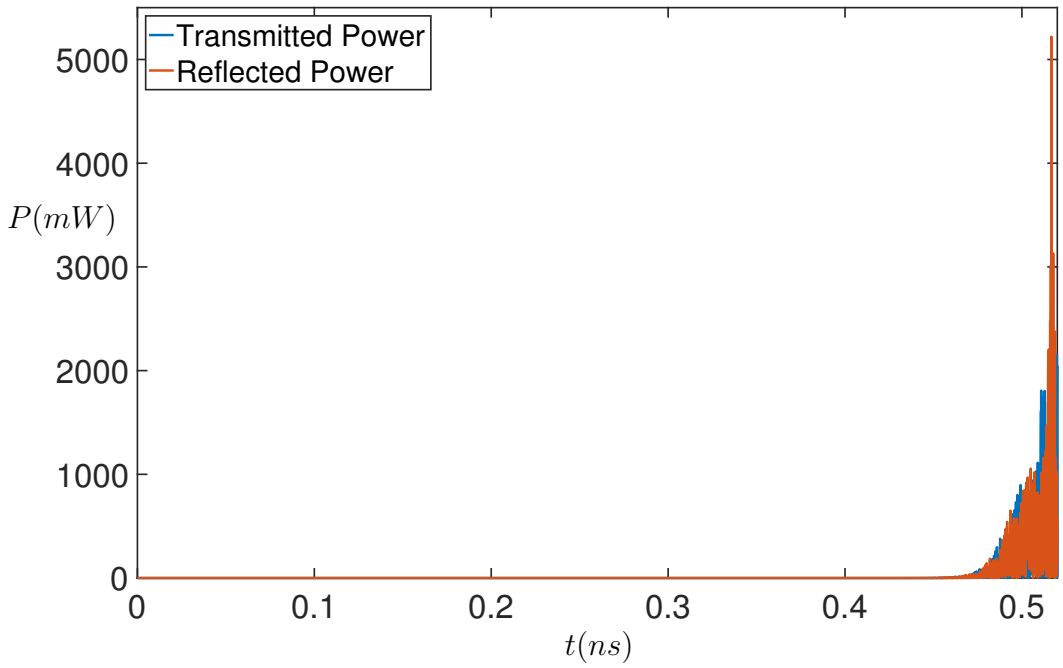

Figure 4.5: Evolution of output power P (mW) of the full propagating model in the first waveguide evaluated with the predictor corrector scheme. Discretized time step is set to be $\Delta t = 50fs$ while all the other parameters maintain the same as previously. The numerical solution becomes unstable with an increased time step size and eventually explodes at around $t = 0.5ns$.

corrector scheme with time stepping size near $\Delta t = 30fs$. For larger step sizes, the stability of the predictor-corrector is compromised. Thus much like a CFL requirement, our proposed method requires a sufficiently small stepping size to balance and ensure stability of the scheme. Regardless, the stable numerical results characterize the generation of frequency combs in the coupled waveguide array diode laser. The predictor-corrector scheme along with the operator-splitting can be broadly applied to more complicated wave propagation models.

Chapter 5

DEEP REINFORCEMENT LEARNING FOR SELF-TUNING MODE-LOCKED LASERS

In this chapter[1], we develop a self-tuning control strategy with deep reinforcement learning (deep RL) to obtain high-energy, single-pulse state in a passive mode-locked fiber laser. Deep RL integrates the two leading machine learning architectures of deep neural networks and reinforcement learning to produce robust and stable learning for control. A multi-parameter deep RL control algorithm is developed and applied to a nonlinear polarization rotation (NPR) based laser, with waveplate and polarizer orientations as controllers to achieve a global optimal performance of mode-locking. Via interactions with the environment, the deep RL controller allows the mode-locked fiber laser to recognize bi-stable structures and navigate, via trajectory planning, to optimally performing solutions and maximize the immediate or delayed rewards. We further integrate transfer learning to help the deep RL agent rapidly learn new parameter regimes and generalize its control authority. Additionally, the deep RL learning can be easily integrated with other control paradigms to provide a broad framework to control any optical system.

5.1 Introduction

Machine learning and artificial intelligence have grown rapidly in recent decades, transforming landscapes of science, technology and lifestyles. For control applications, a variety of ML strategies have been developed for stabilizing optical systems such as mode-locked lasers [17, 47, 87]. From genetic algorithms to deep neural networks, these studies provide a broad perspective on how a diverse set of optimization algorithms can be used to automate the

[1]Content of this chapter is published in journal article [136].

control and self-tuning of a given optical device. However, as a rapidly growing branch of machine learning, reinforcement learning (RL) has been rarely applied for controls in optical systems. RL algorithms are goal-oriented strategies based upon the trial-and-error search. An RL agent learns from interactions with the environment and takes actions adaptively with goal-oriented objectives. Recent works on games like chess and Go [128] have demonstrate the efficacy of RL algorithms combined with deep neural networks, i.e. the deep RL algorithms. Given its leading status as a control and goal-oriented strategy, we show that deep RL can be integrated with the mode-locked lasers to produce an architecture for intelligent and stable self-tuning operation. In this chapter, we show that the deep RL agent can search for the highest-energy mode-locked pulse in the high-dimensional space generated by the waveplates and polarizer, and stabilize a mode-locked laser in a robust manner. More than that, it can learn pathways to circumvent regions in parameter space where bi-stabilities exist. The delayed reward structure of the RL agent allows the system to learn how to maneuver around bi-stabilities in order to achieve optimal mode-locking performance. Furthermore, we demonstrate that transfer learning enables the deep RL controller to adapt rapidly when the interactive environment varies. The schematic of the self-tuning fiber laser built with the deep RL algorithm is shown in Fig. 5.1, with details of the optical system and the deep RL controller provided in the following sections of this chapter.

5.2 Background: reinforcement learning

As noted earlier, the power of RL lies in its ability to learn from interactions with the environment with goal-oriented objectives. This is unlike the two other dominant ML paradigms of supervised and unsupervised learning [18, 52]. Balancing between exploration and exploitation, an RL agent learns to sense the state of its environment and perform actions accordingly to proceed into the next state, with positive or negative rewards earned for learning. Importantly, the RL agent is capable of learning delayed rewards, which is critical for many optical systems since a trajectory to the optimal solution must be learned. This is equivalent to mapping out a set of moves, or long term strategy, to win a chess game. RL

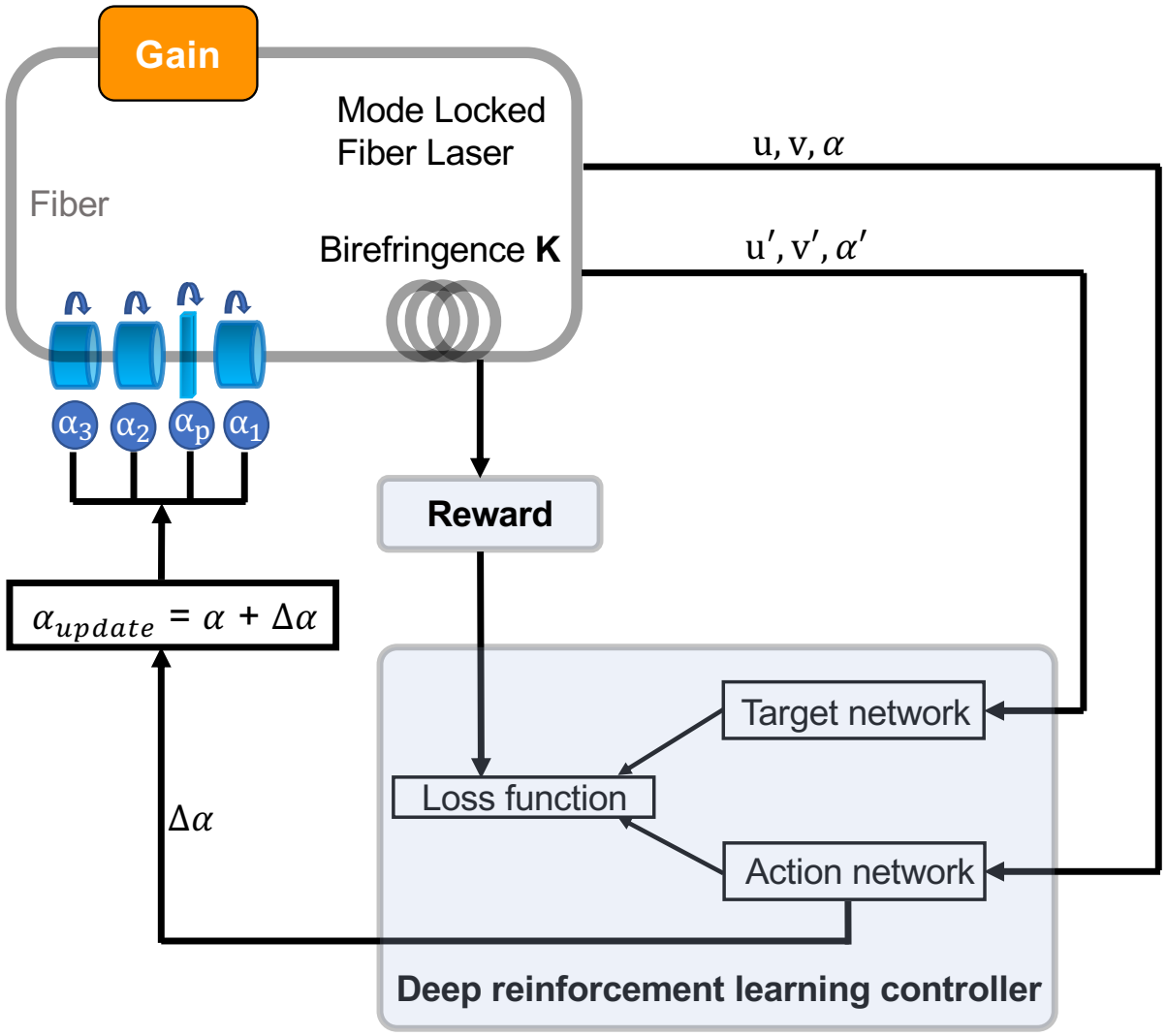

Figure 5.1: Schematic of the self-tuning fiber laser. The mode-locked fiber laser, including the laser cavity and optical components, is discussed in details in Section 5.3.1. The deep reinforcement learning controller is discussed in Section 5.3.2.

targets optimal policies for reinforcement learners to maximize the total reward across an episode. Each state follows a Markov property by assumption, i.e., each state is determined only by the previous state and the transition taken to the current state. Thus a large number of trials must be evaluated in order to determine an optimal policy. This is accomplished in chess and Go by self-play [128], which is exactly what the mode-locked laser is allowed to do to learn an optimal policy.

5.2.1 Q learning

We leverage deep Q-learning, specifically the deep off-policy temporal difference control algorithm [147, 106], which approximates the current estimations based on the previously learned estimations. In reinforcement learning algorithms, the state-action value function, or Q function, is defined as the expected discounted return of rewards starting from the state s with the action a according to policy π. The Q function specifies the agent's performance taking a particular action and transit from the current state to the next with the policy we choose. During training the reinforcement learning agent learns and converges to the optimal policy that maximizes the total reward across an episode.

Q-learning [146] is a particular approach to learn optimal actions in such sequential decision problems and has been recognized as a form of temporal difference learning [139]. Suppose we take action a in the current state s and arrive at state s', Q learning obtains

$$Q(s,a) = r(s,a) + \gamma max_{a'} Q(s',a'), \tag{5.1}$$

where $r(s,a)$ is the reward collected performing action a to move from state s to s', $\gamma \in [0,1]$ is the discount factor that controls the contribution of the rewards collected in the future to the total reward after the episode is finished. During an episode, the agent proceeds by either choosing the action with the highest Q value (exploitation), or selecting randomly an action to explore other possible states which may return higher delayed rewards (exploration). The agent moves forward to the next state s' with the selected action a and collects the associated reward r. Q-learning updates the current Q value of the experienced state-action pair with

the collected reward after transitioning to s' and the possible future rewards taking the optimal action thereafter:

$$Q(s,a) = Q(s,a) + \alpha(r + \gamma max_{a'} Q(s',a') - Q(s,a)), \tag{5.2}$$

where $\alpha \in [0,1]$ is the learning rate. Note that the difference between the actual reward $r + \gamma \max Q(s',a')$ and the expected reward $Q(s,a)$ is taken to update the value of $Q(s,a)$. The parameter α is important for convergence since it determines to what extent the current Q function is updated by the newly explored information. The Q function is arbitrarily initialized and updated following Eq. (5.2) until the Q-learning algorithm has converged.

5.2.2 Deep Q neural networks (DQN)

In discrete environments represented by a finite number of possible states and actions, we often search through all possible state-action pairs exhaustively to find the optimal $Q(s,a)$ values and the associated policy. However, this is computationally expensive and becomes infeasible with more than a small number of state-actions pairs. In continuous environments, it is impossible to list and search through each state with different actions. In contrast, deep Q learning [106] allows one to approximate the tabular Q function $Q(s,a)$ as a parameterized function $Q(s,a;\theta)$. Considering that neural networks can provide good approximations to possibly very complex functions, we utilize here deep neural networks as the estimator of the Q value function. In particular, $Q(s,a;\theta)$ is modeled as a multi-layered neural network with parameters θ that takes a given state s as input and yields a vector of values $Q(s,\cdot;\theta)$, each associated with a particular action a.

Following the Q-learning updating rule defined in Eq. (5.2), we refer to $r+\gamma \max Q(s',a';\theta)$ as the target value, $Q(s,a;\theta)$ as the predicted value, and the difference between the target and prediction is minimized when the current policy converges to the optimum. In deep Q learning, we can define analogously the loss function as the squared difference between the target and predicted value:

$$L = (r + \gamma \max_{a'} Q(s',a';\theta) - Q(s,a;\theta))^2. \tag{5.3}$$

The loss is minimized by learning updates to the deep neural network parameters θ that converge to the optimal policy. In summary, we use neural networks for the approximation of the Q function in deep Q learning, and converge to the optimal policy by minimizing the loss.

In particular, we employ as deep reinforcement learning agent an adaptation of the double deep Q neural network (DDQN) [57, 144] to the self-tuning laser control problem. The architecture of DDQNs is shown in Fig. 5.2, where the inputs fed into the action network describe the current state that the deep RL agent is in, and the output of the action network is the approximated Q function, specifically the Q values for all possible actions given the current state. Following the loss function defined in Eq. (5.3), we would observe strong divergence during training since the same neural network with parameters θ calculates both the predicted value and target value. To diminish the divergence, two separate networks are employed, one for selecting an action and the other for evaluating the selected action. Specifically, the target network with parameters θ' is used to calculate the target value, while the action network with parameters θ yields the predicted Q values associated with each action. The new loss function is defined as:

$$L = (r + \gamma \max_{a'} Q(s', a'; \theta') - Q(s, a; \theta))^2, \tag{5.4}$$

where θ' and θ stand for the different set of parameters of the target network and the action network, respectively. The parameters of the target network are periodically frozen for several episode during training before being updated by copying the parameters from the action network, or partially updated with parameters from the action network in each episode to stabilize the training.

To stabilize the training and reduce the overfitting caused by correlation between the deep RL agent's experiences, we train the DDQN with an experience replay buffer [97], which is usually defined as a queue that saves a fixed number of the recent experiences. The experience $< s, a, r, s' >$ of the deep RL agent is defined as the concatenation of the current state s, the action selected a, the next state s' after performing the action, and

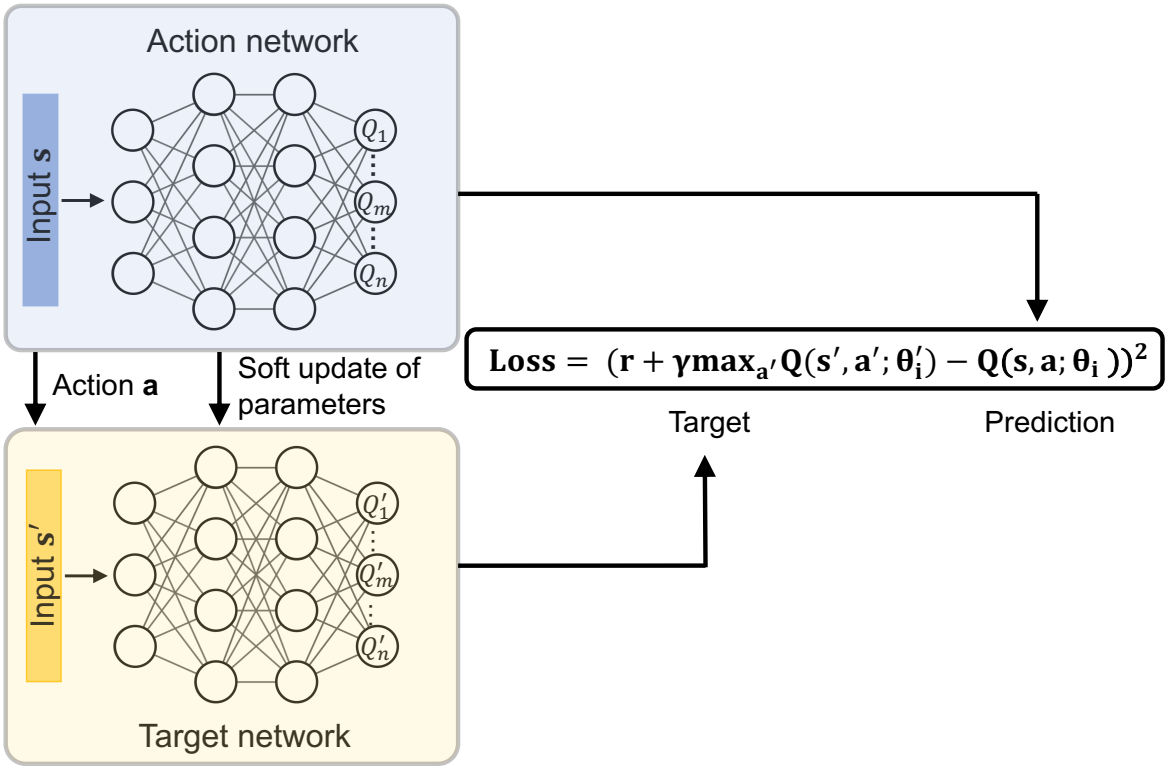

Figure 5.2: The architecture of the double deep Q neural network. A target network is included to stabilize the training. More details are discussed in Section 5.2.2.

the associated reward r received in this transition. During training, rather than directly train with the newest experiences collected, we sample a random batch of the experiences $< s, a, r, s' >$ from the replay buffer and feed the sampled batch to the neural network for parameter updates. The deep RL agent benefits from the replay buffers by learning from an enlarged range of random and less correlated experiences.

5.3 Deep reinforcement learning for self-tuning fiber lasers

5.3.1 Mode-locked fiber laser model

As noted earlier in Chapter 1, here our model of the laser cavity dynamics is a well-established computational model which treats the cavity in a component by component manner by separately applying the nonlinear optical propagation to the laser dynamics with discrete waveplates and polarizer in each round trip. This model produces a rich set of dynamics that we wish to control [130]. We model the propagation of intra-cavity fields with the coupled nonlinear Schrödinger equation with modifications to account for the bandwidth limited gain and cavity losses [40, 39, 82]:

$$i\frac{\partial u}{\partial x} + \frac{D}{2}\frac{\partial^2 u}{\partial t^2} - Ku + (|u|^2 + A|v|^2)u + Bv^2u^* = iRu, \tag{5.5a}$$

$$i\frac{\partial v}{\partial x} + \frac{D}{2}\frac{\partial^2 v}{\partial t^2} + Kv + (A|u|^2 + |v|^2)v + Bu^2v^* = iRv, \tag{5.5b}$$

where $u(x,t)$ and $v(x,t)$ are often referred to as the fast and slow components of the two intra-cavity electric field envelopes, which are orthogonally polarized. The propagation distance x is non-dimensionalized by the cavity length, and the dimensionless time t is normalized by the full width at half maximum of the pulse. D is the average group velocity dispersion, A and B, determined by physical properties of the laser fiber, are the nonlinear coupling parameters characterizing the cross-phase modulation and the four-wave mixing, respectively. Here we consider a silica fiber with $A = 2/3$ and $B = 1/3$. The fiber birefringence, quantified by K, represents a major disturbance to the laser dynamics due to its sensitivity to thermal fluctuations. The dissipative term R, characterizing the bandwidth-limited gain and

attenuation arising from the Yb-doped amplification, is defined as

$$R = \frac{2g_0(1+\tau\partial_t^2)}{1+(1/e_0)\int_{-\infty}^{\infty}(|u|^2+|v|^2)dt} - \Gamma, \tag{5.6}$$

where g_0 is the dimensionless pumping strength, and e_0 is the dimensionless saturation energy of the gain medium. The pump bandwidth is τ and losses caused by output coupling and fiber attenuation are characterized by Γ.

The effect of the waveplates and polarizer during each round trip is modeled by the discrete application of Jones matrices:

$$W_{\lambda/4} = \begin{bmatrix} e^{-i\pi/4} & 0 \\ 0 & e^{i\pi/4} \end{bmatrix}, \tag{7.1}$$

$$W_{\lambda/2} = \begin{bmatrix} -i & 0 \\ 0 & i \end{bmatrix}, W_p = \begin{bmatrix} 1 & 0 \\ 0 & 0 \end{bmatrix}. \tag{7.2}$$

Note that $W_{\lambda/4}$ characterizes the effects of quarter-waveplates α_1 and α_2, $W_{\lambda/2}$ is for the half-waveplate α_3, and W_p is for the polarizer α_p. An additional rotation matrix $R(\alpha)$ is necessary to account for the offset between the direction of the intra-cavity fast field and the principal axes of the waveplates and polarizer, and we define

$$J_j = R(\alpha_j)W_jR(-\alpha_j), \tag{8.1}$$

$$R(\alpha_j) = \begin{bmatrix} cos(\alpha_j) & -sin(\alpha_j) \\ sin(\alpha_j) & cos(\alpha_j) \end{bmatrix}, \tag{8.2}$$

where α_j $(j = 1, 2, 3, p)$ is a waveplate or polarizer angle. These rotation angles are easily manipulated via electronic control [126], and are considered as the control variables of the deep reinforcement learning agent for driving the laser dynamics to mode-locking here. Typical parameters used in these simulations are given in Table 5.1. The round-trip length is 1.5 dimensionless units. The non-dimensional scalings can be found in Refs. [40, 39, 82]. Such lasers typically produce pulse widths on the order of hundreds of femtoseconds with repetition rates in the tens of megahertz.

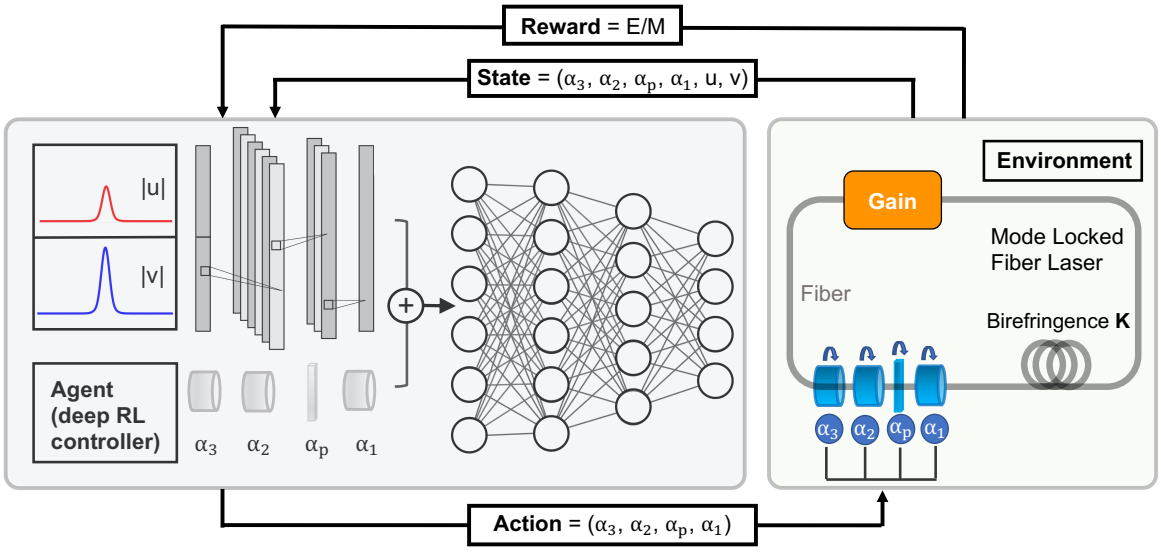

Figure 5.3: Schematic of the self-tuning mode-locked laser with deep reinforcement learning control. The input to the deep RL controller describes the current state that the controller is in, and is defined as the concatenated electric fields u, v and waveplate orientations α_1, α_2, α_3, α_p. The control inputs to the laser cavity are then updated by the selected action of the deep RL controller, which result in changes of the laser cavity dynamics and returns new electric fields u, v, and reward r as defined in Eq. (5.7) to the deep RL agent. Given the updated inputs and the associated reward r, the deep RL controller adjusts its strategy accordingly to select the next action and optimize the control inputs to the laser cavity.

Table 5.1: **CNLS simulation parameters**

τ	Γ	A	B	D	K	g_0	e_0	L_t	N_t
0.1	0.1	2/3	1/3	-0.4	0.1	1.73	4.23	60	256

5.3.2 Deep reinforcement learning control

A schematic of the self-tuning mode-locked laser with deep reinforcement learning control is shown in Fig. 5.3, highlighted with a deep RL controller and a mode locked fiber laser cavity of passive nonlinear polarization rotation (NPR). The mode-locking laser cavity, which is discussed in details in the previous section, is interpreted as the interactive environment in the reinforcement learning framework, and the waveplate angles $\alpha_1, \alpha_2, \alpha_3$ and polarizer angle α_p are considered as the controllable actions of the deep reinforcement learning agent. We take concatenated components of the electric fields u, v, and the current waveplate orientations $\alpha_1, \alpha_2, \alpha_3$ and α_p as the input to the deep reinforcement learning agent. Specifically, the deep reinforcement learning controller, built with TensorFlow 1.10.0, contains three alternatively stacked convolutional layers and max pooling layers, followed by six fully connected layers with leaky-ReLU as activation functions. The convolutional layers extract features from the input state by identifying the solitons inside the electric fields u and v, and the max pooling layers detect existence of the solitons and reduce the input dimensionality before feeding into the fully connected layers. Note that we demonstrate here the efficacy of the deep RL architecture in a numerical simulation of the laser cavity, but it is possible to train the deep RL controller directly in an experiment, as the controller only relies on information that is readily available in experiments.

The performance of the deep reinforcement learning controller is evaluated in terms of a reward r. In particular, we seek to steer the system to high-energy mode-locked states. However, the reward/cost landscape is very complex and exhibits many local optima. In

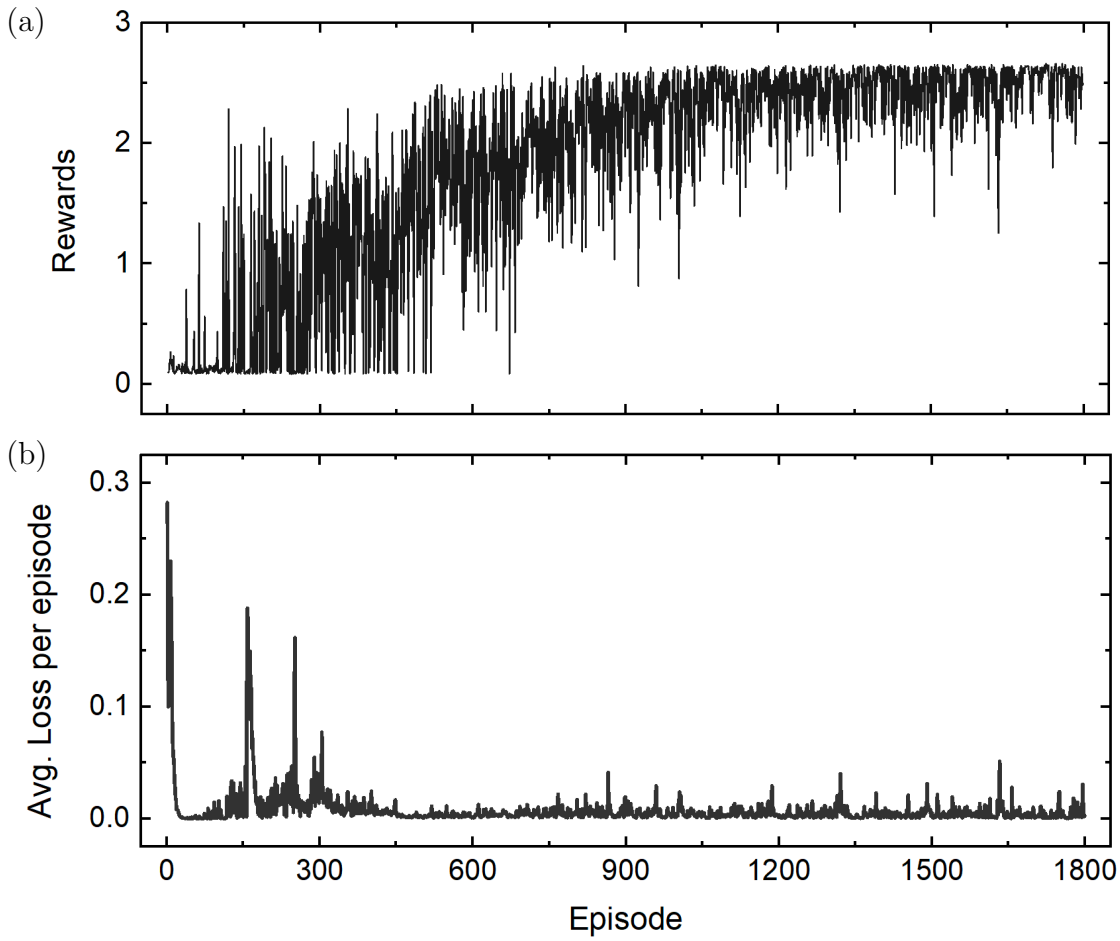

Figure 5.4: The variation of the rewards and loss function during training shows that the deep reinforcement learning controller adapts to improved policies as training proceeds.

addition, evaluating energy is not sufficient, as there are many chaotic solutions which have significantly higher energy than mode-locked states [16]. To define the reward r, we consider including the fourth-moment (kurtosis) M of the Fourier spectrum of the waveform, which is large for chaotic solutions but relatively small for the desired mode-locked states. To have a large reward r only for tightly confined temporal wave packets with relatively large energy, we define [16]

$$r = E/M. \tag{5.7}$$

To penalize the ineffective actions more efficiently during training, we rescale the reward to be centered around zero, so that the desired actions result in positive rewards while the ineffective ones return negative rewards. We rescale it back as defined in Eq. (5.7) after training for consistency and interpretability.

Our deep RL agent uses an ϵ-greedy policy to balance between exploration and exploitation, and parameters θ' of the target network are partially updated in each training step to improve stability. Note that the deep RL agent spans a large action space in the multiple-input single-output (MISO) case, when the three waveplates and polarizer orientations α_1, α_2, α_3, and α_p are considered as controllers. Thus we observe convergence difficulty in training the model directly with randomly initialized neural network parameters. To deal with this problem, we start training our deep RL agent with a single controller α_1, and gradually increase the number of controllers by initializing with previously trained parameters for the current model of increased number of controllers. Such parameter initialization strategy efficiently prevents the model from diverging, especially at the early stages of training.

The deep RL agent takes as input the electric fields and waveplate orientations, and the output yields Q values associated with all possible actions given the current state that the deep RL agent is in. Following the ϵ-greedy policy, our RL agent either randomly selects an action for exploration, or greedily selects the action with the highest Q value for exploitation and moves to the next state accordingly. Specifically, parameters α_1, α_2, α_3, and α_p are adjusted according to the action selected, and consequently we observe changes of electric fields u and v in the fiber laser cavity. The reward r of this transition, as defined in Eq. (5.7),

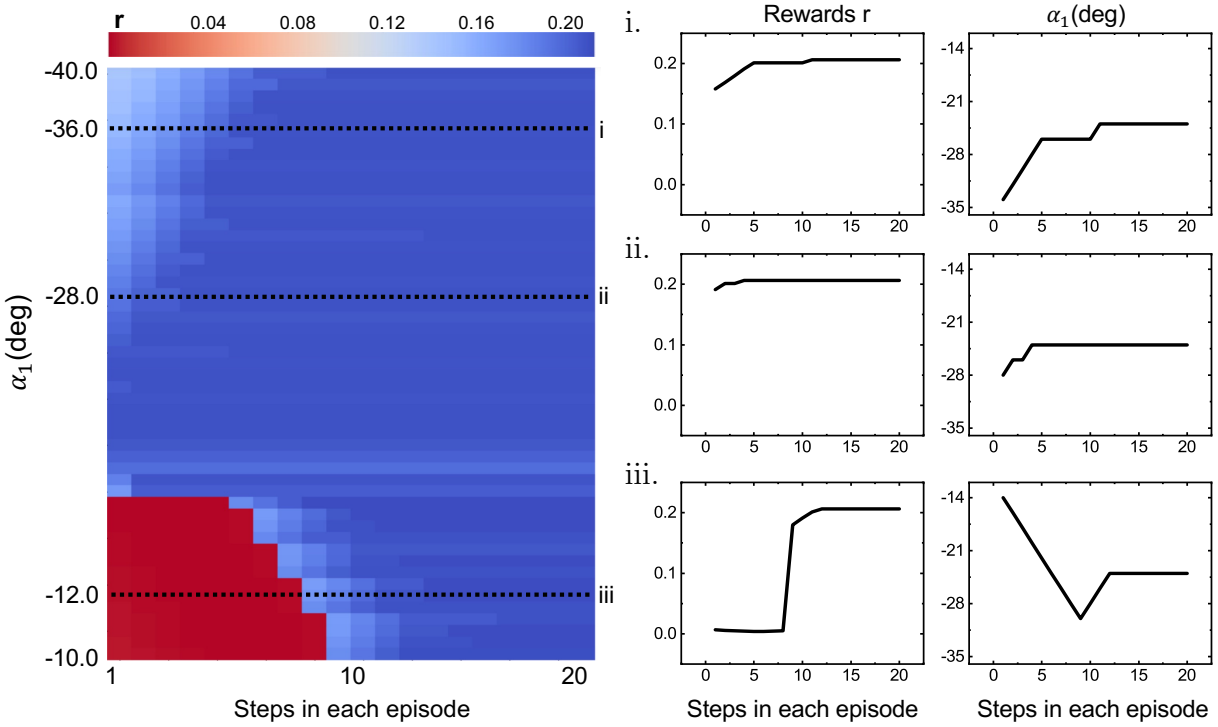

Figure 5.5: The deep reinforcement learning controller effectively drives the laser dynamics to mode-locked solutions with α_1 starting from $[-40°, -10°]$. Left panel demonstrates the change of rewards in each episode starting with different initial values of α_1. The deep reinforcement learning controller adaptively selects actions to continue with the current waveplate orientation, or increase/decrease α_1 by $2°$. Control results for experiments starting with $\alpha_1 = -36°$, $-28°$, and $-12°$ are shown in detail in figures (i)-(iii). Note that the intra-cavity electric fields u and v start as hyperbolic secant pulses in each experiment. Further note that the colormap (which contains a colorbar), used here and in future figures, denotes the reward value.

is taken of the new intra-cavity fields u and v after transition. The procedure is repeated until the completion of the entire episode, and then a new episode is started with the same initial conditions of the electric fields and waveplate/polarizer orientations to collect more samples. Thus, the deep RL agent learns from different trials using exploration and exploitation, and eventually converges to the optimal policy that leads to the highest total reward across the entire episode. Note that after the training stage, the learned policy of the deep RL agent is evaluated by greedily selecting the action with the highest Q value.

5.4 Performance of deep reinforcement learning control

In this section we demonstrate the efficacy of deep RL control in the mode-locked fiber lasers. We first demonstrate the deep RL strategy for a single-input control (α_1). The deep RL controller is then applied in a multi-input control to find the optimal orientation of the waveplates ($\alpha_1, \alpha_2, \alpha_3$) and polarizer ($\alpha_p$). Finally, the controller is generalized to find optimal solutions with varying values of the fiber birefringence, which is an unmeasured latent variable that dictates the performance of the laser cavity. RL is shown to be a robust and stable way to enact control.

5.4.1 Single-input control for fixed birefringence K

Figure 5.4 shows the variation of rewards and loss function during training process of the deep reinforcement learning controller for a single-input, single-output (SISO) case. The quarter-waveplate angle α_1 is the control variable, which can be varied in 2° steps. The search starts with an initial value of $\alpha_1 = 15°$, and all other angles are held fixed at pre-determined, locally maximizing values. The deep reinforcement learning agent takes an action from a state using epsilon-greedy policy and the exploration rate ϵ is exponentially decayed during training. We observe an increase of the total reward over a complete episode as the training proceeds, as shown in Fig. 5.4 (a). Note that the deep RL agent adapts to a new policy when the loss rises as shown in Fig. 5.4 (b).

Extending the initial values of α_1 from 15° during training enables us to train a model that drives the laser dynamics to mode-locking with different initial values of α_1, as shown in Fig. 5.5. With fixed birefringence parameter K, the deep reinforcement learning controller correctly interprets and extracts features from the input states, and takes the action to efficiently drive the laser dynamics to mode-locked solutions with α_1 starting from $[-40°, -10°]$. For example, with the initial value of $\alpha_1 = -12°$, the reward of each step continues increasing from the initial value as the deep RL controller drives the intra-cavity dynamics to mode-locking, as shown in Fig. 5.5 (iii). Interestingly, we observe hysteresis in the corresponding

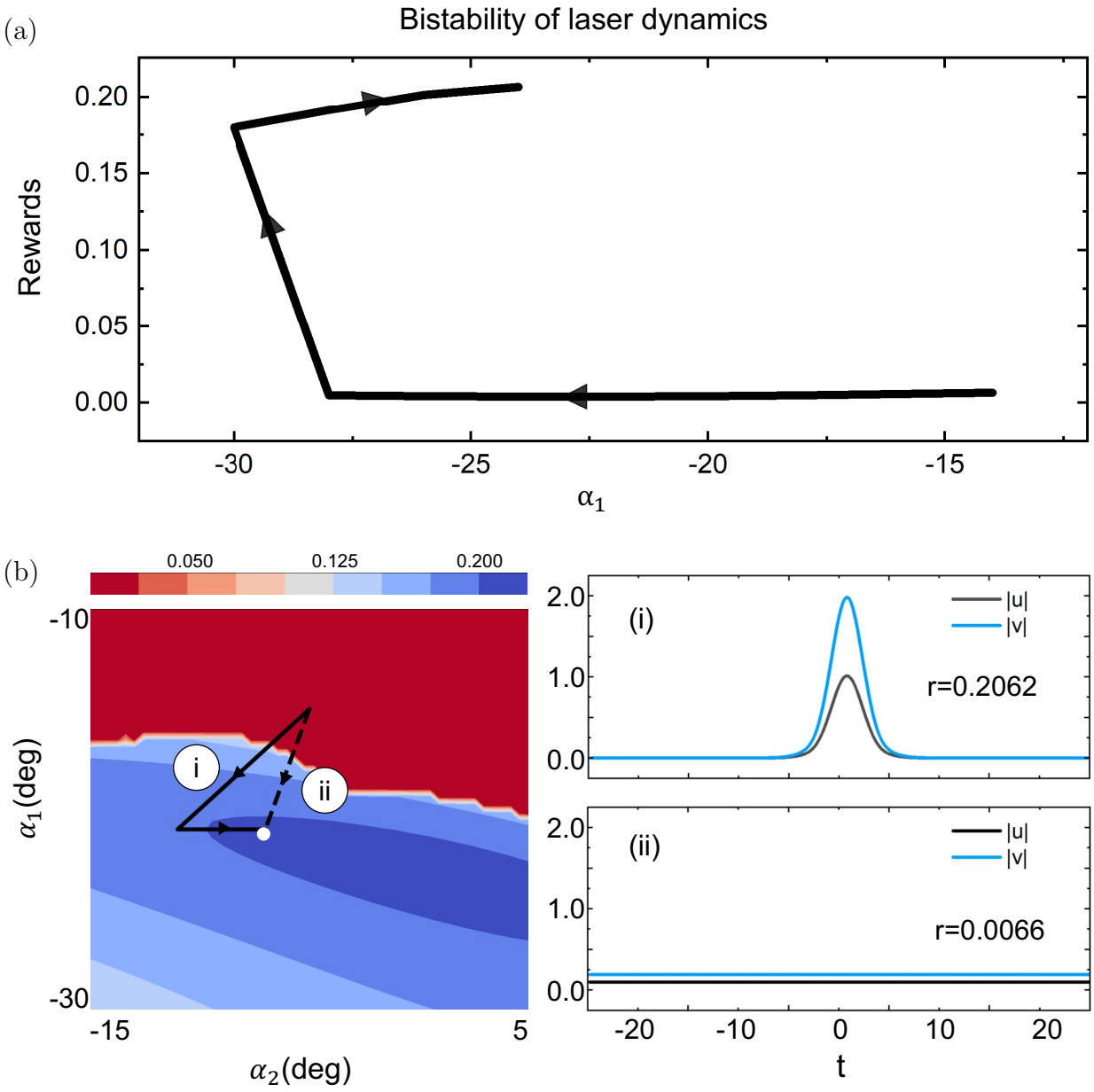

Figure 5.6: (a) The deep reinforcement learning controller for a single-input, single-output (SISO) case. The reward r rises from the initial value as the controller drives the intra-cavity dynamics to mode-locking and we observe hysteresis in the corresponding change of α_1 while the reward r is consistently increasing. (b) The deep reinforcement learning control for two controllers α_1 and α_2. Start with $\alpha_1 = -15°$ and $\alpha_2 = -3°$, the laser dynamics successfully arrives at the mode-locked solution with $r = 0.2062$ following the path (i) selected by the deep reinforcement learning controller, whereas we observe the plane wave solution ($r = 0.0066$) following path (ii) as comparison.

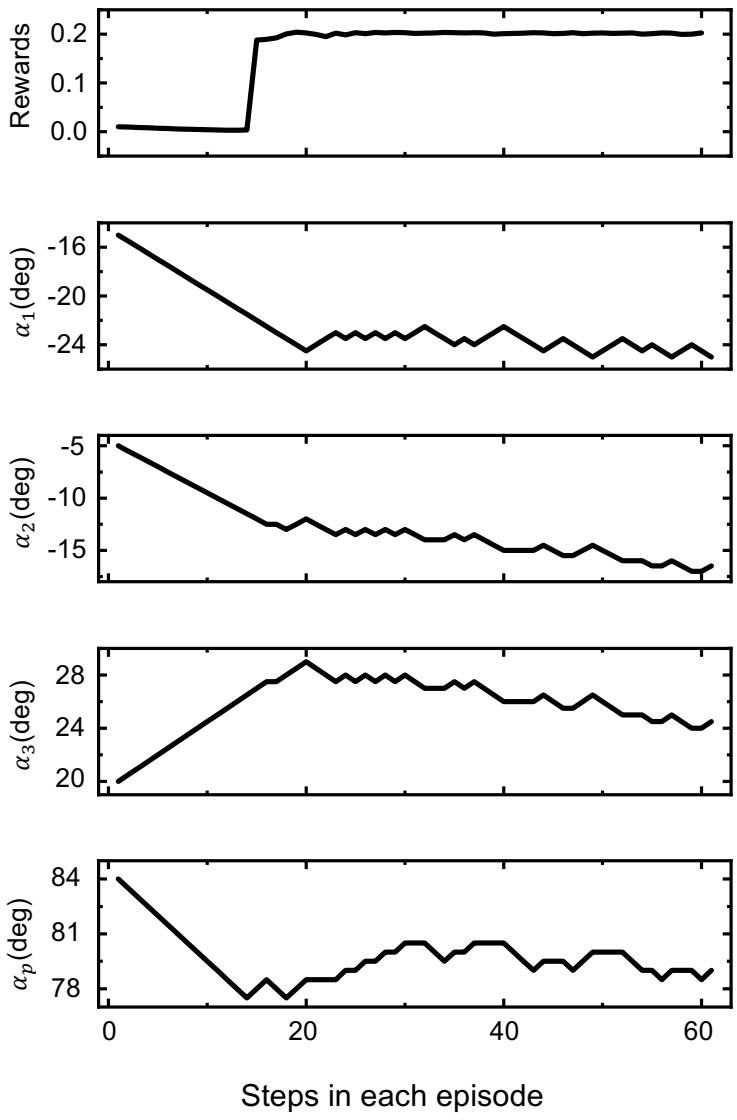

Figure 5.7: The deep reinforcement learning controller for the multiple-input, single-output (MISO) case where we are controlling all four waveplate orientations simultaneously ($K = 0$). The experiment starts with hyperbolic secant pulses u and v in cavity, which are promptly attenuated to constant waveforms with initial values of $\alpha_1 = 15°, \alpha_2 = -5°, \alpha_3 = 20°$, and $\alpha_p = 84°$. The four controllers α_1, α_2, α_3, and α_4 either hold on to the current orientations or increase/decrease by 0.5° in each step.

change of α_1 while the reward is consistently increasing, as shown in Fig. 5.6 (a). The deep reinforcement learning controller correctly identifies the bi-stability of the intra-cavity dynamics and arrives eventually at the globally maximizing solution in this case. No other ML architecture to date has been able to identify bistability. RL achieves this due to its deferred reward structure which allows it to plan a path around the instability. Figure 5.6 (b) describes the system bi-stability with two controllers α_1 and α_2. Our deep RL agent successfully discovers the path to drive the laser dynamics to mode-locking, marked as path (i) in Fig. 5.6 (b). The corresponding final states of the electric fields u and v are also pictured in Fig. 5.6 (b), with a high reward $r = 0.2062$. We compare this path selected by our deep RL agent to the direct connection of the start and end points, which is marked as path (ii) in Fig. 5.6 (b). The corresponding final states of the electric fields u and v are also pictured, of which we observe constant waveforms (plane waves) with $r = 0.0066$. Note that here we only extend the initial values of α_1 to be in the range of $[-40°, -10°]$ during training, but the deep RL agent has the ability to be generalized and further expanded to a larger range of initial values of α_1.

5.4.2 Multi-input control for fixed birefringence K

Figure 5.7 shows the deep reinforcement learning controller for the multiple-input, single-output (MISO) case where we control all four waveplate orientations simultaneously. This multi-input control is more complicated than the single-input case as the number of possible actions is significantly larger. Thus transfer learning is leveraged to prevent the model from diverging at the early stage of training. The number of controllers is gradually increased until the desired performance is achieved. The search starts with initial values of $\alpha_1 = 15°, \alpha_2 = -5°, \alpha_3 = 20°$, and $\alpha_p = 84°$. With fixed fiber birefringence, the deep reinforcement learning controller takes the correct actions to drive the laser dynamics from constant waveforms (plane waves) to the mode-locked solutions, as shown in Fig. 5.7. After the mode-locked state is achieved, the deep reinforcement learning agent continues searching through the action space with the reward oscillating near the optimal performance. Because the waveplate

orientations are varied simultaneously, the large action space results in a slow search for the deep RL agent, and we find it difficult to eliminate such oscillations. Other adaptive controllers, for example, extremum seeking control [16], can be combined to stabilize and attenuate such oscillations for better performance.

5.4.3 Multi-input control for varying birefringence K

We find the neural network parameters of the deep RL controller trained with birefringence $K = 0.1$ can be generalized to control the mode-locking dynamics at different values of K. Except for a few cases, the deep reinforcement learning controller successfully drives the laser dynamics to mode-locking with different values of birefringence K from -0.2 to 0.4, as shown in Fig. 5.8 (a). Note that in such generalized cases, the deep RL controller takes more steps on average to drive the laser dynamics to mode-locking, and in some cases the mode-locked solutions achieved are not tightly-confined as shown previously. Moreover, among a few cases, the deep reinforcement learning controller successfully achieves mode-locking but gradually wanders afterwards.

One feasible solution to improve the control performance in such cases is to retrain the model completely for different values of birefringence K. However, we find the neural network parameters of our deep RL agent adapt well and quickly with transfer learning [109] to different values of the birefringence K. In other words, there is no need to retrain the model completely with varying K, but instead we can slightly increase the exploration rate of the current model and collect more experiences by interacting with the new environment of changed birefringence K. These newly collected experiences enable the model to quickly update and adapt to the new environment. Thus it provides the possibility of building an online model for what is typically a stochastic and slowly-varying birefringence. In our experiments, training the neural network parameters with the birefringence $K = 0.1$ takes at least 2000 episodes for the deep RL controller to converge to the optimal policy, whereas the transfer learning takes only 300 episodes on average to adapt to environments with varying birefringence K. With fined-tuned parameters for $K \in \{-0.2, 0, 0.2, 0.4\}$, we improve the

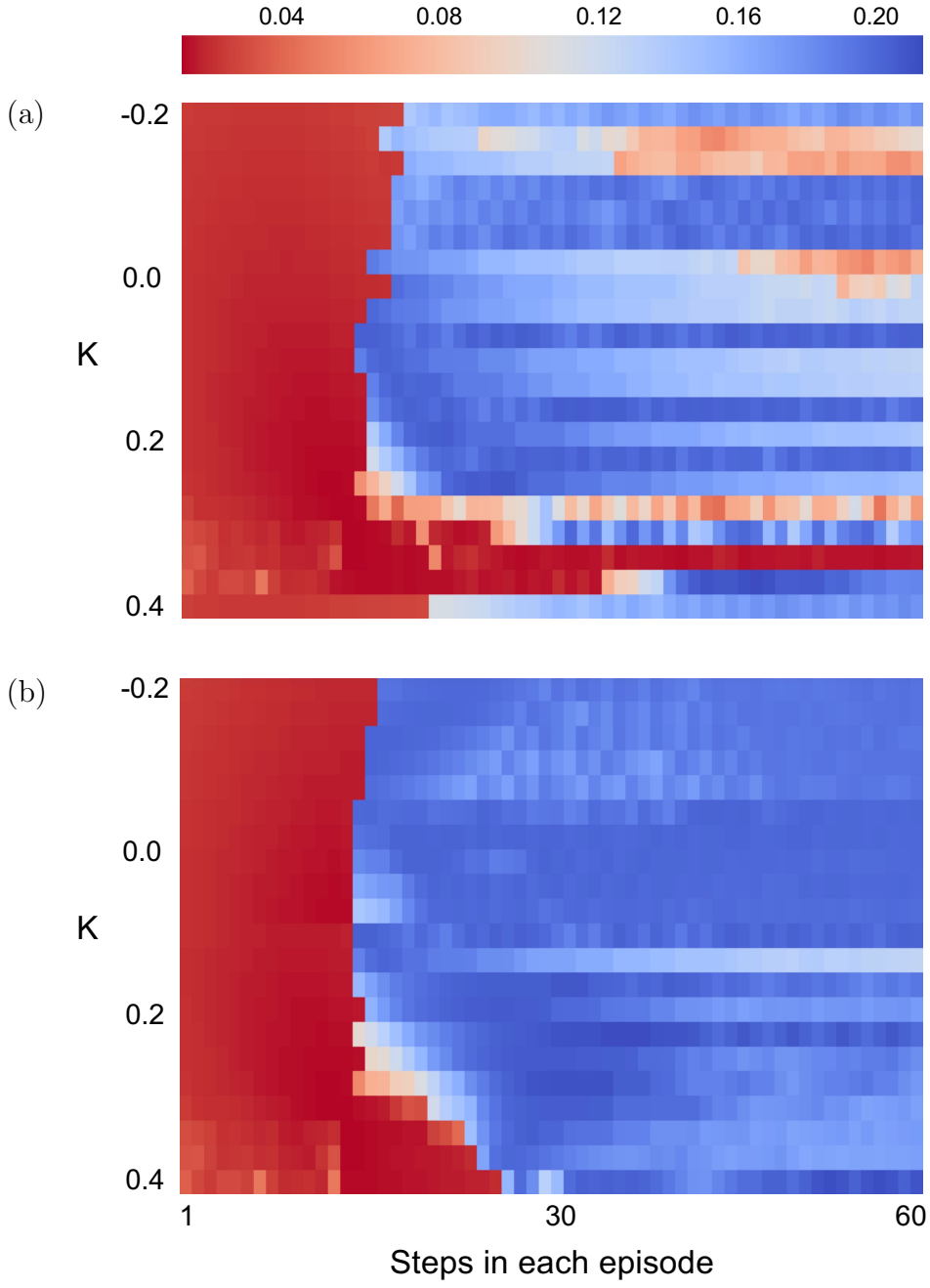

Figure 5.8: (a) Neural network parameters of the deep RL controller trained with birefringence $K = 0.1$ can be generalized to environments with different values of K. (b) With transfer learning, neural network parameters of the deep RL controller can be rapidly fine-tuned with a small amount of newly collected experiences and updated to control effectively in the new environments with different values of K.

performance of the deep reinforcement learning controller to drive the laser dynamics to mode-locking with other values of the birefringence K ranging from -0.2 to 0.4, as shown in Fig. 5.8 (b). Note only four sets of neural network parameters are used to generalize the controller to a range of K values.

As previously noted, we find in some cases that the deep RL controller successfully achieves mode-locking, but gradually walks apart from the desired solution. In such cases we can rely on extremum seeking controller [16] or other adaptive controllers for better performance. Extremum-seeking control, for example, is a form of perturb-and-observe control that estimates the gradient of an objective function by injecting an additional sinusoidal signal as input. The signal converges more rapidly when the objective function has a large gradient. Extremum-seeking control can lock the system to the local maximum and reacts rapidly to moderate changes of intra-cavity dynamics [83]. However, it relies on initial conditions of the parameters and state of the system since it only finds local maxima. Moreover, extremum-seeking control cannot recover in cases when the system is knocked far from the desired local maximum with drastic perturbations. Therefore, a combination of the deep RL agent with the extremum-seeking controller is a viable integrative strategy since it can evade the poor local maximum, and stabilize the intra-cavity dynamics around the mode-locked solution. To implement this integrated strategy, the deep RL controller is first executed in order to find a good mode-locked solution in a rapid manner. Indeed, deep RL can find near optimal stable mode-locking with several steps of propagation. The extremum-seeking controller is then turned on to stabilize the system. The schematic is shown in Fig. 5.9.

5.5 Conclusion

In this chapter we demonstrate a fast, reliable self-tuning controller for the passive mode-locked fiber laser with deep reinforcement learning. The controller varies all four waveplate orientations simultaneously to achieve a tightly-confined, high-energy mode-locked state. Interestingly, the control paths selected by the deep RL controller reflect the bi-stability of the laser dynamics, and demonstrate the efficacy of the deep RL control to correctly sense

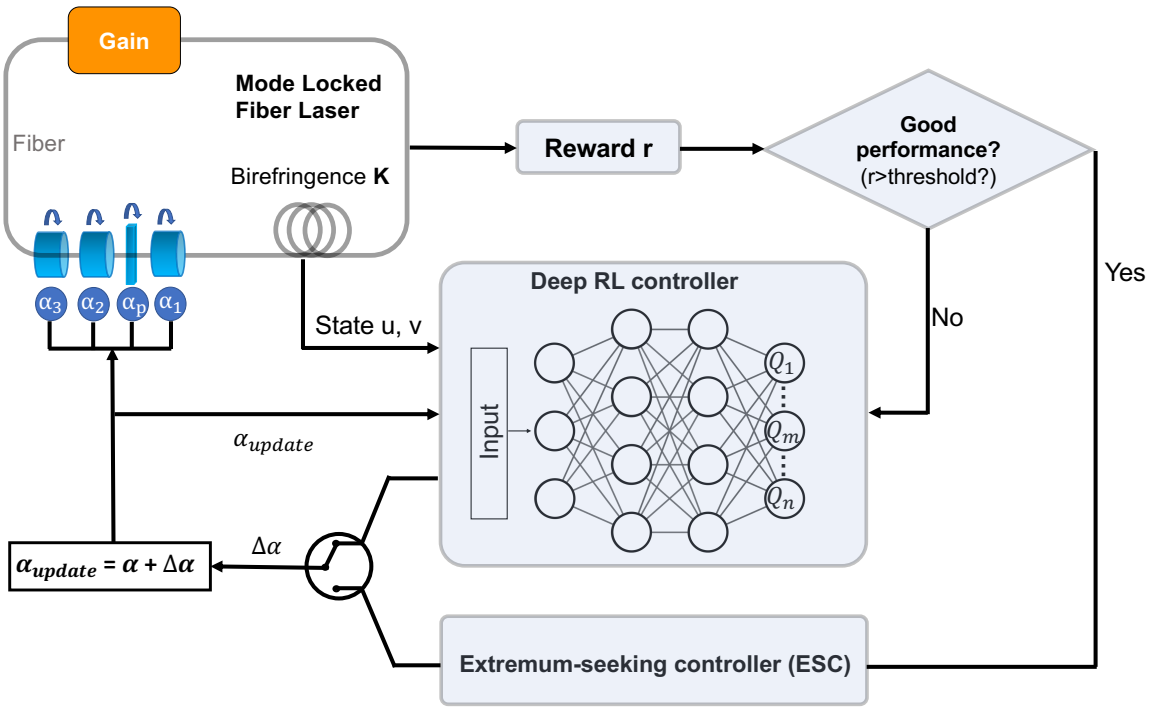

Figure 5.9: Combining the deep reinforcement learning controller with the extremum-seeking controller stabilizes the intra-cavity dynamics and achieves mode-locking with varying birefringence K.

the state of the environment in a bistable system. Deep reinforcement learning is a learning paradigm that integrates the power of reinforcement learning and deep neural networks. It is an ideal ML paradigm for complex dynamical systems where the learning agent is allowed to explore the system and for which trajectory planning is critical for success: both aspects typically manifest in optical systems. The passive mode-locked fiber laser system also manifests one of the key physics features that required the RL agent: bi-stability. Previous self-tuning algorithms take advantage of parameter sweeps and extremum seeking to find optimal solutions. However, these sweeps miss critical bistable structures which must be navigated around in order to achieve ideal model-locking. Indeed, the best solutions are achieved by taking specific trajectories in parameter space, something that the path planning aspects of RL can easily find.

The deep RL controller architecture provided here can be easily integrated and generalized to experimental environments and other optical systems, including for instance, managing instabilities from dispersion management [15], controlling pulse compression [94], and/or circumventing Q-switching instabilities [115]. Importantly, given a well-defined reward criteria and state-space, the deep RL architecture generates experiences with its environment in order to train the deep RL controller.

The deep RL framework demonstrated here can be combined and integrated with other control paradigms, for example, the extremum-seeking controller, for a better control performance. Since the deep RL controller continues searching the entire space even with a good mode-locked solution already found, it is difficult to eliminate the oscillation, and in some cases the controller eventually walks apart from the mode-locked solutions. An integration with the extremum-seeking controller stabilizes the control performance around the optimal solution discovered, even with slowly varying birefringence. With drastic perturbations to the birefringence, our deep RL controller can be promptly fine-tuned to adapt to the new environments using transfer learning. Once a new mode-locked solution is found by the deep RL controller, the extremum-seeking controller is turned on instead to stabilize the system. This hybrid approach marries the ability of deep reinforcement learning to search globally

in a large control space with the increased stability provided by extremum-seeking control via local optimization. Future work looks also to consider emerging methods for producing certifiable RL strategies which can guarantee control performance [44].

BIBLIOGRAPHY

[1] Govind P. Agrawal. Population pulsations and nondegenerate four-wave mixing in semiconductor lasers and amplifiers. J. Opt. Soc. Am. B, 5(1):147, 1988.

[2] Y Arakawa and A Yariv. Quantum well lasers - gain, spectra, dynamics. IEEE J. Quantum Electron., QE22(9):1887, 1986.

[3] Brandon G. Bale, Khanh Kieu, J. Nathan Kutz, and Frank Wise. Transition dynamics for multi-pulsing in mode-locked lasers. Opt. Express, 17(25):23137–23146, Dec 2009.

[4] Brandon G. Bale and J. Nathan Kutz. Variational method for mode-locked lasers. J. Opt. Soc. Am. B, 25(7):1193–1202, Jul 2008.

[5] Brandon G Bale, J Nathan Kutz, and Björn Sandstede. Optimizing waveguide array mode-locking for high-power fiber lasers. IEEE Journal of Selected Topics in Quantum Electronics, 15(1):220–231, 2009.

[6] Salvador Balle. Simple analytical approximations for the gain and refractive index spectra in quantum-well lasers. Physical Review A, 57(2):1304, 1998.

[7] Changjing Bao, Lin Zhang, Andrey Matsko, Yan Yan, Zhe Zhao, Guodong Xie, Anuradha M. Agarwal, Lionel C. Kimerling, Jurgen Michel, Lute Maleki, and Alan E. Willner. Nonlinear conversion efficiency in kerr frequency comb generation. Opt. Lett., 39(21):6126–6129, Nov 2014.

[8] Carl M Bender and Steven A Orszag. Advanced mathematical methods for scientists and engineers I: Asymptotic methods and perturbation theory. Springer Science & Business Media, 2013.

[9] Keith J Blow and David Wood. Theoretical description of transient stimulated raman scattering in optical fibers. IEEE Journal of Quantum Electronics, 25(12):2665–2673, 1989.

[10] Francesca Bontempi, Nicola Andriolli, Filippo Scotti, Marco Chiesa, and Giampiero Contestabile. Comb line multiplication in an inp integrated photonic circuit based on cascaded modulators. IEEE Journal of Selected Topics in Quantum Electronics, 25(6):1–7, 2019.

[11] Nathaniel Bottman, Bernard Deconinck, and Michael Nivala. Elliptic solutions of the defocusing nls equation are stable. Journal of Physics A: Mathematical and Theoretical, 44(28):285201, 2011.

[12] Jared C Bronski, Lincoln D Carr, Ricardo Carretero-González, Bernard Deconinck, J Nathan Kutz, and Keith Promislow. Stability of attractive bose-einstein condensates in a periodic potential. Physical Review E, 64(5):056615, 2001.

[13] Jared C Bronski, Lincoln D Carr, Bernard Deconinck, and J Nathan Kutz. Bose-einstein condensates in standing waves: The cubic nonlinear schrödinger equation with a periodic potential. Physical Review Letters, 86(8):1402, 2001.

[14] Jared C Bronski, Lincoln D Carr, Bernard Deconinck, J Nathan Kutz, and Keith Promislow. Stability of repulsive bose-einstein condensates in a periodic potential. Physical Review E, 63(3):036612, 2001.

[15] Jared C Bronski and J Nathan Kutz. Modulational stability of plane waves in nonreturn-to-zero communications systems with dispersion management. Optics letters, 21(13):937–939, 1996.

[16] Steven L Brunton, Xing Fu, and J Nathan Kutz. Extremum-seeking control of a mode-locked laser. IEEE Journal of Quantum Electronics, 49(10):852–861, 2013.

[17] Steven L Brunton, Xing Fu, and J Nathan Kutz. Self-tuning fiber lasers. IEEE Journal of Selected Topics in Quantum Electronics, 20(5):464–471, 2014.

[18] Steven L Brunton and J Nathan Kutz. Data-driven science and engineering: Machine learning, dynamical systems, and control. Cambridge University Press, 2019.

[19] Paul F Byrd and Morris D Friedman. Handbook of elliptic integrals for engineers and physicists, volume 67. Springer, 2013.

[20] Cosimo Calò, Vidak Vujicic, Regan Watts, Colm Browning, Kamel Merghem, Vivek Panapakkam, Francois Lelarge, Anthony Martinez, Badr-Eddine Benkelfat, Abderrahim Ramdane, and Liam P. Barry. Single-section quantum well mode-locked laser for 400 gb/s ssb-ofdm transmission. Opt. Express, 23(20):26442, 2015.

[21] Lincoln D Carr, Charles W Clark, and Wilhelm P Reinhardt. Stationary solutions of the one-dimensional nonlinear schrödinger equation. ii. case of attractive nonlinearity. Physical Review A, 62(6):063611, 2000.

[22] Qing Chao, Darren D Hudson, J Nathan Kutz, and ST Cundiff. Waveguide array fiber laser. IEEE Photonics Journal, 4(5):1438–1442, 2012.

[23] Yanne K. Chembo and Curtis R. Menyuk. Spatiotemporal lugiato-lefever formalism for kerr-comb generation in whispering-gallery-mode resonators. Phys. Rev. A, 87:053852, May 2013.

[24] Weng W. Chow, Stephan W. Koch, and Murray Sargent III. Semiconductor-Laser Physics. Springer-Verlag, 1994.

[25] Weng W. Chow, Hans Christian Schneider, Stephan W. Koch, Chih-Hao Chang, Lukas Chrostowski, and Connie J. Chang-Hasnain. Nonequilibrium model for semiconductor laser modulation response. IEEE J. Quantum Electron., 38(4):402, 2002.

[26] DN Christodoulides and RI Joseph. Discrete self-focusing in nonlinear arrays of coupled waveguides. Optics letters, 13(9):794–796, 1988.

[27] Shun Lien Chuang. Physics of Photonic Devices. John Wiley and Sons, Inc., Hoboken, NJ, 2nd edition, 2009.

[28] Earl A Coddington and Norman Levinson. Theory of ordinary differential equations. Tata McGraw-Hill Education, 1955.

[29] Ian Coddington, William C. Swann, and Nathan R. Newbury. Coherent multiheterodyne spectroscopy using stabilized optical frequency combs. Phys. Rev. Lett., 100:13902, 2008.

[30] Mark C Cross and Pierre C Hohenberg. Pattern formation outside of equilibrium. Reviews of modern physics, 65(3):851, 1993.

[31] Steven T Cundiff and Andrew M Weiner. Optical arbitrary waveform generation. Nature Photonics, 4(11):760–766, 2010.

[32] Steven T. Cundiff and Andrew M. Weiner. Optical arbitrary waveform generation. Nat. Phot., 4:760, 2010.

[33] Steven T. Cundiff and Jun Ye. Femtosecond optical frequency combs. Rev. of Mod. Phys., 75(1):325, March 2003.

[34] Bernard Deconinck and Benjamin L Segal. The stability spectrum for elliptic solutions to the focusing nls equation. Physica D: Nonlinear Phenomena, 346:1–19, 2017.

[35] Peter J. Delfyett, Leigh Thirion Florez, N. Stoffel, T. Gmitter, Nicholas C. Andreadakis, Yaron Silberberg, and Jonathan P. Heritage. High-power ultrafast laser diodes. IEEE J. Quantum Electron., 28(10):2203, 1992.

[36] Pascal DelHaye, T Herr, E Gavartin, ML Gorodetsky, Ronald Holzwarth, and Tobias J Kippenberg. Octave spanning tunable frequency comb from a microresonator. Physical Review Letters, 107(6):063901, 2011.

[37] Dennis J. Derickson, Roger J. Helkey, Alan Mar, Judy R. Karin, John G. Wasserbauer, and John E. Bowers. Short pulse generation using multisegment mode-locked semiconductor lasers. IEEE J. of Quant. Elec., 28(10):2186, 1992.

[38] S. A. Diddams, Th. Udem, J. C. Bergquist, E. A. Curtis, R. E. Drullinger, L. Hollberg, W. M. Itano, W. D. Lee, C. W. Oates, K. R. Vogel, and D. J. Wineland. An optical clock based on a single trapped 199 hg1+ ion. Science, 293:825, 2001.

[39] Edwin Ding and J Nathan Kutz. Operating regimes and performance optimization in mode-locked fiber lasers. Optics and Spectroscopy, 111(2):166, 2011.

[40] Edwin Ding, Eli Shlizerman, and J Nathan Kutz. Generalized master equation for high-energy passive mode-locking: the sinusoidal ginzburg–landau equation. IEEE journal of quantum electronics, 47(5):705–714, 2011.

[41] Mark Dong, Steven T Cundiff, and Herbert G Winful. Physics of frequency-modulated comb generation in quantum-well diode lasers. Physical Review A, 97(5):053822, 2018.

[42] Mark Dong, Niall M Mangan, J Nathan Kutz, Steven T Cundiff, and Herbert G Winful. Traveling wave model for frequency comb generation in single-section quantum well diode lasers. IEEE Journal of Quantum Electronics, 53(6):1–11, 2017.

[43] JN Elgin. Perturbations of optical solitons. Physical Review A, 47(5):4331, 1993.

[44] Michael Everett, Bjorn Lutjens, and Jonathan P How. Certified adversarial robustness for deep reinforcement learning. arXiv preprint arXiv:2004.06496, 2020.

[45] Fahmida Ferdous, Houxun Miao, Daniel E Leaird, Kartik Srinivasan, Jian Wang, Lei Chen, Leo Tom Varghese, and Andrew M Weiner. Spectral line-by-line pulse shaping of on-chip microresonator frequency combs. Nature Photonics, 5(12):770–776, 2011.

[46] Martin E. Fermann and Ingmar Hartl. Ultrafast fibre lasers. Nat. Phot., 7:868, 2013.

[47] Xing Fu, Steven L Brunton, and J Nathan Kutz. Classification of birefringence in mode-locked fiber lasers using machine learning and sparse representation. Optics express, 22(7):8585–8597, 2014.

[48] Thierry Gallay and Dmitry Pelinovsky. Orbital stability in the cubic defocusing nls equation: I. cnoidal periodic waves. Journal of Differential Equations, 258(10):3607–3638, 2015.

[49] Thierry Gallay and Dmitry Pelinovsky. Orbital stability in the cubic defocusing nls equation: I. cnoidal periodic waves. Journal of Differential Equations, 258(10):3607–3638, 2015.

[50] Mariangela Gioannini, Paolo Bardella, and Ivo Montrosset. Time-domain traveling-wave analysis of the multimode dynamics of quantum dot fabry–perot lasers. IEEE Sel. Topics Quantum Electron., 21(6):1900811, December 2015.

[51] Cyril Godey, Irina V. Balakireva, Aurélien Coillet, and Yanne K. Chembo. Stability analysis of the spatiotemporal lugiato-lefever model for kerr optical frequency combs in the anomalous and normal dispersion regimes. Phys. Rev. A, 89:063814, Jun 2014.

[52] Ian Goodfellow, Yoshua Bengio, and Aaron Courville. Deep learning. MIT press, 2016.

[53] Ariel Gordon, Christine Y. Wang, L. Diehl, F. X. Kärtner, A. Belyanin, D. Bour, S. Corzine, G. Höfler, H. C. Liu, H. Schneider, T. Maier, M. Troccoli, J. Faist, and Federico Capasso. Multimode regimes in quantum cascade lasers: From coherent instabilities to spatial hole burning. Phys. Rev. A, 77(5):053804, 2008.

[54] James P Gordon and Hermann A Haus. Random walk of coherently amplified solitons in optical fiber transmission. Optics letters, 11(10):665–667, 1986.

[55] Hairun Guo, Maxim Karpov, Erwan Lucas, Arne Kordts, Martin HP Pfeiffer, Victor Brasch, Grigory Lihachev, Valery E Lobanov, Michael L Gorodetsky, and Tobias J Kippenberg. Universal dynamics and deterministic switching of dissipative kerr solitons in optical microresonators. Nature Physics, 2016.

[56] Stephen Gustafson, Stefan Le Coz, and Tai-Peng Tsai. Stability of periodic waves of 1d cubic nonlinear schrödinger equations. Applied Mathematics Research eXpress, 2017(2):431–487, 2017.

[57] Hado V Hasselt. Double q-learning. In Advances in neural information processing systems, pages 2613–2621, 2010.

[58] C. H. Henry, R. A. Logan, and K. A. Bertness. Spectral dependence of the change in refractive index due to carrier injection in gaas lasers. Journal of Applied Physics, 51(7):4457, 1981.

[59] T Herr, V Brasch, JD Jost, CY Wang, NM Kondratiev, ML Gorodetsky, and TJ Kippenberg. Temporal solitons in optical microresonators. Nature Photonics, 8(2):145–152, 2014.

[60] T Herr, V Brasch, JD Jost, CY Wang, NM Kondratiev, ML Gorodetsky, and TJ Kippenberg. Temporal solitons in optical microresonators. Nature Photonics, 8(2):145–152, 2014.

[61] T. Herr, K. Hartinger, J. Riemensberger, C. Y. Wang, E. Gavartin, R. Holzwarth, M. L. Gorodetsky, and T. J. Kippenberg. Universal formation dynamics and noise of kerr-frequency combs in microresonators. Nat. Phot., 6:480, 2012.

[62] T Herr, K Hartinger, J Riemensberger, CY Wang, E Gavartin, R Holzwarth, ML Gorodetsky, and TJ Kippenberg. Universal formation dynamics and noise of kerr-frequency combs in microresonators. Nature Photonics, 6(7):480–487, 2012.

[63] M. Homar, S. Balle, and M San Miguel. Mode competition in a fabry-perot semiconductor laser: travelling wave model with asymmetric dynamical gain. Optics Communications, 131:380–390, 1996.

[64] M. Homar, J. V. Moloney, and M. San Miguel. Traveling wave model of a multimode fabry-perot laser in free running and external cavity configurations. IEEE J. Quantum Electron., 32(3):553, 1996.

[65] Darren D Hudson, J Nathan Kutz, Thomas R Schibli, Demetrios N Christodoulides, Roberto Morandotti, and Steven T Cundiff. Spatial distribution clamping of discrete spatial solitons due to three photon absorption in algaas waveguide arrays. Optics express, 20(3):1939–1944, 2012.

[66] Darren D Hudson, Kimberlee Shish, Thomas R Schibli, J Nathan Kutz, Demetrios N Christodoulides, Roberto Morandotti, and Steven T Cundiff. Nonlinear femtosecond pulse reshaping in waveguide arrays. Optics letters, 33(13):1440–1442, 2008.

[67] Julien Javaloyes and Salvador Balle. Emission directionality of semiconductor ring lasers: A traveling-wave description. IEEE J. Quantum Electron., 45(5):431, 2009.

[68] Julien Javaloyes and Salvador Balle. Mode-locking in semiconductor fabry-perot lasers. IEEE Journal of Quantum Electronics, 46(7):1023–1030, 2010.

[69] D J Jones, L M Zhang, J E Carroll, and D D Marcenac. Dynamics of monolithic passively mode-locked semiconductor lasers. IEEE J. Quantum Electron., 31(6):1051–1058, June 1995.

[70] Todd Kapitula, J Nathan Kutz, and Björn Sandstede. Stability of pulses in the master mode-locking equation. JOSA B, 19(4):740–746, 2002.

[71] Todd Kapitula, Nathan Kutz, and Björn Sandstede. The evans function for nonlocal equations. Indiana University mathematics journal, pages 1095–1126, 2004.

[72] VI Karpman and EM Maslov. Perturbation theory for solitons. JETP, 73:537–559, 1977.

[73] Maxim Karpov, Hairun Guo, Arne Kordts, Victor Brasch, Martin H. P. Pfeiffer, Michail Zervas, Michael Geiselmann, and Tobias J. Kippenberg. Raman self-frequency shift of dissipative kerr solitons in an optical microresonator. Phys. Rev. Lett., 116:103902, Mar 2016.

[74] Maxim Karpov, Hairun Guo, Arne Kordts, Victor Brasch, Martin HP Pfeiffer, Michail Zervas, Michael Geiselmann, and Tobias J Kippenberg. Raman self-frequency shift of dissipative kerr solitons in an optical microresonator. Physical review letters, 116(10):103902, 2016.

[75] FX Kartner, ID Jung, and U Keller. Soliton mode-locking with saturable absorbers. IEEE Journal of Selected Topics in Quantum Electronics, 2(3):540–556, 1996.

[76] Simeon N. Kaunga-Nyirenda, Michal P. Dlubek, Andrew J. Phillips, Jun Jun Lim, Eric C. Larkins, and Slawomir Sujecki. Theoretical investigation of the role of optically induced carrier pulsations in wave mixing in semiconductor optical amplifiers. J. Opt. Soc. Am. B, 27(2):168, February 2010.

[77] DJ Kaup. Perturbation theory for solitons in optical fibers. Physical Review A, 42(9):5689, 1990.

[78] Jirayr Kevorkian and Julian D Cole. Perturbation methods in applied mathematics, volume 34. Springer Science & Business Media, 2013.

[79] I Kilen, J. Hader, J. V. Moloney, and S. W. Koch. Ultrafast nonequilibrium carrier dynamics in semiconductor laser mode locking. Optica, 1(4):192, 2014.

[80] Tobias J Kippenberg, Ronald Holzwarth, and SA Diddams. Microresonator-based optical frequency combs. Science, 332(6029):555–559, 2011.

[81] Yuji Kodama and Mark J Ablowitz. Perturbations of solitons and solitary waves. Studies in Applied Mathematics, 64(3):225–245, 1981.

[82] Andrey Komarov, Herve Leblond, and François Sanchez. Multistability and hysteresis phenomena in passively mode-locked fiber lasers. Physical review A, 71(5):053809, 2005.

[83] Miroslav Krstić and Hsin-Hsiung Wang. Stability of extremum seeking feedback for general nonlinear dynamic systems. Automatica, 36(4):595–601, 2000.

[84] J. N. Kutz. Data-Driven Modeling & Scientific Computation: Methods for Complex Systems & Big Data. Oxford University Press, 2013.

[85] J Nathan Kutz. Mode-locked soliton lasers. SIAM review, 48(4):629–678, 2006.

[86] J Nathan Kutz. Passive mode-locking using phase-sensitive amplification. Physical Review A, 78(1):013845, 2008.

[87] J Nathan Kutz and Steven L Brunton. Intelligent systems for stabilizing mode-locked lasers and frequency combs: machine learning and equation-free control paradigms for self-tuning optics. Nanophotonics, 4(1):459–471, 2015.

[88] J Nathan Kutz, Brandon C Collings, Keren Bergman, Sergio Tsuda, Steven T Cundiff, Wayne H Knox, Philip Holmes, and Michael Weinstein. Mode-locking pulse dynamics in a fiber laser with a saturable bragg reflector. JOSA B, 14(10):2681–2690, 1997.

[89] J Nathan Kutz and Björn Sandstede. Theory of passive harmonic mode-locking using waveguide arrays. Optics Express, 16(2):636–650, 2008.

[90] J Nathan Kutz and PKA Wai. Gordon-haus timing jitter reduction in dispersion-managed soliton communications. IEEE Photonics Technology Letters, 10(5):702–704, 1998.

[91] Jose Nathan Kutz and Edward Farnum. Solitons and ultra-short optical waves: the short-pulse equation versus the nonlinear schrödinger equation. Edited by HE Hernández-Figueroa, E. Recami, page 148, 2014.

[92] Daan Lenstra and Mirvais Yousefi. Rate-equation model for multi-mode semiconductor lasers with spatial hole burning. Opt. Express, 22(7):8144, 2014.

[93] Feng Li, P. K. A. Wai, and J. Nathan Kutz. Geometrical description of the onset of multi-pulsing in mode-locked laser cavities. J. Opt. Soc. Am. B, 27(10):2068–2077, Oct 2010.

[94] Qian Li, J Nathan Kutz, and PKA Wai. High-degree pulse compression and high-coherence supercontinuum generation in a convex dispersion profile. Optics Communications, 301:29–33, 2013.

[95] W Liang, D Eliyahu, VS Ilchenko, AA Savchenkov, AB Matsko, D Seidel, and L Maleki. High spectral purity kerr frequency comb radio frequency photonic oscillator. Nature communications, 6, 2015.

[96] Peicheng Liao, Changjing Bao, Arne Kordts, Maxim Karpov, Martin HP Pfeiffer, Lin Zhang, Amirhossein Mohajerin-Ariaei, Yinwen Cao, Ahmed Almaiman, Morteza Ziyadi, et al. Dependence of a microresonator kerr frequency comb on the pump linewidth. Optics Letters, 42(4):779–782, 2017.

[97] Long-Ji Lin. Reinforcement learning for robots using neural networks. Technical report, Carnegie-Mellon Univ Pittsburgh PA School of Computer Science, 1993.

[98] Luigi A Lugiato and René Lefever. Spatial dissipative structures in passive optical systems. Physical review letters, 58(21):2209, 1987.

[99] TH Maiman. Optical and microwave-optical experiments in ruby. Physical review letters, 4(11):564, 1960.

[100] Dawn Marshall, Alan Miller, and Chris C. Button. In-well ambipolar diffusion in room-temperature ingaasp multiple quantum wells. IEEE J. Quantum Electron., 36(9):1013, 2000.

[101] David McDonald and Ronan F O'Dowd. Comparison of two- and three-level rate equations in the modeling of quantum-well lasers. IEEE J. Quantum Electron., 31(11):1927, November 1995.

[102] Antonio Mecozzi, John D Moores, Hermann A Haus, and Yinchiah Lai. Soliton transmission control. Optics letters, 16(23):1841–1843, 1991.

[103] C Menyuk. Nonlinear pulse propagation in birefringent optical fibers. IEEE Journal of Quantum electronics, 23(2):174–176, 1987.

[104] Curtis R Menyuk. Pulse propagation in an elliptically birefringent kerr medium. IEEE journal of quantum electronics, 25(12):2674–2682, 1989.

[105] Carles Milián, Andrey V Gorbach, Majid Taki, Alexey V Yulin, and Dmitry V Skryabin. Solitons and frequency combs in silica microring resonators: Interplay of the raman and higher-order dispersion effects. Physical Review A, 92(3):033851, 2015.

[106] Volodymyr Mnih, Koray Kavukcuoglu, David Silver, Andrei A Rusu, Joel Veness, Marc G Bellemare, Alex Graves, Martin Riedmiller, Andreas K Fidjeland, Georg Ostrovski, et al. Human-level control through deep reinforcement learning. Nature, 518(7540):529–533, 2015.

[107] Linn F Mollenauer, James P Gordon, and Stephen G Evangelides. The sliding-frequency guiding filter: an improved form of soliton jitter control. Optics letters, 17(22):1575–1577, 1992.

[108] Valentina Moskalenko, Jeroen Koelemeij, Kevin Williams, and Erwin Bente. Study of extra wide coherent optical combs generated by a qw-based integrated passively mode-locked ring laser. Opt. Letters, 42(7):1428, 2017.

[109] Sinno Jialin Pan and Qiang Yang. A survey on transfer learning. IEEE Transactions on knowledge and data engineering, 22(10):1345–1359, 2009.

[110] Scott B Papp and Scott A Diddams. Spectral and temporal characterization of a fused-quartz-microresonator optical frequency comb. Physical Review A, 84(5):053833, 2011.

[111] M Deseada Gutierrez Pascual, Vidak Vujicic, Jules Braddell, Frank Smyth, Prince M Anandarajah, and Liam P Barry. Inp photonic integrated externally injected gain switched optical frequency comb. Optics letters, 42(3):555–558, 2017.

[112] Ulf Peschel, Roberto Morandotti, John M Arnold, J Stewart Aitchison, Hagai S Eisenberg, Yaron Silberberg, Thomas Pertsch, and Falk Lederer. Optical discrete solitons in waveguide arrays. 2. dynamic properties. JOSA B, 19(11):2637–2644, 2002.

[113] Joerg Pfeifle, Victor Brasch, Matthias Lauermann, Yimin Yu, Daniel Wegner, Tobias Herr, Klaus Hartinger, Philipp Schindler, Jingshi Li, David Hillerkuss, et al. Coherent terabit communications with microresonator kerr frequency combs. Nature photonics, 8(5):375–380, 2014.

[114] Joshua L Proctor and J Nathan Kutz. Passive mode-locking by use of waveguide arrays. Optics letters, 30(15):2013–2015, 2005.

[115] Joshua L Proctor and J Nathan Kutz. Theory of q switching in actively mode-locked lasers. JOSA B, 23(4):652–662, 2006.

[116] Lutfur Rahman and Herbert G Winful. Improved coupled-mode theory for the dynamics of semiconductor laser arrays. Optics letters, 18(2):128–130, 1993.

[117] Lutfur Rahman and Herbert G Winful. Nonlinear dynamics of semiconductor laser arrays: a mean field model. IEEE journal of quantum electronics, 30(6):1405–1416, 1994.

[118] R. Rosales, K. Merghem, C. Calo, G. Bouwmans, I. Krestnikov, A. Martinez, and A. Ramdane. Optical pulse generation in single section inas/gaas quantum dot edge emitting lasers under continuous wave operation. App. Phys. Lett., 101:221113, 2012.

[119] Ricardo Rosales, Kamel Merghem, Anthony Martinez, A. Akrout, J.-P. Tourrenc, Alain Accard, Francois Lelarge, and Abderrahim Ramdane. Inas/inp quantum-dot passively mode-locked lasers for 1.55-μm applications. IEEE J. Sel. Top. Quantum Electron., 17(5):1292, 2011.

[120] Ricardo Rosales, S. G. Murdoch, R.T. Watts, K. Merghem, Anthony Martinez, Francois Lelarge, Alain Accard, L. P. Barry, and Abderrahim Ramdane. High performance mode locking characteristics of single section quantum dash lasers. Optics Express, 20(8):8649, 2012.

[121] Mattia Rossetti, Paolo Bardella, and Ivo Montrosset. Time-domain travelling-wave model for quantum dot passively mode-locked lasers. IEEE J. Quantum Electron., 47(2):139, 2011.

[122] Kenji Sato. Optical pulse generation using fabry–pérot lasers under continuous-wave operation. IEEE J. Sel. Top. Quantum Electron., 9(5):1288, 2003.

[123] Benjamin Schleich, Nabil Anwer, Luc Mathieu, and Sandro Wartzack. Shaping the digital twin for design and production engineering. CIRP Annals, 66(1):141–144, 2017.

[124] C Serrat and C Masoller. Modeling spatial effects in multi-longitudinal-mode semiconductor lasers. Physical Review A, 73(4):043812, 2006.

[125] C. Serrat and C. Masoller. Modeling spatial effects in multi-longitudinal-mode semiconductor lasers. Phys. Rev. A, 73:043812, 2006.

[126] Xuling Shen, Wenxue Li, Ming Yan, and Heping Zeng. Electronic control of nonlinear-polarization-rotation mode locking in yb-doped fiber lasers. Optics Letters, 37(16):3426–3428, 2012.

[127] Y. Silberberg, P. W. Smith, and D. J. Eilenberger. Passive mode locking of a semiconductor diode laser. Optics Letters, 9(11):507, 1984.

[128] David Silver, Thomas Hubert, Julian Schrittwieser, Ioannis Antonoglou, Matthew Lai, Arthur Guez, Marc Lanctot, Laurent Sifre, Dharshan Kumaran, Thore Graepel, et al. A general reinforcement learning algorithm that masters chess, shogi, and go through self-play. Science, 362(6419):1140–1144, 2018.

[129] NJ Smith, W Forysiak, and NJ Doran. Reduced gordon-haus jitter due to enhanced power solitons in strongly dispersion managed systems. Electronics Letters, 32(22):2085–2086, 1996.

[130] Kristin M Spaulding, Darryl H Yong, Arnold D Kim, and J Nathan Kutz. Nonlinear dynamics of mode-locking optical fiber ring lasers. JOSA B, 19(5):1045–1054, 2002.

[131] Martin Spreemann, Mark Lichtner, Mindaugas Radziunas, Uwe Bandelow, and Hans Wenzel. Measurement and simulation of distributed-feedback tapered master-oscillator power amplifiers. IEEE Journal of Quantum Electronics, 45(6):609–616, 2009.

[132] C. B. Su. Dielectric grating induced by cavity standing wave as a new explanation of origin of nonlinear gain in semiconductor diode lasers. IEEE Electron. Lett., 24(7):370–371, 1988.

[133] Myoung-Gyun Suh, Qi-Fan Yang, Ki Youl Yang, Xu Yi, and Kerry J Vahala. Microresonator soliton dual-comb spectroscopy. Science, 354(6312):600–603, 2016.

[134] Chang Sun, Travis Askham, and J Nathan Kutz. Stability and dynamics of microring combs: elliptic function solutions of the lugiato–lefever equation. JOSA B, 35(6):1341–1353, 2018.

[135] Chang Sun, Mark Dong, Niall M Mangan, Herbert G Winful, Steven T Cundiff, and J Nathan Kutz. Frequency comb generation at 800nm in waveguide array quantum well diode lasers. IEEE Journal of Quantum Electronics, 2019.

[136] Chang Sun, Eurika Kaiser, Steven L Brunton, and J Nathan Kutz. Deep reinforcement learning for optical systems: A case study of mode-locked lasers. Machine Learning: Science and Technology, 1(4):045013, oct 2020.

[137] Chang Sun, Niall Mangan, Mark Dong, Herbert G Winful, Steven T Cundiff, and J Nathan Kutz. Stable numerical schemes for nonlinear dispersive equations with counter-propagation and gain dynamics. JOSA B, 36(12):3263–3274, 2019.

[138] D. H. Sutter, G. Steinmeyer, L. Gallmann, N. Matuschek, F. Morier-Genoud, U. Keller, V. Scheuer, G. Angelow, and T. Tschudi. Semiconductor saturable-absorber mirror- assisted kerr-lens mode-locked ti:sapphire laser producing pulses in the two-cycle regime. Opt. Lett., 24:631, 1999.

[139] R. S. Sutton. Learning to predict by the methods of temporal differences. Machine learning, 3(1):9–44, 1988.

[140] M Suzuki, I Morita, N Edagawa, S Yamamoto, H Taga, and S Akiba. Reduction of gordon-haus timing jitter by periodic dispersion compensation in soliton transmission. Electronics Letters, 31(23):2027–2029, 1995.

[141] Luuk F. Tiemeijer, P. I. Kuindersma, Peter J. A. Thijs, and Geert L. J. Rikken. Passive fm locking in ingaasp semiconductor lasers. IEEE J. Quantum Electron., 25(6):1385, 1989.

[142] Philipp Trocha, M Karpov, D Ganin, Martin HP Pfeiffer, Arne Kordts, S Wolf, J Krockenberger, Pablo Marin-Palomo, Claudius Weimann, Sebastian Randel, et al. Ultrafast optical ranging using microresonator soliton frequency combs. Science, 359(6378):887–891, 2018.

[143] Th. Udem, J. Reichert, R. Holzwarth, and T. W. Hänsch. Absolute optical frequency measurement of the cesium d1 line with a mode-locked laser. Phys. Rev. Lett., 82(18):3568, 1999.

[144] Hado Van Hasselt, Arthur Guez, and David Silver. Deep reinforcement learning with double q-learning. In Thirtieth AAAI conference on artificial intelligence, 2016.

[145] Aaron D. Vandermeer and Daniel T. Cassidy. A rate equation model of asymmetric multiple quantum-well lasers. IEEE J. Quantum Electron., 41(7):917, 2005.

[146] C. J. C. H. Watkins. Learning from delayed rewards. PhD thesis, 1989.

[147] Christopher JCH Watkins and Peter Dayan. Q-learning. Machine learning, 8(3-4):279–292, 1992.

[148] Michael I Weinstein. Modulational stability of ground states of nonlinear schrödinger equations. SIAM journal on mathematical analysis, 16(3):472–491, 1985.

[149] Matthew O. Williams, Eli Shlizerman, and J. Nathan Kutz. The multi-pulsing transition in mode-locked lasers: a low-dimensional approach using waveguide arrays. J. Opt. Soc. Am. B, 27(12):2471–2481, Dec 2010.

[150] Amnon Yariv. Coupled-mode theory for guided-wave optics. IEEE Journal of Quantum Electronics, 9(9):919–933, 1973.

[151] Xu Yi, Qi-Fan Yang, Ki Youl Yang, Myoung-Gyun Suh, and Kerry Vahala. Soliton frequency comb at microwave rates in a high-q silica microresonator. Optica, 2(12):1078–1085, 2015.

[152] Xiao Zhang, Matthew Williams, Steven T Cundiff, and J Nathan Kutz. Semiconductor diode laser mode-locking by a waveguide array. IEEE Journal of Selected Topics in Quantum Electronics, 22(2):34–39, 2016.